Mechanocapillary Forming of Filamentary Materials

by

Sameh Hani Tawfick

A dissertation submitted in partial fulfillment
of the requirements for the degree of
Doctor of Philosophy
(Mechanical Engineering)
in The University of Michigan
2012

Doctoral Committee

Assistant Professor Anastasios John Hart, Chair
Professor Kensall D. Wise
Associate Professor Joerg Lahann
Associate Professor Wei Lu

ACKNOWLEDGEMENTS

My PhD journey was enjoyable!

I have been extremely fortunate to work with John Hart on the elegant topic of this thesis. John's energetic and enthusiastic approach to research made the last four years feel more like four months! He sets the example of how fun and hard work, creativity and comprehensiveness, and friendship and advising can be harmoniously combined.

I would like to thank my thesis committee: Professors Kensall D. Wise, Joerg Lahann and Wei Lu for their insightful discussions and inspiring suggestions.

I am grateful to Rackham Graduate School and Mechanical Engineering department for the generous fellowships and awards.

I am thankful for the fun and fruitful collaborations with fellow students and post-docs:

- Michael De Volder for his leadership in exploring all aspects of 3-D CNT research and for being a real friend.
- The Mechanosynthesis team for their coordinated efforts and mutual friendship and support.
- Xiaopei Deng and Zhouzhou Zhao for the fruitful collaborations.
- NNIN and undergraduate students for working on various topics of the thesis.
- EMAL and LNF staff for the help with various aspects of the experiments.

For any achievement, I am most indebted to my loving wife. Christine, who is a mom and a commuting psychology PhD student at MSU, understands CNTs and capillary forces more than my understanding of how to use our own washing machine or pay DTE bills online. I can't thank you enough!

I am grateful to my aunts and my parents in law for their encouragement and support.

Last but not least, my daughter, sister, brother, mom and dad, thank you for your continuous faith and unconditional love.

TABLE OF CONTENTS

ACKNOWLEDGEMENTS ii

LIST OF FIGURES vii

LIST OF TABLES xi

ABSTRACT xii

Chapter 1 Introduction and thesis scope 1

1. 1 Motivation 1

1. 2 Thesis scope 2

1. 3 Thesis outline 4

1. 4 Bibliography 6

Chapter 2 3-D surfaces and CNTs in microfabrication 8

2. 1 Classification and fabrication of 3-D anisotropic surfaces 9

2.1.1. Inclined lithography 11

2.1.2. Metal assisted chemical etching 14

2.1.3. Glancing angle deposition 18

2.1.4. Oblique angle polymerization 21

2.1.5. Directed mechanical deformation 22

2.1.6. Oriented nanostructure growth 25

2. 2 Aligned CNTs in microfabrication 29

2.2.1. Properties scaling of CNT assemblies 30

2.2.2. Integration considerations of VA-CNT 32

2.2.3. Examples of properties and applications of VA-CNTs 37
2.2.4. Integration considerations of HA-CNTs 39
2.2.5. Examples of properties and applications of HA-CNTs 41
2. 3 Bibliography 43
Chapter 3 Synthesis and coating of VA-CNT microstructures 53
3. 1 Catalyst patterning and deposition 53
3. 2 VA-CNT growth 57
3.2.1. Catalyst annealing stage 59
3.2.2. CNT growth stage 61
3.2.3. The termination stage 63
3. 3 Effect of pattern size and density 65
3. 4 Plasma etching of VA-CNT 66
3. 5 Coating of VA-CNT microstructures 68
3.5.1. Ceramics coatings by Atomic Layer Deposition 68
3.5.2. Polymer coating by Chemical Vapor Deposition 70
3. 6 Bibliography 73
Chapter 4 Mechanical rolling of VA-CNT 75
4. 1 Process and machine design 76
4. 2 Alignment characteristics of HA-CNT 79
4. 3 Thickness and density of HA-CNT 80
4. 4 Transfer printing of HA-CNT 82
4. 5 Bibliography 84
Chapter 5 Capillary forming of VA-CNT 85
5. 1 Elastocapillary forces in micro- and nanofabrication 85
5. 2 Structural programming for capillary forming 87

5.2.1. Capillary forming of axisymmetric VA-CNTs ... 89
5.2.2. Bending of asymmetric VA-CNTs ... 91
5.2.3. Twisting and hierarchical assembly of asymmetric VA-CNTs ... 91
5. 3 Capillary folding of HA-CNTs ... 93
5. 4 Bibliography ... 97
Chapter 6 Mechanism of capillary forming ... 99
6. 1 Capillary forming building blocks ... 100
6. 2 Dynamics of capillary forming ... 102
6.2.1. Solvent condensation and evaporation ... 103
6.2.2. Self-directed capillary rise ... 103
6.2.3. In situ capillary forming of conical wells ... 105
6.2.4. Kinetics of shape evolution ... 106
6.2.5. Interface migration during evaporation ... 108
6. 3 Forces and stresses in mechanocapillary forming ... 108
6.3.1. Local aggregation of CNTs ... 111
6.3.2. Capillary induced bending ... 112
6.3.3. Capillary folding of thin microstructures ... 114
6. 4 Effect of material modification on capillary forming ... 118
6. 5 Bibliography ... 121
Chapter 7 Integration and properties of mechanocapillary formed CNTs ... 122
7. 1 Mechanical properties of CNT-polymer composite microstructures ... 123
7.1.1. Dense composites by capillary forming and polymer infiltration ... 123
7.1.2. Porous composites by CVD coating ... 126
7. 2 Chemical functionality of coated CNT microstructures ... 131
7. 3 Electrical conductivity of VA-CNT microstructures ... 133

7. 4 Integration of VA-CNT with microfabrication processes 135
7. 5 Responsive CNT-hydrogel composites and transducers 136
7.6 Bibliography 140
Chapter 8 Properties of CNT-CNT joints 142
8. 1 Limits and potential of macro-scale CNT materials 142
8. 2 Mechanical stiffness and strength of CNT joints 146
8. 3 Electrical conductivity of CNT joints 152
8. 4 Bibliography 155
Chapter 9 Fabrication and elastocapillary densification of silicon nanowires 156
9. 1 SiNW by MACE using salt solution 157
9. 2 SiNW by MACE using a metal mesh 159
9. 3 Fabrication of SiNW microstructures by MACE 164
9. 4 Bibliography 168
Chapter 10 Findings and next steps 170
10. 1 Thesis contributions 170
10. 2 Future directions 174
10. 3 Bibliography 178

LIST OF FIGURES

Figure 1.1 Axes of material composition; structural characteristics; and architecture....... 3
Figure 2.1 Classification of anisotropic surfaces with 3-D features.................................. 9
Figure 2.2 Inclined lithography... 12
Figure 2.3 SU-8 microstructure arrays fabricated by inclined lithography. 13
Figure 2.4 Metal assisted chemical etching (MACE) of silicon nanowires (SiNW)....... 15
Figure 2.5 Nanosphere lithography (NSL) template for the fabrication of hierarchically ordered SiNWs by MACE. 16
Figure 2.6 3-D silicon etching by MACE.. 18
Figure 2.7 Glancing Angle Deposition (GLAD). 20
Figure 2.8 Oblique angle polymerization (OAP).. 22
Figure 2.9 Fabrication of bent nanohairs by self-directed mechanical deformation. 24
Figure 2.10 Complex morphologies of inorganic NWs................................... 26
Figure 2.11 3-D VA-CNT nanostructured morphologies.................................. 28
Figure 2.12 Previously published values of CNT electrical conductivity. 31
Figure 2.13 SEM images of CNT films grown by CVD.................................. 33
Figure 2.14 High aspect ratio straight VA-CNT growth and integration. 34
Figure 2.15 Transfer of VA-CNT to flexible substrates.................................. 36
Figure 2.16 Transfer printing of HA-CNTs using PDMS stamps. 41
Figure 2.17 Integrated HA-CNT MEMS resonators and switches................................. 42
Figure 3.1 Fabrication of VA-CNT microstructures.. 55
Figure 3.2 Chemical Vapor Deposition system used to grow VA-CNTs....................... 56
Figure 3.3 VA-CNT growth recipes. 58
Figure 3.4 Atomic Force Microscope images of the catalyst. 59
Figure 3.5 VA-CNT growth rate and density for various catalyst compositions. 60

Figure 3.6 Water vapor content time evolution. 62
Figure 3.7 VA-CNT growth rate and density for various C_2H_4 flow rates. 63
Figure 3.8 VA-CNT growth termination recipe.. 64
Figure 3.9 Mask for studying the effect of catalyst size and density on CNT growth.. .. 65
Figure 3.10 VA-CNT growth rate for various pattern diameters and density 66
Figure 3.11 VA-CNT bending due to variation in growth rate across the same feature. 67
Figure 3.12 VA-CNT top surface morphology. 68
Figure 3.13 Al_2O_3 coating of VA-CNT by Atomic Layer Deposition. 69
Figure 3.14 Parylene coating of VA-CNT by Chemical Vapor Deposition. 71
Figure 4.1 Rolling of VA-CNT blades. 76
Figure 4.2 SEM images of CNTs before and after rolling. 77
Figure 4.3 Rolling of CNT sheets. 77
Figure 4.4 Optical image of the rolling machine. 78
Figure 4.5 Kinematics of rolling 79
Figure 4.6 Characterization of alignment of CNT microstructures 80
Figure 4.7 Control of HA-CNT geometry by control of rolling force. 81
Figure 4.8 Normalized Raman spectra acquired for HA-CNT ribbons. 82
Figure 4.9 Transfer printing of HA-CNTs.. 83
Figure 5.1 Elastocapillary effect in nature and microfabrication 86
Figure 5.2 Elastocapillary aggregation of CNTs. 87
Figure 5.3 Capillary forming setup. 88
Figure 5.4 Method and mechanism of capillary forming of CNT and microstructures. .. 89
Figure 5.5 Map of capillary forming transformations of axisymmetric shapes showing the effect of CNT height for various inner/outer diameter values. 90
Figure 5.6 Programming inclination of conical wells by catalyst shape design. 91
Figure 5.7 Bending of asymmetric CNT microstructures by capillary forming. 92
Figure 5.8 Fabrication of complex geometries by capillary forming.. 93
Figure 5.9 Fabrication of HA-CNT patches by structurally programmed capillary folding.. 94
Figure 5.10 Multi-layered and multi-directional CNT networks. 95

Figure 5.11 A micro CNT crop circle made by precisely folding HA-CNTs and forming VA-CNTs. 96
Figure 6.1 Capillary forming building blocks. 100
Figure 6.2 *In situ* dynamics of capillary forming.. 102
Figure 6.3 Capillary rise around various geometries. 104
Figure 6.4 Capillary rise around various VA-CNT geometries.. 105
Figure 6.5 *In situ* capillary forming of a conical well. 106
Figure 6.6 Kinetics of densification induced shape change. 107
Figure 6.7 Global CNT migration during capillary forming. 109
Figure 6.8 Structural characteristics of CNTs. 109
Figure 6.9 Competition of CNT mechanics and liquid surface tension. 110
Figure 6.10 Comparison of elastocapillary theory with experiments. 112
Figure 6.11 Bending of asymmetric CNT microstructures. 113
Figure 6.12 Mechanism of capillary folding. 115
Figure 6.13 Plots comparing the theory and experiments of elastocapillay buckling. 117
Figure 6.14 Tuning capillary forming by plasma etching. 119
Figure 6.15 Tuning capillary forming by changing the diameter of the CNTs 120
Figure 7.1 Mechanical testing of capillary formed CNT structures. 124
Figure 7.2 SEM image of CNT microstructures coated by Reactive Coating.. 127
Figure 7.3 Compression testing of CNTs coated with Reactive Coating. 128
Figure 7.4 Demonstration of selective chemical functionality of CNT microstructures enabled by polymer coating. 132
Figure 7.5 Electrical measurement of capillary formed CNTs. 133
Figure 7.6 Integration of 3-D CNT with microfabrication. 134
Figure 7.7 *I-V* measurement of radially oriented (RO-) CNTs and HA-CNTs. 135
Figure 7.8 Process for fabrication of 3-D CNT-hydrogel composites. 136
Figure 7.9 Self-directed actuation of 3-D CNT-hydrogel composites. 137
Figure 7.10 Integration of CNT-hydrogel microtransducers. 138
Figure 8.1 Mechanical properties of CNT yarns. 143
Figure 8.2 1-D model of CNT sheet conductivity. 145
Figure 8.3 HA-CNT sheets. 146

Figure 8.4 Mechanocapillary joining of CNTs by rolling and overlapping. 147
Figure 8.5 Mechanical stiffness of CNT strips. 148
Figure 8.6 Mechanical strength of CNT strips.. 149
Figure 8.7 SEM showing the CNT strip after failure.. 150
Figure 8.8 Electrical model of CNT sheet conductivity 152
Figure 8.9 Electrical characterization of the CNT joint... 153
Figure 9.1 Fabrication of silicon nanowires (SiNWs) by MACE using salt solution..... 158
Figure 9.2 Fabrication of SiNWs by MACE using HF/H_2O_2 solution and a metal mesh 160
Figure 9.3 SEM image showing the surface morphology of the metal mesh. 161
Figure 9.4 SEM image showing the morphology of the metal mesh and the resulting SiNWs. 162
Figure 9.5 SEM showing the elastocapillary aggregation of SiNWs 163
Figure 9.6 SEM showing the aggregation morphology of high aspect ratio SiNWs..... 163
Figure 9.7 Fabrication of SiNW microstructures by MACE using salt solution. 165
Figure 9.8 SEM images of SiNW microstructures by MACE using salt solution......... 166
Figure 9.9 Fabrication of SiNW microstructure by MACE using a metal mesh........... 167

LIST OF TABLES

Table 2.1 Comparison of process capabilities for fabrication of anisotropic surfaces with 3-D features 11
Table 2.2 Comparison of some microfabrication material properties with CNTs 30
Table 2.3 Details of CNT electrical data plotted in Figure 2.12, cited from previous studies of individual CNTs and CNT assemblies 31
Table 2.4 Recent advances and benchmarks in CNT interconnect via 38
Table 3.1 Process parameters for catalyst patterning by photolithography 54
Table 3.2 CNT catalyst deposition process parameters 57
Table 3.3 Process parameters for plasma etching of VA-CNTs 67
Table 7.1 Dimensions and properties of various capillary formed CNT microstructures characterized by mechanical compression 125
Table 7.2 Dimensions and properties of various parylene coated CNT microstructures characterized by mechanical compression 131
Table 8.1 Calculated stiffness, strength and energy stored and dissipated for cycles 1 to 3 149
Table 9.1 Mechanical properties of SiNWs prepared by MACE using ($AgNO_3$+HF) by a MEMS compression testing cell mounted inside the SEM chamber 159

ABSTRACT

The hierarchical structure and organization of filaments within natural materials determine their collective chemical and physical functionalities. Synthetic nanoscale filaments such as carbon nanotubes (CNTs) are known for their outstanding properties including high stiffness and strength at low density, and high electrical conductivity and current carrying capacity. Ordered assemblies of densely packed CNTs are therefore expected to enable the synthesis of new materials having outstanding multifunctional performance. However, current methods of CNT synthesis have inadequate control of quality, density and order.

In pursuit of these needs, a new technique called capillary forming is used to manipulate vertically aligned (VA-) CNTs, and to enable their integration in applications ranging from microsystems to macroscale functional films. Capillary forming relies on shape-directed capillary rise during solvent condensation; followed by evaporation-induced shrinkage. Three-dimensional geometric transformations result from the heterogeneous strain distribution within the microstructures during the vapor-liquid-solid interface shrinkage. A portfolio of microscale CNT assemblies with highly ordered internal structure and freeform geometries including straight, bent, folded and helical profiles, are fabricated using this technique. The mechanical stiffness and electrical conductivity of capillary formed CNT micropillars are 5 GPa and 10^4 S/m respectively. These values are at least hundred-fold higher than as-grown CNT properties, and exceed the properties of typical microfabrication polymers. Responsive CNT-hydrogel composites are prototyped by combining isotropic moisture-induced swelling of the hydrogel with the anisotropic stiffness of CNTs to induce reversible self-directed shape changes of up to 30% stroke.

Centimeter scale sheets are fabricated by mechanical rolling and capillary assisted joining of CNTs. The mechanical stiffness, strength and electrical conductivity of CNT

sheets are comparable to those of continuous CNT microstructures; and can be tuned by engineering the morphology of the CNT joints. Finally, the applicability of mechanocapillary forming to other nanoscale filaments is demonstrated using silicon nanowires synthesized by metal assisted chemical etching. Further work using the methods developed in this dissertation could enable applications such as directional liquid transport, adhesives, and biosensors; toward an end goal of creating multifunctional surfaces having arbitrary structural, interfacial, and optical responsiveness.

Chapter 1
Introduction and thesis scope

1. 1 Motivation

Filamentary materials constitute an essential building block used by nature not only to construct different organisms but also to assign to materials their chemical and physical functionality, and in some cases, responsiveness. Natural filaments exist on their own, or in filament-matrix composites, spanning a wide range of length scales, orders and complexities. For instance, in animals, tendons have hierarchical fibrillar vertebrate tissues with fibrous structures at the molecular, nanometer, and micrometer level[1], hence allowing storage and release of mechanical energy and passive enhancement of locomotion stability[2]. In plants, the cellulose fibrils in the cell wall tissue dictate the plant's stiffness and toughness[3], and the gradual change in their orientation from the inner to the outer walls is responsible for the movements associated with plant tropism[3, 4]. Accordingly, various technologies have been developed to manipulate the synthesis and assembly of fibers, in industrial processes spanning from textile combing/weaving, to aerospace composite fabrication (pultrusion, preforming).

While natural filamentary materials comprise hierarchically organized structures, current methods of synthetic filament processing suffer from trade-offs between the filaments size and the level of organization in the final material assembly. Nonetheless, the integration of nanoscale filaments with novel interfacial properties and interactions could enable the synthesis of new materials having outstanding performance and responsiveness. Therefore, the goal of this thesis is to create new techniques for manipulating and forming nanoscale filamentary materials, using synthetic filaments, namely carbon nanotubes (CNTs). These nanoscale filament building blocks have

diameters ranging from approximately 1-100 nanometers and can have lengths up to thousands of microns. While many efforts have been invested in controlling the synthesis conditions to tailor their structure and properties, the main challenge towards the integration of nanoscale filaments in functional materials remains the ability to arbitrary control their location, organization and spacing.

Manipulation of synthetic nanoscale filaments is of interest because of their strong and unique functional properties. For example, synthetic nanoscale filaments such as CNTs[5] and silicon nanowires (SiNW)[6] are under evaluation as potential replacements for conductors and semiconductors in microelectronic and optical devices. Already, the integration of CNTs and SiNWs in transistors,[7, 8] flexible transistors,[9] lasers,[10] solar cells,[11] supercapacitors,[12] batteries,[13] resonators,[14] and interconnect via[15] has demonstrated outstanding performance due to many specific properties and/or combinations of these properties. Additionally, the exceptional high stiffness and strength at low mass density promotes the potential application of CNTs as structural fibers for making Micro- Electro-Mechanical Systems (MEMS),[16, 17] composites,[18] functional coatings, [19] fibers and yarns.[20]

1. 2 Thesis scope

The goal of this dissertation is to **develop methods for the fabrication of new materials and surfaces using highly organized assemblies of nanoscale filaments**. To this end, new methods and tools have been developed to form Vertically Aligned (VA-) CNT and SiNW forests, and to enable their scalable integration in applications ranging from microelectronics and MEMS to macroscale functional films and yarns.

The outcome of this thesis is a portfolio of fabrication techniques that combine methods of controlling the material composition, structural characteristics and architecture of nanoscale filament assemblies (**Figure 1.1**). The mechanisms responsible for changing the material properties according to variations in the aforementioned parameters are investigated.

The material composition axis corresponds to the constituent materials in the filament assembly, which in this thesis are CNTs or SiNWs. The filaments can be coated with polymers or ceramics after growth thus forming core-shell filaments. Finally, the assembly can be filled with polymers to form filament-matrix composites.

The structural characteristics axis manipulates the filament (e.g., CNT) diameter, length, alignment, and density. The structural characteristics of the assembly are also affected by the interactions among the CNTs (e.g. van der Waals attraction) or in CNT-CNT joints.

The architecture axis describes the geometry of the microstructures. This includes their orientation (horizontal, inclined, and vertical) and their 3-D profiles (bent and helical).

Efforts throughout this 3-axis space have been combined to create an understanding of the mechanics of organization and interactions in the fabricated thin-films and complex structures, and to characterize their electrical and mechanical properties.

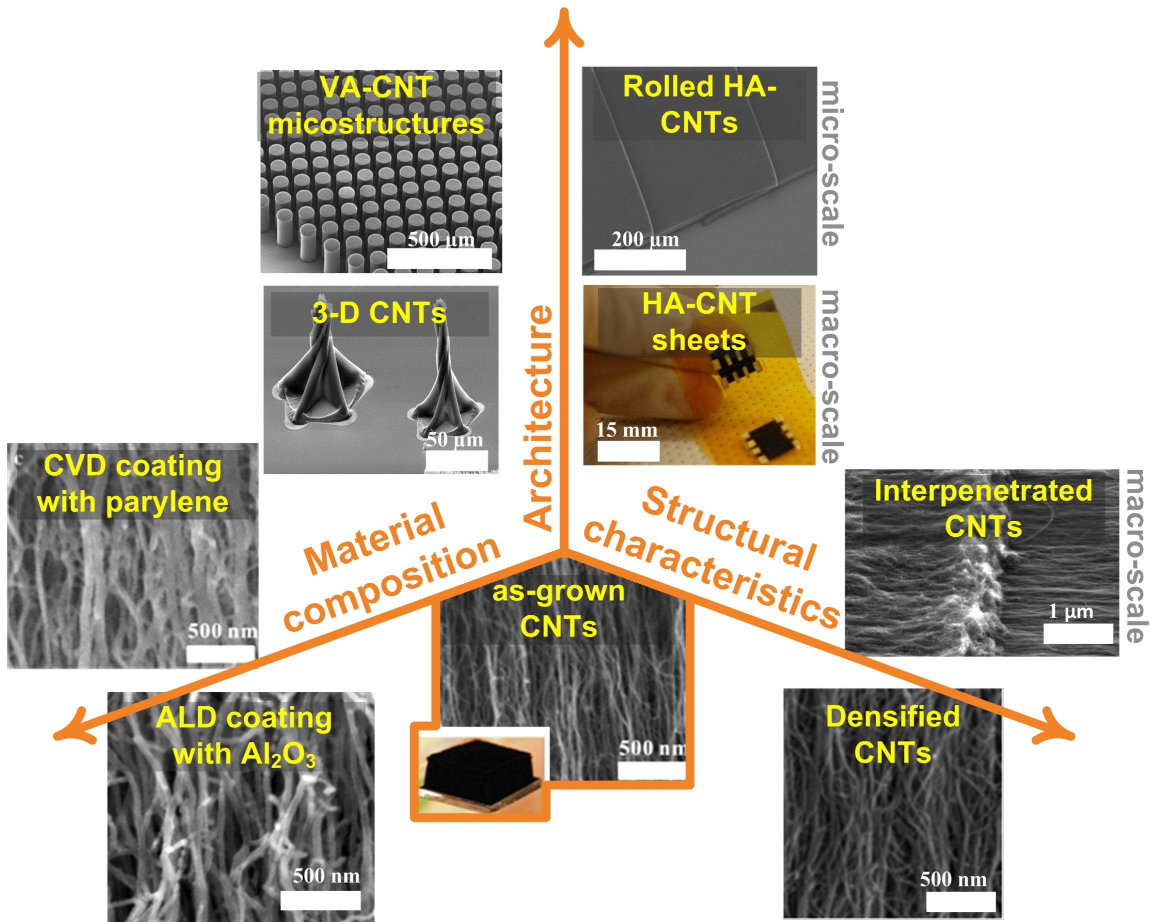

Figure 1.1 Axes of material composition; structural characteristics; and architecture.

1. 3 Thesis outline

The thesis is organized into the chapters as follows:

Chapter 2 reviews the state-of-the art in fabrication of 3-D nano and micro-scale surface topographies in functional materials such as metals and polymers. It highlights the outstanding properties of CNTs and the challenges and potential for their integration in microfabricated surfaces and devices.

Chapter 3 describes the methods and tools developed to fabricate VA-CNT microstructures by chemical vapor deposition from lithographically patterned catalyst, and to coat the microstructures after synthesis with polymers and ceramics.

Chapter 4 presents the fabrication of microscale horizontally aligned (HA-) CNT interconnects by mechanical rolling and dry transfer printing. This process changes the orientation of the VA-CNTs, increases their packing density, and thus enhances their properties. The same technique is also used to make large scale yarns and sheets by overlapping and joining CNTs.

Chapter 5 presents a new process for 3-D microfabrication of filamentary materials, which we call *capillary forming*. Robust 3-D CNTs with dense ordered internal structure and freeform geometries were fabricated from VA-CNTs using controlled elastocapillary aggregation. Solvent condensation and evaporation creates geometric transformations in CNT microstructures by changing the CNT organization on multiple length scales. It establishes the design rules for making a portfolio of 3-D CNT architectures including straight, bent, folded and helical CNT microstructures.

Chapter 6 explains the mechanism of capillary forming. It shows how the equilibrium between capillary forces and CNT elastic restoring forces enables the spatial programming of the 3-D forms. The dynamics of the solvent in manipulating the CNTs are discussed; and the stresses and material properties affecting the organization of the CNTs are elucidated.

Chapter 7 characterizes the electrical and mechanical properties of HA- and 3-D CNTs. It demonstrates the various microfabrication methods to pattern electrodes for electrical addressability to CNTs. Active CNT-hydrogel composite structures are prototyped and tested by combining isotropic moisture-induced swelling of the hydrogel with the anisotropic stiffness of CNTs to induce directed shape changes which can be electrically transduced.

Chapter 8 presents the fabrication of cm-scale CNT films and yarns by mechanocapillary joining of CNT microstructures. The mechanical and electrical properties were measured and validated by comparison to analytical models to enable the prediction of joint properties as a function of their morphologies..

Chapter 9 presents an initial exploration of the synthesis of densely packed SiNW using Metal Assisted Chemical Etching followed by capillary densification. Methods of controlling of the nanowire diameter, density, and aggregated bundle morphologies are presented.

Chapter 10 summarizes the findings and contributions of the thesis, and reflects on future challenges in harnessing the properties of nanoscale filaments in micro- and macroscale assemblies. Fundamental and practical questions for future work are presented, hoping to foster greater understanding of mechanocapillary forming as well as technology transition to important applications in Microsystems and engineered surfaces.

1. 4 Bibliography

1. Fratzl, P.; Burgert, I.; Gupta, H. S., On the role of interface polymers for the mechanics of natural polymeric composites. *Physical Chemistry Chemical Physics* **2004,** *6* (24), 5575-5579.

2. Roberts, T. J.; Marsh, R. L.; Weyand, P. G.; Taylor, C. R., Muscular force in running turkeys: The economy of minimizing work. *Science* **1997,** *275* (5303), 1113-1115.

3. Burgert, I.; Fratzl, P., Plants control the properties and actuation of their organs through the orientation of cellulose fibrils in their cell walls. *Integrative and Comparative Biology* **2009,** *49* (1), 69-79.

4. Elbaum, R.; Zaltzman, L.; Burgert, I.; Fratzl, P., The role of wheat awns in the seed dispersal unit. *Science* **2007,** *316* (5826), 884-886.

5. Iijima, S., Helical microtubules of graphitic carbon. *Nature* **1991,** *354* (6348), 56-58.

6. Morales, A. M.; Lieber, C. M., A Laser Ablation Method for the Synthesis of Crystalline Semiconductor Nanowires. *Science* **1998,** *279* (5348), 208-211.

7. Tans, S. J.; Verschueren, A. R. M.; Dekker, C., Room-temperature transistor based on a single carbon nanotube. *Nature* **1998,** *393* (6680), 49-52.

8. Cui, Y.; Lieber, C. M., Functional Nanoscale Electronic Devices Assembled Using Silicon Nanowire Building Blocks. *Science* **2001,** *291* (5505), 851-853.

9. Cao, Q.; Hur, S. H.; Zhu, Z. T.; Sun, Y. G.; Wang, C. J.; Meitl, M. A.; Shim, M.; Rogers, J. A., Highly Bendable, Transparent Thin-Film Transistors That Use Carbon-Nanotube-Based Conductors and Semiconductors with Elastomeric Dielectrics. *Advanced Materials* **2006,** *18* (3), 304-309.

10. Huang, M. H.; Mao, S.; Feick, H.; Yan, H.; Wu, Y.; Kind, H.; Weber, E.; Russo, R.; Yang, P., Room-Temperature Ultraviolet Nanowire Nanolasers. *Science* **2001,** *292* (5523), 1897-1899.

11. Tian, B.; Zheng, X.; Kempa, T. J.; Fang, Y.; Yu, N.; Yu, G.; Huang, J.; Lieber, C. M., Coaxial silicon nanowires as solar cells and nanoelectronic power sources. *Nature* **2007,** *449* (7164), 885-889.

12. An, K. H.; Kim, W. S.; Park, Y. S.; Moon, J. M.; Bae, D. J.; Lim, S. C.; Lee, Y. S.; Lee, Y. H., Electrochemical Properties of High-Power Supercapacitors Using Single-Walled Carbon Nanotube Electrodes. *Advanced Functional Materials* **2001,** *11* (5), 387-392.

13. Chan, C. K.; Peng, H.; Liu, G.; McIlwrath, K.; Zhang, X. F.; Huggins, R. A.; Cui, Y., High-performance lithium battery anodes using silicon nanowires. *Nat Nano* **2008,** *3* (1), 31-35.

14. JensenK; Kim, K.; ZettlA, An atomic-resolution nanomechanical mass sensor. *Nat Nano* **2008,** *3* (9), 533-537.

15. Wei, B. Q.; Vajtai, R.; Ajayan, P. M., *Reliability and current carrying capacity of carbon nanotubes*. AIP: 2001; Vol. 79, p 1172-1174.

16. Stampfer, C.; Helbling, T.; Obergfell, D.; Sch¶berle, B.; Tripp, M. K.; Jungen, A.; Roth, S.; Bright, V. M.; Hierold, C., Fabrication of Single-Walled Carbon-Nanotube-Based Pressure Sensors. *Nano Letters* **2006,** *6* (2), 233-237.

17. Hayamizu, Y.; Yamada, T.; Mizuno, K.; Davis, R. C.; Futaba, D. N.; Yumura, M.; Hata, K., Integrated three-dimensional microelectromechanical devices from processable carbon nanotube wafers. *Nat Nano* **2008,** *3* (5), 289-294.

18. Shaffer, M. S. P.; Windle, A. H., Fabrication and Characterization of Carbon Nanotube/Poly(vinyl alcohol) Composites. *Advanced Materials* **1999,** *11* (11), 937-941.

19. Wu, Z.; Chen, Z.; Du, X.; Logan, J. M.; Sippel, J.; Nikolou, M.; Kamaras, K.; Reynolds, J. R.; Tanner, D. B.; Hebard, A. F.; Rinzler, A. G., Transparent, Conductive Carbon Nanotube Films. *Science* **2004,** *305* (5688), 1273-1276.

20. Li, Y.-L.; Kinloch, I. A.; Windle, A. H., Direct Spinning of Carbon Nanotube Fibers from Chemical Vapor Deposition Synthesis. *Science* **2004,** *304* (5668), 276-278.

Chapter 2
3-D surfaces and CNTs in microfabrication

This chapter reviews the state-of-the art in fabrication of 3-D micro- and nanoscale surface topographies in functional materials such as metals and polymers. In the past years, several methods of top-down and bottom-up fabrication techniques enabled the engineering of bulk and interfacial properties for microsystems and devices used in energy, electronics, photonics, composite materials, and medical devices. In particular, the fabrication of complex 3-D structures such as inclined and helical pillars is desirable for applications such as directional adhesives and circular polarizers. Recent advances in nanotechnology stimulated the development of various bottom-up techniques to form 3-D surface patterns such as glancing angle deposition and top-down techniques such as self-directed mechanical deformation of microstructures made by traditional lithography, growth or etching methods.

After reviewing these methods, the chapter focuses on the potential use of CNTs as a material for microfabrication. The scaling of the collective properties of aligned CNT assembles from the individual CNT properties according to their packing density is demonstrated by comparing the electrical conductivity of various CNT assemblies from the recent literature with the predicted assemblies properties based on individual CNT properties and their packing density. Important considerations for the integration of CNT synthesis and processing with standard microfabrication are discussed. Finally, examples of the recent advances in the fabrication, integration and application of vertically- and horizontally-aligned CNT configurations in MEMS and 3-D interfaces are presented.

2. 1 Classification and fabrication of 3-D surfaces

3-D microstructures are defined as micropatterns having high aspect ratio (AR >1) and variable geometry along the vertical direction.[1] High AR structures perpendicular to the substrate are considered 2.5-D structures. Exemplary 3-D features include bent, inclined, zigzag, and helical pillars. Fabrication methods enabling the creation of 3-D microstructures are summarized in **Table 2.1**.

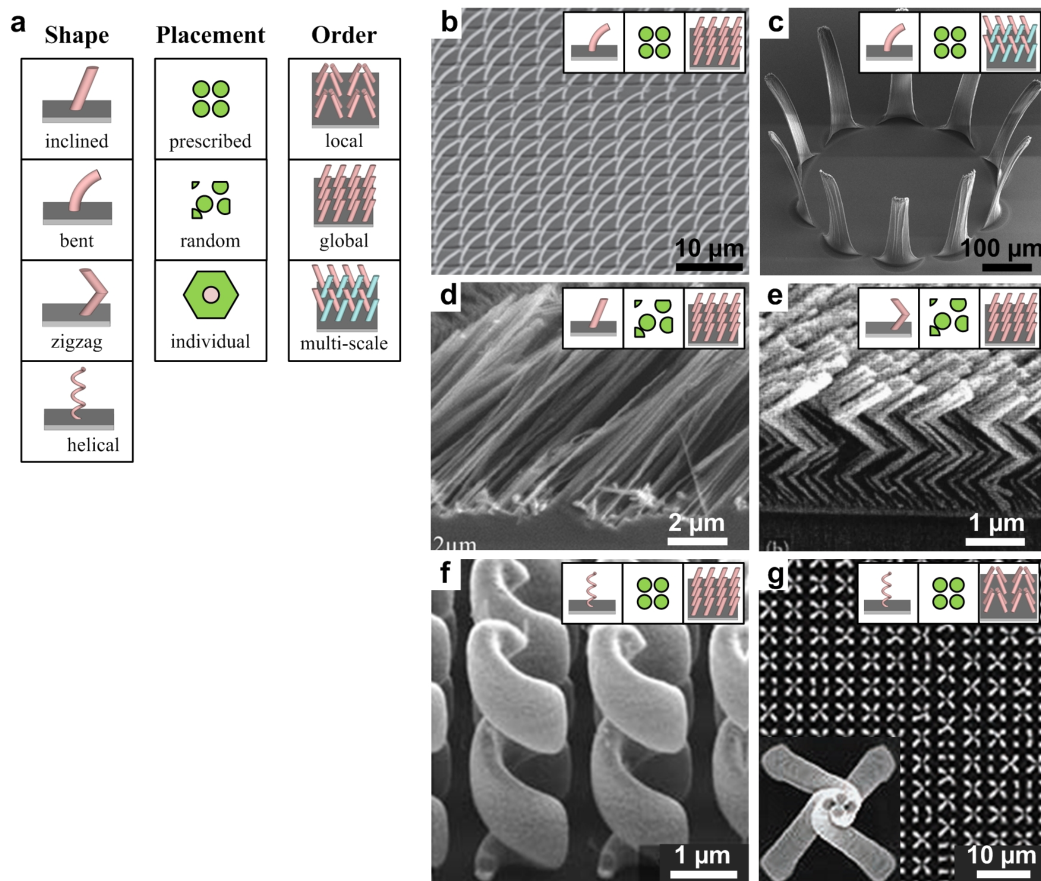

Figure 2.1 Classification of anisotropic surfaces with 3-D features. (a) Legend. (b-g) SEM showing examples of different shapes, placement and order: (b) Uni-directional bent silicon nanowires made by oblique direction deposition of metal films.[1] (c) Multi-directional bent CNT beams made by capillary forming. [2] (d) Uni-directional inclined silicon nanowires made by metal assisted chemical etching. [3] (e) Zigzag MgF_2 nanowires made by glancing angle deposition. [3] (f) Gold helices made by multi-photon lithography.[4] (g) Helical epoxy nanowires made by local capillary self-assembly.[5]

[1] This section is submitted for publication as a Review Article in the journal *Advanced Materials*.

In order to rigorously compare fabrication methods and feature geometries, it is important to establish a consistent nomenclature. Notably, in current literature, the adjectives *tilt*, *bent*, *slanted* and *inclined* are loosely used to describe any non-vertical micro- or nanopillar. In this chapter, the term *inclined* is used to denote a straight but non-vertical feature; and *bent* features are described as having a measurable radius of curvature, which typically results from a stress gradient. Further, the 3-D geometry of *helical* structures made by different methods is difficult to discriminate. Thus the term helical is used to describe any structure (solid or hollow) that makes a generally spiral trajectory about a vertical axis.

Several methods enable fabrication of 3-D structures over relatively large areas, albeit with different levels of control in the placement and order of the constituent features, as well as varying dimensional limits and material capabilities. As a result, 3-D processes are classified according to their ability to control relative position and organization of the features on the surface. Examples are shown in SEM images in **Figure 2.1**, and a related symbology is presented which in turn corresponds to the classification tables. For instance, "top-down" (subtractive) patterns made by photolithography are prescribed, because the position and orientation of each feature follows the design of the lithography mask. Imprinting, replica molding, and etching techniques also result in prescribed patterns because the master template is typically made by lithography. As a result, the size, absolute and relative positions of the structures (and hence their density and order) can be arbitrarily controlled. We note that these methods are prescribed within the allowed resolution (or feature size). For example, photolithography is limited by optical diffraction which make the process non-deterministic beyond this scale; however, the dimensions and location of each feature can be accurately prescribed within this limit.

On the other hand, "bottom-up" (additive) methods typically result in patterns that satisfy energy minimization under certain conditions. As a result, the order of the patterns is most likely local but not global, unless a pre-patterned template is used. Also, the type of ordering (packing) may be determined by the interactions among the features and/or their components. For example, self-assembly of spherical molecules of diblock block copolymer can result in a hexagonally-packed arrangement of cylindrical domains.[6, 7] It cannot result in the square or rectangular arrangement without templates.

Moreover, the size of the building blocks and the spacing between them are coupled; thus the density of the structures can only be indirectly and partially controlled based on the lengths of the polymer. Self-directed mechanical stresses can also lead to self-ordered surface features,[8] such as when micron-sized surface wrinkles are formed due to stress gradients caused by the deposition of thin metal films on *polydimethylsiloxane* PDMS substrates. In both cases, the resulting surface structures have order in small domains, typically called grains or crystals. The relative orientation of different domains is uncontrolled and cannot be deterministically defined.

Table 2.1 Comparison of process capabilities for fabrication of anisotropic surfaces with 3-D features.

Process	Geometry (side view)	In-plane feature size [μm]	Feature placement	Order	Packing density	Aspect ratio (max)	Resolution limited by
Inclined lithography		0.01 0.1 1 10			0 - 1	5	wavelength of light, refractive index of polymer
Multi-photon lithography		0.01 0.1 1 10			0 - 1	10	wavelength of light
Replica molding		0.01 0.1 1 10			0 - 1	20	mechanical robustness of mold
Metal-assisted chemical etching (MACE)		0.01 0.1 1 10	*template		≈ 0.5	100	catalyst size and geometry
Glancing-angle deposition (GLAD)		0.01 0.1 1 10			≈ 0.5	10	interfacial energy between wafer and deposited atoms
Oblique angle polymerization (OAP)		0.01 0.1 1 10			≈ 0.5	10	interfacial energy between wafer and deposited polymer
Oriented nanostructure growth		0.01 0.1 1 10			≈ 0.1	1000	catalyst size and geometry
Capillary densification†		0.01 0.1 1 10		*capillary forming	0.1 - 1	10	catalyst size and geometry
Directed mechanical deformation†		0.01 0.1 1 10			0.1 - 0.5	10	mechanical robustness

† start from straight structures

2.1.1. Inclined lithography

Typically, polymer features made by photolithography have straight sidewalls, and conventional lithography methods do not enable variation of the lateral feature dimensions (i.e., slope, undercut) in the vertical direction. Certain photoresists (PR) such as SU-8 enable the fabrication of high aspect ratio micropillars; however, these remain straight unless special exposure techniques are used.[9] To overcome the limitation of straight features, inclined lithography (IncL) was developed.[10, 11] IncL enables the formation of 3-D geometries such as inclined micropillars and truncated cones, by tilting the wafer with respect to the light source and optionally rotating the wafer and/or the

mask during the exposure. For example, as shown in **Figure 2.2 and 2.3**, Beuret et al. fabricated multidirectional inclined structures in a commercially available thick PR by using an inclined and rotating assembly of two masks and the wafer.[10]

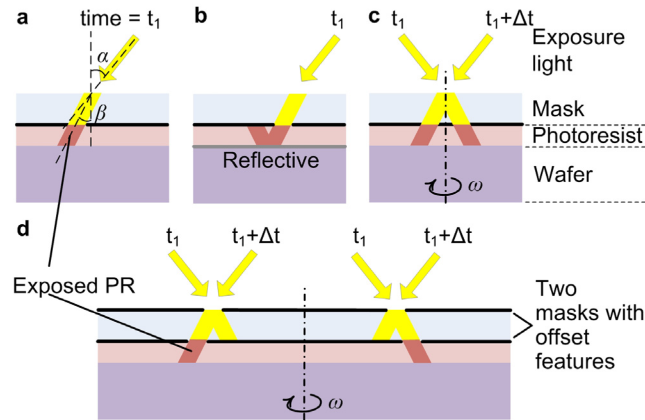

Figure 2.2 Inclined lithography. (a) Fabrication of tilted microstructures by inclined lithography where α is the incidence angle of UV light and β is the microstructure tilt; $\alpha \neq \beta$ because of light refraction. (b) Fabrication of V-shaped inclined structures by increasing the light dosage such that the PR is also exposed in the reflected path. (c) Rotation and/or inclination of the wafer lead to the fabrication of hollow or conical structures. (d) Masks stacks with offset features along with substrate rotation are used to fabricate microstructures with different tilt angles or central holes.

3-D structures made by inclined lithography have lateral dimensions and height (defined by the PR thickness and exposure depth) both in the range of 1-100 microns. For instance, inclined SU-8 pillars with an aspect ratio (height/width) exceeding 4 have been realized in 100 μm thick SU-8. The angle of inclination is limited by the refraction of light entering the mask as shown in **Figure 2.2** and has a theoretical limit in air of ~39°, measured from the normal to the substrate). Immersion lithography can thus achieve larger inclination angles, such as 56.2° in water [12] and 71° in glycerol.[13] The spacing between individual structures can be as small as the feature size, and is also limited by the wavelength of the exposure light. However, to our knowledge, submicron 3-D features made by inclined photolithography have not been demonstrated.

Combinations of standard vertical and inclined lithography allow the fabrication of asymmetric pillars with both straight and inclined sidewalls as shown in **Figure 2.2**.[14] For example, two masks can be stacked (or a double-side mask may be used) such that the two patterns have a desired offset. This configuration enables simultaneous exposure of the PR at different angles by allowing the transmission of UV at the angle defined by

the offset double mask. This technique can also be used to make hollow conical microwells. Additionally, Tabata et al. fabricated solid conical structures in PR using a rotating mask along with a LIGA process.[11] The mask has a clear circle with radius *R* offset from the center of rotation as shown **Figure 2.2**. The difference in exposure dose from the center to edge leads to the formation of the cone. Moreover, when a reflective substrate (e.g. Si wafer) is used, the reflection of the exposure light can result in parasitic patterning of material near the base of the structures. This limitation can also be an opportunity; for example, crosslinking of the SU-8 along the reflected path can give V-shaped geometries (**Figure 2.3**).[15]

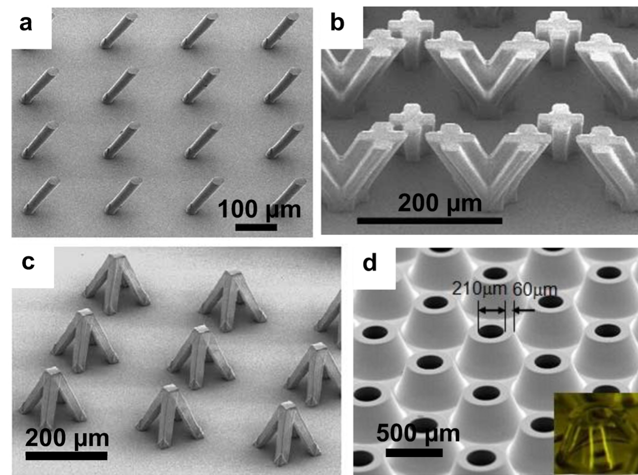

Figure 2.3 SU-8 microstructure arrays fabricated by inclined lithography. Tilted microstructures made by (a) inclined beams made by inclined lithography in air. (b) V-shaped microstructures made by inclinded lithography on a reflective substrate. (c) Microtruss structures made by three discrete inclined exposures with 120° wafer rotation following each exposure.[15] (d) Conical microwells made by inclined exposure and continuous wafer rotation.[16]

Arrays of structures made by inclined lithography have been exploited to create anisotropic wetting or adhesive surfaces. These surfaces have found several applications in microfluidics where they are used as filters, droplet fragmentation devices, truncated microchannels, and 3-D mixing channels.[12, 17-19] The main limitation of anisotropic structures fabricated by inclined lithography remains the performance of the PR as a functional material (and not as a sacrificial material). For example, the mechanical, electrical and thermal properties of most PR are inferior to the properties of metals, silicon or other inorganic materials (**Table 2.2**). Nonetheless, this limitation can be

addressed by coating or infiltration of polymer structures with inorganic films or nanoparticles specially to enhance their surface properties.

2.1.2. Metal assisted chemical etching

Metal assisted chemical etching (MACE) of silicon was first demonstrated in 2003 by Peng et al. for the top-down fabrication of silicon nanowires (SiNWs) form single crystalline silicon wafers as shown in **Figure 2.4**.[20] In contrast to bottom-up growth of SiNWs by chemical vapor deposition (CVD), MACE relies on catalytic etching of silicon wafers in a solution of hydrofluoric acid (HF) in the presence of a metal catalyst and an oxidant. MACE can result in the formation of vertically-aligned or inclined SiNW that follow a specific crystal orientation.[21] Because MACE is a top-down technique, it results in the fabrication of single crystalline SiNW of controlled diameter and orientation when combined with catalyst patterning. SiNWs made by MACE have enabled solar cells with up to 11.4% conversion efficiencies.[2]

Formation of SiNWs by MACE occurs due to the simultaneous oxidation of the silicon surface into SiO_2 at the catalyst-silicon interface, and the anisotropic etching of the formed SiO_2 by the HF solution. Therefore, the projection of the etched area is determined by the arrangement of catalyst on the top surface. The metallic catalyst, which is usually a noble metal such as Ag, Au, or Pt, can be deposited by physical vapor deposition (PVD) on template of self-assembled polystyrene nanospheres, block-co-polymers, or anodic aluminum oxide membranes. When the catalyst metal is deposited on the surface prior to MACE, an etching solution of HF and H_2O_2 (oxidant) is typically used (**Figure 2.5)**. Alternatively, a random etching pattern can be established using a solution of HF with a dissolved metal salt such $AgNO_3$. This causes etching by simultaneous precipitation of Ag^+ ions and formation of an interconnected 2-D network of metal nanoparticles that catalyze anisotropic etching of silicon.

In both cases, the area of the silicon surface that is not covered by the metal catalyst is not etched, thus a forest of vertically aligned or tilted SiNW is formed. MACE using a metal salt solution typically gives SiNWs with 50-200 nm diameter. MACE using an ordered metal mesh as a template gives SiNWs with narrow diameter distributions. For example, masking using nanosphere lithography gave SiNWs with average diameter of

200 nm,[22] a BCP-templated mesh gave 22 nm diameter SiNWs,[23] and using anodic aluminium oxide (AAO) template SiNWs as small as 8 nm diameter[24] were made. In general, the etching rate is ~ 1µm/min and depends on the [HF]/[oxidant] concentration ratio and the etching solution temperature with an optimum temperature ≈55°C.[21]

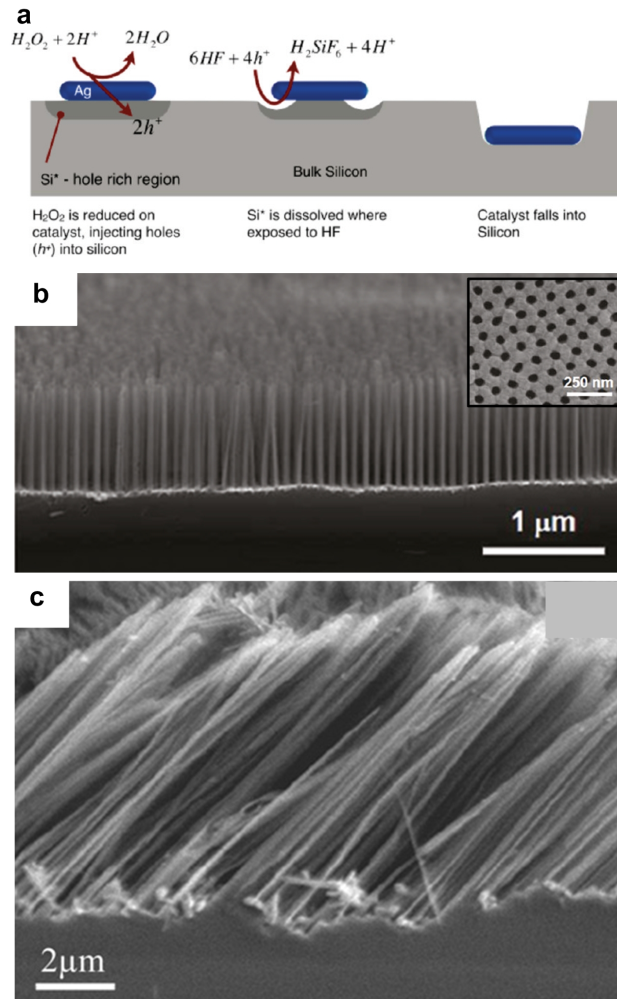

Figure 2.4 Metal assisted chemical etching (MACE) of silicon nanowires (SiNW). (a) Schematic showing the mechanism of MACE using Ag catalyst in HF-H_2O_2 solution. [25] (b) Straight SiNWs fabricated by MACE. Inset shows Au/Ag bilayered catalyst mesh with hexagonally ordered 50 nm holes replicated from an Anodic Aluminum Oxide (AAO) membrane.[2] (c) Slanted silicon nanowires fabricated by MACE of (111) wafer with Ag catalyst mesh and etching solution of 4.6M HF and 0.44M H_2O_2 etching solution.[26]

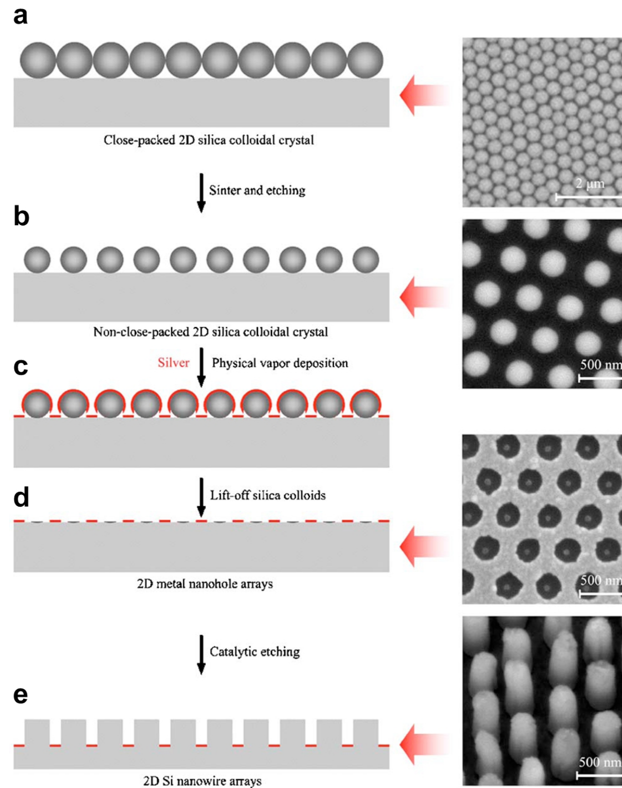

Figure 2.5 Nanosphere lithography (NSL) template for the fabrication of hierarchically ordered SiNWs by MACE. (a) Self-assembly of a monolayer of 500 nm silica spheres on a (100) silicon wafer. (b) Sintering and etching of the nanospheres to reduce their diameter and increase the spacing. (c) E-beam evaporation of Ag film. (d) Lift-off of the silica nanoparticles and the formation of a Ag mesh with 200 nm hexagonally ordered pores. (e) The Ag mesh catalyzes the etching in HF-H_2O_2 solution as it moves down the wafer, and a forest of ordered vertical silicon posts is formed.[22]

Most studies of MACE have produced vertical SiNWs; however, it was recently shown that tilted SiNWs can be formed when the etch chemistry is adjusted to manage the oxidation versus the etching rates of the single crystal wafer substrate.[27] For example, when there is preferential etching in the <100> direction, SiNWs were tilted by β=54.7° and 45° from (111) and (110) wafers, respectively. This preferential etching of the tilted crystal planes occurs only at slow etching rates when using a low concentration of H_2O_2 oxidant relative to the HF concentration. Anisotropic etching perpendicular to the wafer surface occurs at high H_2O_2 concentration. Thus, the etching direction depends on a competition between the total strength of the back bonds of silicon atoms in a particular crystal direction and the relative rates of oxidation and etching at the catalyst-silicon interface. In silicon, the atoms on the {100} plane have two back bonds, while the atoms

on the {111} plane have three back bonds to the atoms underneath them.[27] As a result, it is generally more favorable to dissolve atoms along the <100> direction (⊥ to [28]) for wafers of non-(100) orientation. When the rate of etching of SiO_2 is higher than the rate of oxidation of Si (high [HF]/[H_2O_2] ratio), the etching proceeds in the inclined direction following the <100> direction. Conversely, the Si at the catalyst-Si interface is adequately oxidized at sufficiently low [HF]/[H_2O_2] ratio, insuring anisotropic vertical etching. It is also shown that all the Si back bonds (on the different planes) are generally weakened due the formation Si-OH terminated atoms at high oxidant concentration which effectively suppresses the effect of the back bond anisotropy and leads to vertical etching regardless of the crystal plane orientation. On the other hand, when the solid area of the metal mask is sufficiently greater than the open area, etching according to the crystallographic directions is suppressed and SiNWs are formed perpendicular to the wafer surface due to the limited mobility of the metal catalyst.

In addition to vertical and tilted etching, in- and out-of-plane rotation and folding of catalyst meral patterns have been demonstrated using MACE to fabricate 3-D Si geometries as shown in **Figure 2.6**.[25, 29, 30] Star-shaped catalyst geometries were defined by e-beam lithography and rotation of the start-shaped catalyst along the vertical etching direction was obsereved for a wide range of [HF]/[H_2O_2] etch ratios thus creating a spiral. The mechanism can be explained by local variability in etching rates depending on the geometry of the catalyst boundary. In particular, line width has been identified as an important factor which is correlated to the etching rate. The mechnism of geometry-dependent etching rate in MACE is not understood, but speculations about electrophoretic forces driving the motion of the catlyst layer can explian the etching trajectories and catlyst deformations observed in recent studies.[30]

Because it can directly form vertical or tilted nanowires with controlled diameters over large areas, MACE is potentially advantageous over CVD growth of SiNWs because it does not require high temperature conditions. The ability to form inclined NWs is particularly advantageous for fabrication of smart materials, including anisotropic adhesives and wetting surfaces. However, more studies are needed on fabrication of structures with variable local densities, and different heights and geometries on the same substrate, which would be important steps toward 3-D surface engineering using MACE.

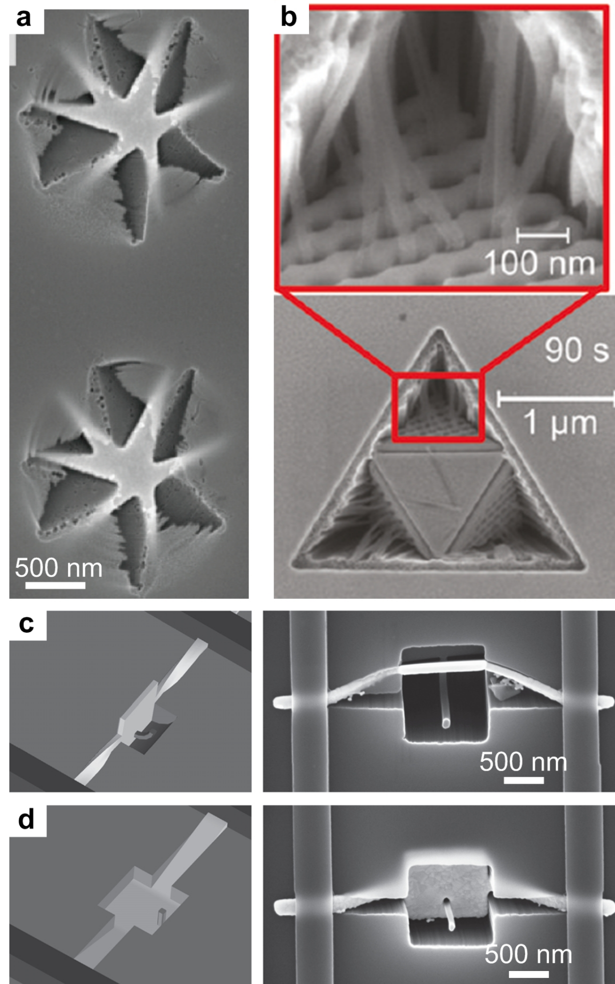

Figure 2.6 3-D silicon etching by MACE. (a) Spiral etching trajectories from rotation of a star-shaped Ti-Au catalyst pattern. [25] (b) Etching from folding of a triangular-shape catalyst, with close-up view of SiNWs protruding from the folded triangular catalyst.[29] (c) Curved etching trajectory from of a square-shaped catalyst with two lateral arms (width = 164 nm) fixed by photoresist lines (vertical stripes in image). Left is 3-D CAD model, and right is SEM image. (d) Same as (c) but arm width is 210 nm.[30]

2.1.3. Glancing angle deposition

Glancing angle deposition (GLAD) is a physical vapor deposition (PVD) technique typically used to sculpt 3-D nanostructured anisotropic thin films. GLAD attracted widespread interest in 1996 when Robbie *et al.* fabricated helically structured films of MgF_2 as shown in **Figure 2.7d** and reported the capability of these films to rotate the plane of polarization of transmitted light.[31]

GLAD is based on the local shadowing effect that arises when the target substrate is tilted **(Figure 2.7)** such that the angle between the normal to the substrate and the incident vapor flux is $\alpha \geq 80°$.[3] GLAD therefore enables self-organization of anisotropic surface features by a combination of chemical and physical effects that govern the nucleation and growth of the deposited films. The geometry and density of the deposited structures are determined by both physical and chemical effects.

GLAD anisotropic structures grow when the substrate and source material interact such that Volmer-Weber growth occurs.[32] This occurs when the newly condensing adatoms have a greater affinity to one another than to the substrate, thus forming isolated microscopic islands on the substrate. As deposition proceeds, the islands locally shadow the ballistic vapor flux from the source, which leads to vertical growth of the islands into individual 3-D structures. Hence, the nucleation and growth dynamics are governed by the source-substrate interfacial interactions and the mobility of the deposited material on the substrate, which in turn are dependent on the substrate temperature and surface roughness.

Moreover, rotation of the substrate during GLAD enables the controlled formation of four types of archetypal pillar structures, as shown in **Figure 2.7b-e**: straight, tilted, zigzag, and helical. A substrate fixed at an angle α leads to the growth of pillars tilted by at an angle β. To create zigzag pillars, the substrate tilt is changed from $+\alpha$ to $-\alpha$ after a given deposition time which determines the thickness of each segment. Continuous rotation during deposition will cause formation of helical structures with a vertical pitch dependant on the deposition and rotation rates. At high rotation rates, the pillars grow perpendicular to the substrate, thus forming straight pillars.

The lateral dimensions of GLAD structures are typically in the range of 10-1000 nm. The height is typically heights are in the range of hundreds of nanometers to a few microns. The column spacing *a* is comparable to the feature size, and can be estimated as

$$a = (1 + 1/\cos\alpha)\delta \qquad \text{Eq. (2.1)}$$

where δ is the is the column diameter.[33] This simple relation takes into consideration only the geometrical shadowing effect and not diffusion of the deposited material.

GLAD structures can also grow from pre-patterned seeds where photolithography can be used to control the position and density of the based on the position of the seeds.[34]

For angled or helical columns, it was found that the angle (β) can be related to the substrate tilt angle (α) as

$$\beta = \alpha - \sin^{-1}\left[\left(1-\cos\alpha\right)/2\right] \qquad \text{Eq. (2.2)}$$

For example, for β = 89°this equation predicts a minimum tilt angle of 30° (measured relative to the substrate plane).

In principle, all materials that can be deposited by PVD can form GLAD structure morphologies. Reported examples include metals (Al, Ag, Bi, C, Co, Cr, Cu, Mg, Mn, Ni, Pt, Ti,W, Zn), semiconductors (Si, Ge), and compound semiconductors (MgF_2, CaF_2, ITO, SiO_2, SiO, ZrO_2, MgO, YBCO, ZnO, TiO_2, WO_3).[35]

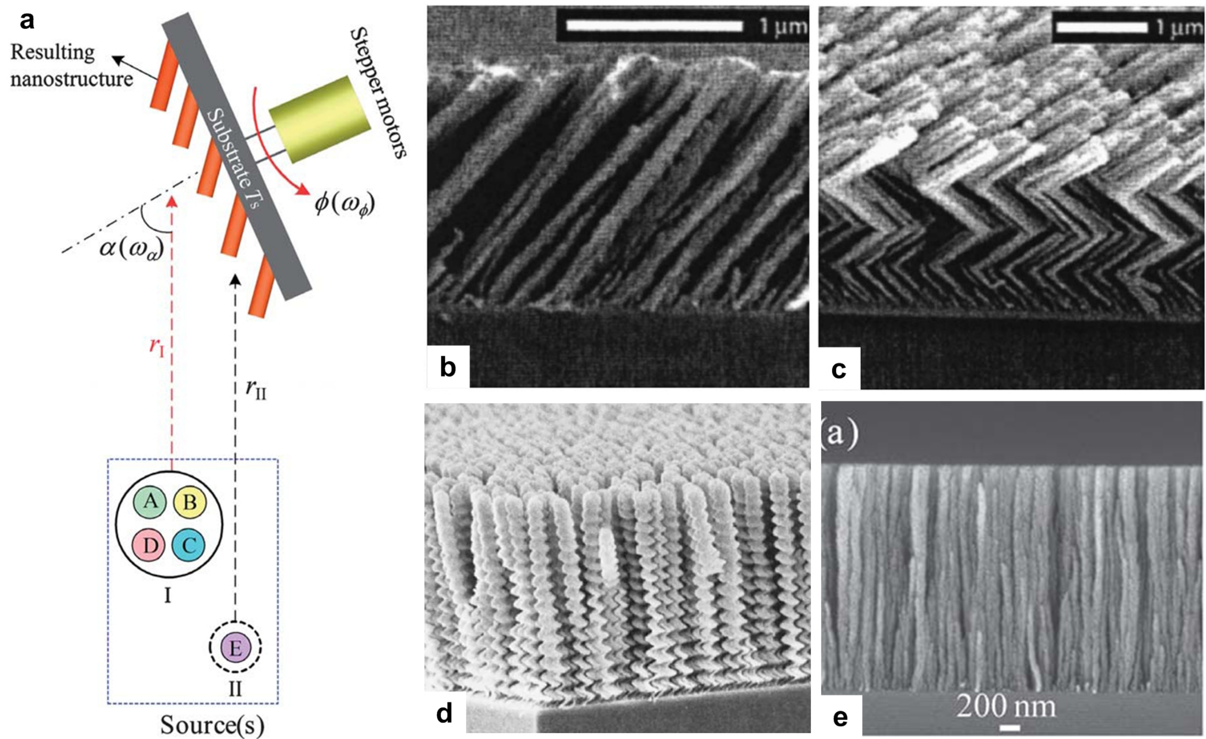

Figure 2.7 Glancing Angle Deposition (GLAD). (a) Setup of the substrate with tilt and rotation capability, and illustration of shadowing effect and growth of tilted pillars. The four archetypal structures of GLAD: (b) Tilted pillars (MgF2) (c) zigzag pillars (MgF2) (d) helical pillars (MgF2), and (e) straight pillars (Si).[3, 31, 35]

2.1.4. Oblique angle polymerization

Oblique Angle Polymerization (OAP) is analogous to GLAD except that polymer precursors polymerize into individual anisotropic structures on the surface of a substrate. OAP was first introduced by Pursel et al. in 2005 who showed the formation of helical structures by *in situ* polymerization.[36] For OAP, a nozzle is typically directed at a shallow angle (≈10°) with respect to the substrate, in contrast to being perpendicular to the substrate in tradition polymer CVD. Notable applications of OAP include surfaces with anisotropic wetting and adhesion,[37, 38] and templates for metal deposition that enable biosening by Surface Enhanced Raman Spectroscopy (SERS).[39]

In the case of parylene deposition by OAP, a dimer is evaporated at 150 - 175°C and then pyrolized into a monomer precursor resulting in a chemical structure such as poly-p-xylene (PPX) that leaves the nozzle at pressure of ≈10 mTorr.[36] Because the flux is directed onto the substrate at a shallow angle, a network of molecular strands nucleates on the substrate without forming a continuous film due to shadowing effects. (**Figure 2.8**) The strands then start to aggregate into columns of 200-400 nm diameter, which are tilted with respect to the substrate. The density of the columns is $\sim 10^7$ mm^2. The tilt angle is a function of the nozzle orientation and is approximately 55° for a nozzle directed at 10° with respect to the substrate. When the substrate is rotating, helical structures with a pitch of ≈ 2 μm can be formed. Detailed analysis of the effect of deposition parameters on the structure of OAP films is reported by Cetinkaya and Demirel.[40] Pursel et al. demonstrated OAP in a commercial polymer PVD system with modifications including the insertion of a 1/4″ diameter nozzle for precursor injection, and the addition of the substrate rotation and tilt motors. The dimer used was para-chloro-xylylene, and the deposited polymer consisted of a benzene ring with two para-methylene groups and one chlorine side group, having the chemical formula C_8H_7Cl. Demirel et al. used chloro-[2.2]paracyclophane dimer to fabricate slanted columns of poly(chloro-p-xylylene) (PPXC) having 50-100 nm diameter and up to 50 μm thickness with an inclinaton angle of 45°.[41] Cetinkaya et al. demonstrated columnar nanostructures of poly(chloro-*p*-xylylene) and poly(bromo-*p*-xylylene) thin films, and co-deposition of nanostructured poly(*o*-trifluoroacetyl-*p*-xylylene-*co*-*p*-xylylene).[41, 42]

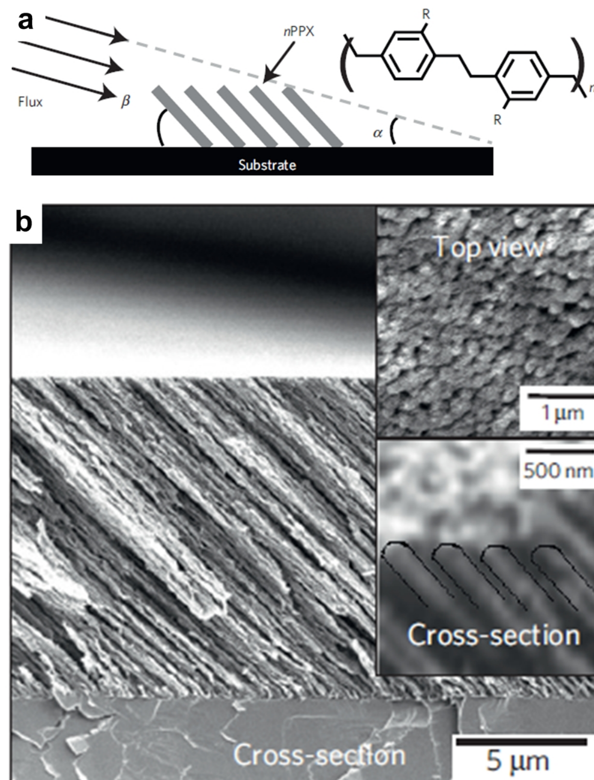

Figure 2.8 Oblique angle polymerization (OAP). (a) Growth of tilted PPX nanopillars from a dimer flux directed at a shallow angle with respect to the substrate. (b) SEM images of a film of tilted PPX nanopillars, with insets showing top view and cross-section at higher magnification.[37]

2.1.5. Directed mechanical deformation

Arrays of bent pillars can also be fabricated by a number of methods that first create straight pillars, and then apply asymmetric stresses to cause bending.[1, 43-45] In the first fabrication step, vertical micro- or nanopillars are fabricated by etching or molding from a master template. Exemplary studies have used pillars with diameter 0.1-1 μm and height of 1-10 μm. The pillars are subsequently bent by directional metal deposition, electrochemical coating, e-beam irradiation, thermal treatment, or a combination of these methods. This step induces a stress gradient across each pillar, causing bending due to a mechanical effect analogous to the thermal actuation of a bimetallic strip. These anisotropic arrays have found applications in unidirectional wetting,[1, 43] anisotropic adhesion,[46] chemical and biological sensing, and actuation.[45]

Kim et al. demonstrated several approaches to make bent polymer nanohairs for applications in unidirectional wetting and dry adhesives.[46] First, they fabricated a silicon

master template using lithography and deep reactive ion etching (DRIE) as shown in **Figure 2.9a**.[44] The holes were 100 nm diameter and 1 μm deep, with tapered side walls as an inherent result of the DRIE process. The silicon master was treated with a self-assembled monolayer of low surface energy molecules ([$CF_3(CF_2)_5CH_2CH_2SiCl_3$]) to aid demolding. Three polymers were used for molding: soft polyurethane PUA (E = 19.8 MPa), hard PUA (320 MPa), and Teflon (1.9 GPa). Drops of uncured polymer were dispensed on the master and pressed with a flexible poly(ethyleneteraphthalate) (PET) film (50 μm thickness) that functioned as a mechanical support during demolding. The liquid polymer filled the master by capillary effects while being cured, and this process was called capillary molding. After demolding and curing the polymer, a 4 nm thick film of Pt was deposited on the polymer nanohairs by e-beam evaporation to prevent electron charging during e-beam irradiation. Bent nanohairs were formed by irradiating the metal-coated array in a Field Emission Gun Scanning Electron Microscope (FEG-SEM) at an angle of 30° with a voltage of 5-15 kV, for up to 40s. The authors attributed the e-beam induced tilting to decomposition of the C=O groups into CO_2 (which outgases), subsequent shrinkage of the portion of each pillar that was penetrated by the e-beam.[47] Moreover, local shadowing of the e-beam by the nanohairs affected the final bent shape. Seminara et al. also studied nanopillar bending due to SEM beam exposure, and found that electrostatic forces resulting from charging and induction caused the pillars to return to the vertical when the beam intensity was reduced.[48] However, when two or more pillars touched during irradiation, they remained bent due to van der Waals forces that overcame elastic restoring forces. At lab scales, both of these techniques are serial (as limited by the field of view of the e-beam at the required intensity) and relatively expensive because of the high operation costs for most commercial FEG SEM systems.

Directional thermal stresses provide a more scalable method for bending of nanohair arrays. For example, Yoon et al. coated PUA nanohair arrays with 6-12 nm Pt by oblique e-beam evaporation.[49] Annealing for 30 minutes at 120°C caused bending of the pillars to ≈20° from their initial vertical orientation, and these bent pillars had directional adhesion properties. The authors noted that the pillars bent toward the metal-coated side upon thermal annealing, (most likely because of greater thermal expansion of the polymer. Upon e-beam irradiation, the pillars bend toward the polymer side. Chu et al.

presented a different approach where metal was deposited on Si pillars at elevated temperature (up to 1000°C).[1] Internal stresses resulting from the mismatch in thermal expansion coefficient caused the pillars to deflect upon cooling to room temperature. The bending angle was controlled from 2-52 ° depending on the thickness of the Au film (250-400 nm).

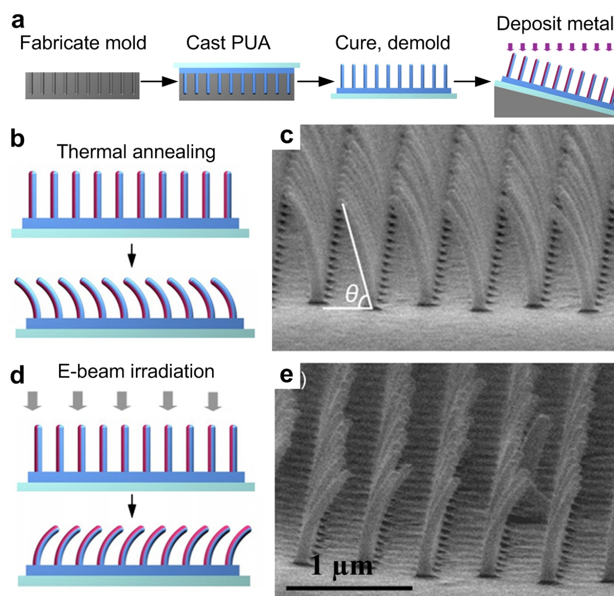

Figure 2.9 Fabrication of bent nanohairs by self-directed mechanical deformation: (a) Fabrication process for PUA nanohairs with oblique metal coating. (b) Bending towards metal-coated side, induced by thermal annealing. (c) SEM image after process (b). (d) Bending towards non-coated side, induced by e-beam irradiation. (e) SEM image after the process shown in (d).49

Stresses generated during anisotropic electrodeposition can also induce bending of polymer nanopillars. Kim et al. used UV-curable epoxy resin (UVO114, Epotek) to make straight nanopillars using a PDMS mold.[45] After demolding, the nanopillars were coated with 30-100 nm thick Au film by oblique e-beam evaporation or sputtering. The metal film deposited on only one side of the pillar arrays due to shadowing effects. This film functioned then as the electrode for deposition of PPy from an aqueous solution containing 0.1 M pyrrole (Py) and 0.1 M NaDBS (0.5-0.7 V vs Ag/AgCl reference electrode). As selective deposition of the PPy progressed on each pillar, the resulting mechanical strain gradients caused the nanopillars to bend in one direction.

Active anisotropic surfaces are a class of materials having reversibly anisotropic building blocks which respond to external stimuli by changing their shape. For example,

flexible polymer nanopillar arrays embedded in a hydrogel matrix can change their shape –anisotropically- due to isotropic expansion of the hydrogel.[50] The nanopillars can thus tilt in one direction as the hydrogel expands and straigthten back up as it re-contracts. By changing the chemistry of the hydrogel, these surfaces can respond to electric, chemical, or light stimuli.[51] These active composite surfaces can have many applications in photonics, wetting surfaces, and microfluidics, where the structural geometry and the resulting performance anisotropy can be reversibly controlled.[52]

2.1.6. Oriented nanostructure growth

Synthesis of aligned one-dimensional (1-D) nanostructures such as carbon nanotubes (CNTs) and semiconducting or oxide nanowires (NW) allows the bottom-up fabrication of high performance anisotropic thin films from organic and inorganic materials. Typically, such nanostructures grow from catalyst nanoparticle "seeds" or nanoscale surface features by gas or liquid phase methods such as chemical vapor deposition (CVD), plasma enhanced CVD (PE–CVD), supercritical, or electrochemical deposition. In general, the geometry and orientation of a 1-D nanostructure is determined by the precipitation reaction and/or by external forces that act on the structure during growth. External forces can be from the synthesis environment (e.g. gas flows or applied electric fields), the substrate, and/or from neighboring structures (i.e., van der Waals interactions). An overall challenge in bottom-up fabrication of 1-D nanostructures with anisotropic organization is the development of scalable approaches for defining the position and spacing of the individual nanostructures over large areas.

In principle anisotropy of individual 1-D nanostructures can be controlled by the motion of the catalyst particle, and model systems are seen with inorganic NWs particularly SiNWs. Tian et al. demonstrated a strategy to fabricate zigzag SiNWs with deterministically placed kink locations and angles (**Figure 2.10**).[53] By Au catalyzed VLS synthesis, 120° kinks were introduced at pre-determined intervals by purging the growth furnace for 15 s, then reintroducing the growth gases. The growth gases were SiH_4 and H_2 at a pressure of 40 Torr; and during purging, the flows were stopped and the chamber was pumped down to 3 mTorr. Purging dropped the reactant concentration in the super-saturated catalyst seed, and reintroducing the growth gases led to the saturation of the

catalyst seed and heterogeneous nucleation of the kink segment. The angle of the kink was dictated by the most thermodynamically favorable growth direction according to the Si crystal structure. Additionally, pinetree-like lead sulfide (PbS) nanostructures were made using CVD, by Bierman and Lau et al..[54] The growth of this complex architecture was attributed to a screw dislocation along the axial trunk (**Figure 2.10**).[55] According to Eshelby theory, an axial screw dislocation exerts a torque at the free ends of the trunk, resulting in the twist of the rod along the axial direction.[56] Zhang et al. fabricated SiO_2 helical nanowires by CVD and attributed their formation to asymmetric growth chemistry around the catalyst.[57] Wang et al. fabricated high dense helical SiO_2 NW forests by the liquid-vapor-solid mechanism using a gold catalyst with contact angle anisotropy (CAA),[58] where the deposition temperature was 350°C.[59] CAA occurs when the catalyst size is larger than the NW size and the center of mass of the catalyst is shifted with respect to the NW center of mass. This in turn leads to CAA and hence asymmetric work of adhesion for new atoms attaching on the catalyst-NW interface (NW growth), which results in asymmetric growth rates across the NW. Nanosprings have also been made from boron nitride and silicon carbide.[58, 60]

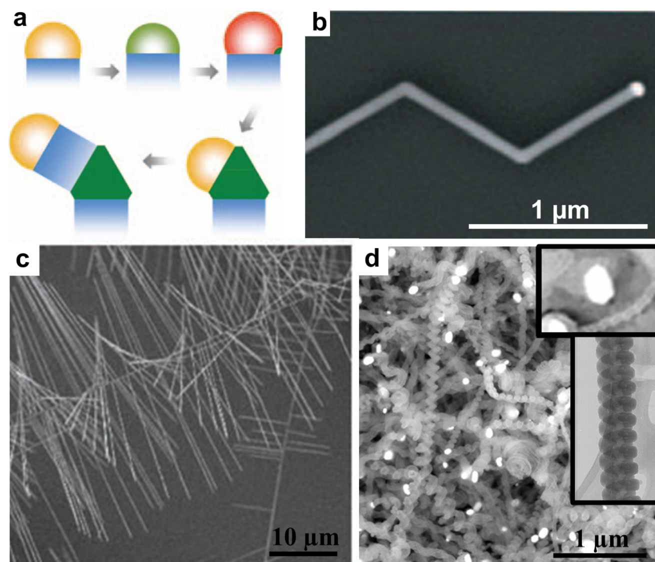

Figure 2.10 Complex morphologies of inorganic NWs. (a) Deterministic formation of kinked SiNWs by purging, re-introduction of reactant, joint growth, and subsequent arm growth. (b) Kinked SiNW segment made by pulsed method.[53] (c) Pine tree PbS NW made by VLS.[54] (d) SiO_2 nanosprings grown from Au catalyst. Inset shows catalyst particle and TEM image of helical SiO_2 NW.[59]

Because of the widespread work on CNT synthesis for different applications, many methods have been developed to control both the anisotropic organization and the individual structure of CNTs. CNTs can be synthesized on substrates in the horizontal orientation (parallel to the substrate) or vertical orientation (perpendicular to the substrate), depending on their interaction with neighboring CNTs and with the substrate. In common CVD methods, CNTs grow from nanoparticle seeds in the tip- or base-growth mode, described by, respectively, whether the catalyst nanoparticles are advancing with the tip of the CNT or pinned to the substrate. In the tip growth mode, the convective gas flow on the substrate can lift the particles and align the CNTs with the flow direction. The alignment of the CNTs to the substrate can also be caused by van der Waals interactions between the CNTs and the substrate. As a result, HACNTs have been grown directly on crystalline substrates, such as ST-cut single crystal quartz and a-/r-/c-plane sapphire. On sapphire, atomic step edges (a few angstroms high) become faceted upon annealing, and physically guide CNTs during growth.[61] However, in all these methods the density of horizontally-aligned CNTs is still low (10-50 CNTs/µm). Recent reports demonstrate how the density can be increased by optimizing the gas-catalyst combination,[62] doing multiple re-growth cycles,[63] or transfer printing.[64] Nevertheless, in order to be a potential replacement for Cu as horizontal interconnects in CMOS chips, CNTs must be made at much higher packing densities and with enhanced control of local position and orientation. Other applications of anisotropic films of HACNTs include RF transistors, flexible devices and interconnects, and polarization-sensitive near field detectors.[65, 66]

When the catalyst seeds are densely distributed on a 2-D planar substrate, CNTs self-assemble into "forests" of vertically aligned (VA) CNTs.[67] VA-CNT can be synthesized by thermal or PE-CVD from a variety of catalysts such as Fe, Co, or Ni, which are often supported by a layer of Al, Al_2O_3, SiO_2, or Ta. The density of the CNTs in this configuration is usually low (<5% by volume) but the length can reach several millimeters.[68] VACNTs can be transformed to HACNTs by mechanical rolling and capillary folding.[69, 70]

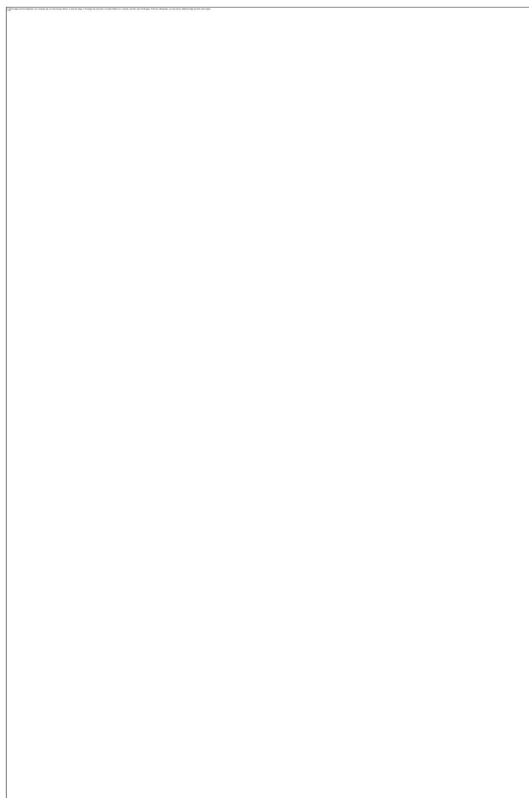

Figure 2.11 3-D CNT morphologies. (a) Zigzag CNTs fabricated by PECVD.[71] (b) Helical CNTs fabricated by CVD from Ferrocene-In catalyst precursor.[72]

In addition to the classic anisotropic vertical morphology, CNTs provide examples of the ways that anisotropy can be engineered using intrinsic (catalyst motion) and extrinsic (external force) growth effects. AuBuchon et al. demonstrated growth of anisotropic bent and zigzag carbon nanofiber morphologies by controlling the direction of an electric field applied during growth (**Figure 2.11**).[71] This morphology was achieved by DC PECVD with Ni catalyst particles and a mixed gas of ammonia (NH_3) and acetylene (C_2H_2). The CNTs followed the tip growth mode, and the field direction was changed by moving conducting plates that changed the direction of electric field lines in the vicinity of the substrate, thus exerting different forces on the catalyst particles. Bajpai and Dai et al. demonstrated the large scale synthesis of VA-CNTs having a helical morphology by controlling the gas-catalyst interaction (intrinsic effect).[67] To achieve this morphology, co-pyrolysis of $Fe(CO)_5$ was performed at 1000°C with a mixture of Ar and H_2 flow. They attributed the formation of the helical structure to the insertion of carbon dimers C_2 into the C_6 hexagonal ring, which led to the formation of two pentagon and heptagon

pairs.[73] Subsequent insertion of C_2 into the heptagon pairs shifted the geometry thus forming the helical twist. The diameter and pitch of the CNT helices were approximately 100 nm and 500 nm respectively. Thermal CVD on substrate bound Fe catalyst nanoparticles was also be used to fabricate helical CNTs, though the alignment was poor compared to the co-pyrolysis method.[74] CVD of helical CNTs from floating catalyst was achieved by injecting xylene-ferrocine mixture having dissolved indium isopropoxide and tin isopropoxide (sources for In and Sn respectively) in a CVD furnace (Figure 2.11). Formation of helices was explained by asymmetric growth on compound catalyst nanoparticles (Fe-In) due to different carbon precipitation rates in the segregated phases of the particle.

2. 2 Aligned CNTs in microfabrication

Carbon nanotubes (CNTs) are known for their outstanding properties including high stiffness and strength at low density and high electrical conductivity and current carrying capacity as described in **Table 2.2**. They are considered potential building blocks for use in microfabrication and engineered surfaces. In particular, highly ordered assemblies of densely packed CNTs are expected to enable the synthesis of new materials having outstanding performance for micro- and macroscale applications. However, current methods of CNT synthesis have inadequate control of quality, density and order. Comparison of notable microfabrication materials to CNTs is summarized in **Table 2.2**.

To this end, previous research has demonstrated synthesis of CNTs in tangled, VA-[75] and HA- configurations. The latter two configurations are the focus of this review section (**Figure 2.13**). Despite seminal advances in CNT synthesis, the integration of aligned CNTs is still hindered by many practical processing considerations. Accordingly, several processing challenges and considerations, in addition to opportunities of the integration of VA- and HA- configurations are discussed in this section.

Table 2.2 Comparison of some microfabrication material properties with CNTs

Material	Mechanical stiffness [GPa]	Mechanical strength [GPa]	Electrical conductivity $[m\Omega\text{-cm}]^{-1}$	Heat conductivity [W/m-K]	Melting/ Oxidation temperature [°C]
Si	112	7	=*f* (doping)	149	1414
SiO_2	70	0.8	low	1.4	1700
Si_3N_4	310	3	low	30	1900
SiC	410	3.9	low	120	2730
Cu	115	0.4	590	380	1084
Au	44	0.1	4550	301	1064
Al	69	0.3	370	170	660
Al_2O_3	300	2.1	low	18	2072
SU-8	2-4	0.05	low	<1	250
PDMS	<.001	0.002	low	<1	250
PMMA	1-3	0.04-0.08	low	<1	< 200
Parylene	3	0.07	low	<1	290
SWCNT	1250	20	500	3500	600
MWCNT (dia. nm)	1049 (15)	100 (15)	1000 (100)	2000 (9.8)	600

2.2.1. Properties scaling of CNT assemblies

An example of the challenges and opportunities of potential aligned CNT applications is considered by examining the integration of CNTs in microelectronic interconnects. In particular, dense assemblies of aligned CNTs are evaluated as replacement to copper interconnect via, as suggested by the International Roadmap of Semiconductors (IRS)[76]. Theoretical and experimental studies confirm that CNTs are resistant to electromigration at emerging Complementary Metal Oxide Semiconductors (CMOS) linewidths, have μm-scale electron mean free path and have higher current carrying capacity than Cu (10^9 A/cm^2)[77]. Therefore, highly organized CNTs are expected to replace Cu in both vertical and horizontal microelectronic interconnects. Growth of VA-CNT forests is an effective means of orienting large numbers of CNTs in an aligned configuration; however, the packing fraction of high-quality VA-CNTs is typically 1-2% and no more than 10%, which is insufficient for electronic applications. Notable previous electrical measurements of individual CNTs and CNT assemblies are summarized in **Figure 2.12** and **Table 2.3**.

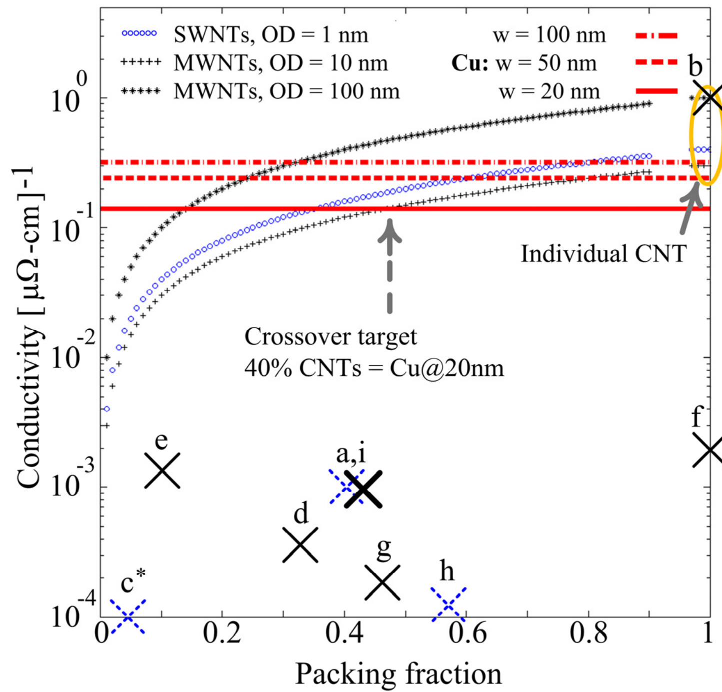

Figure 2.12 Previously published values of CNT electrical conductivity. Calculations of conductivity as a function of the CNT packing fraction are compared to previously measured electrical data for individual CNTs and CNT networks. The packing fraction is defined as the as the ratio of the CNT areal density (number of CNTs/cm^2) to the areal density of hexagonally packed CNTs (modeled as cylinders) having the same outer diameter. Solid and dashed X marks are MWCNT and SWCNT respectively. We assume that the conductivity of aligned CNT network is linearly proportional to the number of CNTs per unit cross-sectional area, and that the constant of proportionality is the conductivity of an individual CNT. Data point (i) is for the HA-CNT ribbons described in Chapter 4 and 7 of this thesis.

Table 2.3 Details of CNT electrical data plotted in Figure 2.12, cited from previous studies of individual CNTs and CNT assemblies.

Label in Figure 2.12	CNT type	Diameter	Packing fraction	Resistivity [mΩ.cm]	Ref.
a	SWCNT	1.3 nm	0.4	0.91	[78]
b	MWCNT	100 nm	individual	10^{-6}	[79]
c*	SWCNT	1 nm	0.01	33	[66]
d	MWCNT	12 nm	0.33	2.5	[80]
e	MWCNT	7 nm	0.10	0.7	[81]
f	MWCNT	70 nm	individual	$5x10^{-4}$	[82]
g	MWCNT	15 nm	0.45	5	[83]
h	SWCNT	2.8 nm	0.58	8	[84]
i	MWCNT	10 nm	0.42	1	†

* values of packing and resistivity were scaled linearly to fit within the axis limits of **Figure 2.12**
† average of measurements (discussed in Chapter 7) taken on bundles fabricated by the method presented in Chapter 4

Figure 2.12 shows the predicted electrical conductivity of aligned CNTs as a function of packing density, compared to Cu. The CNT performance is based on values of conductivity and mean free path measured for individual CNTs. The packing fraction of CNTs is a measure of the density of aligned CNTs. The packing fraction is the ratio of CNTs per unit area to maximum number of CNTs per area in a hexagonally packed configuration. This data suggests that CNT microstructures having packing density exceeding 40% could have higher conductivity than 20nm linewidth Cu, and that tightly-packed CNTs could outperform 50nm linewidth width Cu. While theoretical performance has been matched by measurements of individual CNTs, the measured electrical conductivity values of CNT films to date are typically at least two orders of magnitude lower than what theory predicts for transport through continuous aligned CNTs at the same packing fraction. The practical packing fraction hence remains one of the main challenges towards the integration of CNTs in future devices. Processing temperatures and gases are among other challenges hindering the integration of CNTs in microelectronics as discussed in the next section.

2.2.2. Integration considerations of VA-CNT

The methods of growth and architecture of VA-CNT are discussed in **Section 2.16** and the details of the CNT growth methods used in this thesis are presented in **Chapter 3**. Here, the focus is on the essential considerations for the integration of the VA-CNT configuration in devices.

Synthesis conditions:

VA-CNTs are synthesized by CVD at pressures ranging from a few Torr to atmospheric pressure. The temperature is typically 600-900 °C but can be as low as 450°C using plasma enhanced CVD[85]. Low pressure growth enables more precise dynamics controlled gas environment and hence better control of CNT diameter and growth rate. CMOS-compatible processing can be achieved using remote plasma and/or dedicated thermal decomposition of the precursor gas, along with use of suitable metal catalyst materials.

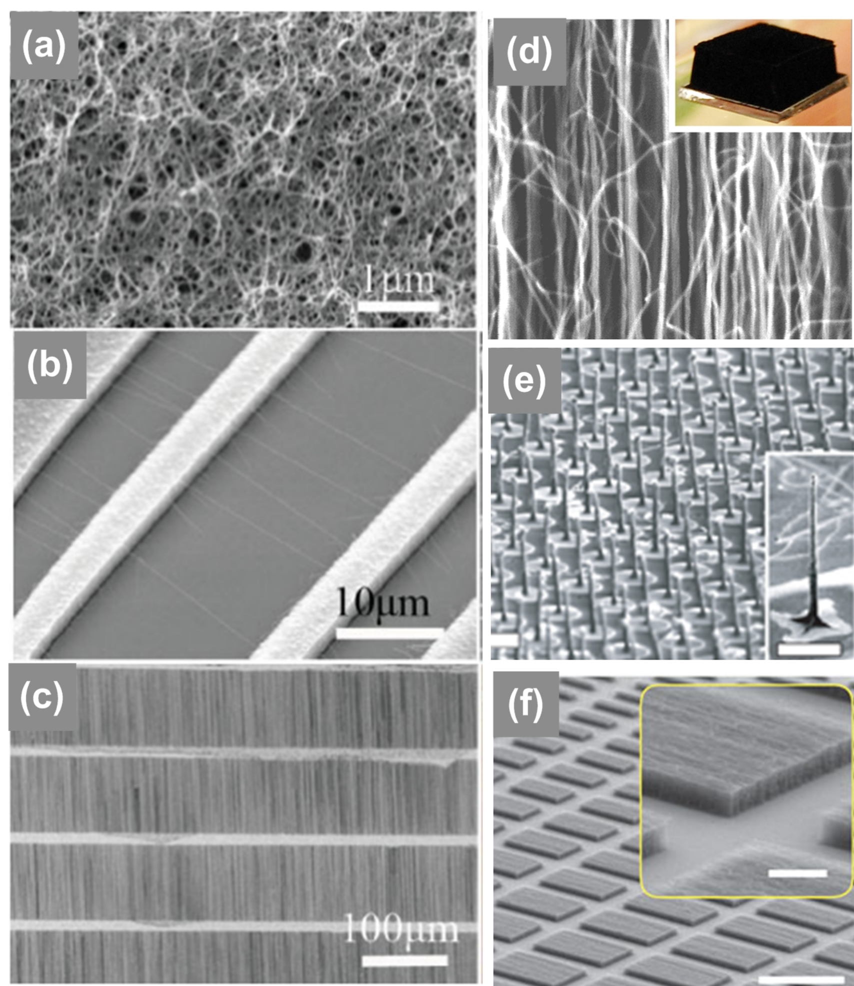

Figure 2.13 SEM images of CNT films grown by CVD. (a) tangled thin SWCNT films made by ethanol assisted growth. (b) Horizontally aligned (HA-) SWCNTs made directly by CVD with an applied electric field between microelectrodes (white). (c) HA-SWCNT made by CVD with methanol and Fe catalyst patterned into 10 mm wide stripes (bright horizontal lines) on quartz.[86] (d) Vertically aligned (VA-) MWCNTs made by CVD with ethylene carbon source. Inset showing several mm growth height.[87] (e) Capillary densified VA-SWCNT pins made by CVD and solvent immersion.[88] (f) HA-SWCNTs made by CVD of line patterns and capillary collapse.[84]

Geometric control:

VA-CNTs are synthesized from catalyst films. The lateral dimensions of the films are prescribed by photolithographic patterning and lift-off. Photolithography is used for features in the μm range. For features smaller than 400 nm deep UV, interference or nanoimprint lithography can be used. VA-CNTs grow perpendicular to the substrate (2.5-D); and hence don't have controlled inclination angles to form 3-D geometries. The

growth rate can be controlled by the synthesis environment (gas mixture, pressure and temperature) but is usually high (0.1-2 μm/s). This makes them useful for micro-scale structures. If very high aspect ratios are desired, VA-CNT growth can proceed until the self-termination stage (~ 1 hour) leading to growth heights typically ~1 mm but can be s high as a few cm.[89, 90] VA-CNT microstructure can be stable for up to 10:1 aspect ratios. Higher aspect ratios need to be structurally stabilized by larger neighboring CNT microstructures as shown in **Figure 2.14**.

CNT diameter:

The diameter, density and alignment of CNTs in this configuration influence the properties of the microstructures. Effective diameter control for VA- multiwalled (MW) CNT can be realized by growing from preformed nanoparticles as the catalyst layer.[91] For single and double walled CNTs, diameter control can be achieved by controlling the catalyst film thickness and the growth environment.[92] For example, control of the amount of water vapor in the growth environment can effectively lead to single walled (SW) CNT with diameters < 3 nm.[93] Chirality[2] control for SWCNT remains one of the most challenging aspects of SWCNT synthesis and is beyond the scope of this discussion.[94, 95]

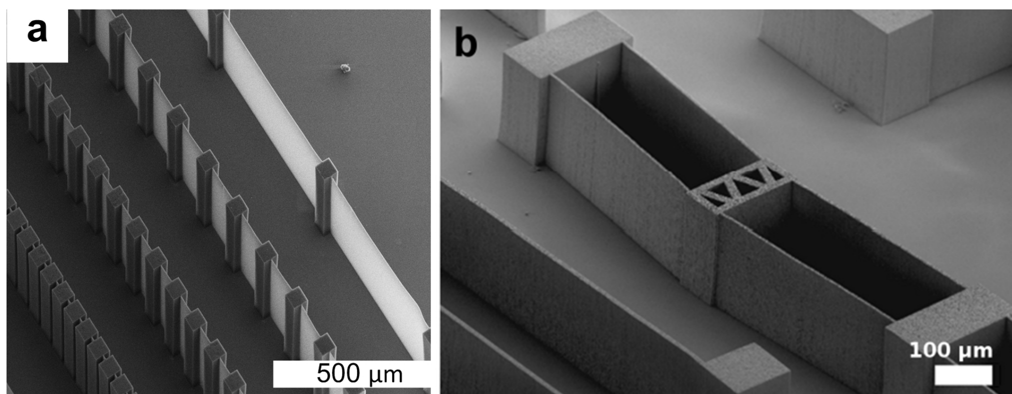

Figure 2.14 High aspect ratio straight VA-CNT growth and integration. (a) Structurally supported structures of straight high aspect ratio low density VA-CNTs. (b) Integration of VA-CNT infiltrated with SiO_2 in MEMS.[96]

[2] Chirality is the angle between the shell orientation and the tube axis; it determines the tube's electrical properties (conductive/semiconductive)

Packing fraction and density:

VA-CNT forests grown from substrate bound catalyst films are characterized by very low density, typically between 1 and 5%.[68] This low density is in fact essential for the growth to proceed because it accounts for the mechanical stresses developed due to the polydispersity in diameter and growth rates among neighboring CNTs. The low density results in (i) low mechanical robustness (stiffness ~ MPa) and (ii) decreased performance per unit area due to the low number of active CNTs. Further, liquid processing lead to the uncontrolled distortion and/or collapse of as-grown VA-CNT microstructures[97] due to elastocapillary coalescence.[97]

Substrate adhesion:

VA-CNTs are typically adhered to the substrate by weak van der Waals forces and hence can be easily delaminated. Controlling the adhesion of the CNT films to the catalyst film can be achieved by modifying the growth environment. For example, a flow of hydrocarbon source at temperatures between 300°C and 600°C can enhance the adhesion of the CNT to the catalyst and hence to the substrate by forming thin carbon layers at the interface between the catalyst particle and the CNT.[98]

Substrate and transferability:

VA-CNTs are typically synthesized on silicon wafers. However, quartz and metal foils coated with the suitable catalyst (e.g. Al_2O_3/Fe) can be used as growth substrate as long as they have an adequate melting temperature (>1000°C) and are chemically stable in the growth environment (hydrocarbon and H_2 at high temperature). Alternatively, VA-CNT microstructures can be transferred using thermal bonding to polymer films as shown in **Figure 2.15**.[99-101] Polymer films are carefully laminated on top of the VA-CNT films. The films are adequately heated until polymer reflow and capillary forces cause partial embedding of the CNTs and hence their adhesion to the polymer. Small pressure is applied to ensure contact without mechanically distorting the CNTs.

Coating and functionalization:

Coating and functionalization of VA-CNTs can be performed by gas phase processes. Solution based processing can damage as-grown VA-CNT due to capillary forces. CNTs

can be conformally coated by PVD of metals and ceramics; CVD of polymers and oxides; or atomic layer deposition (ALD) of ceramics. The coatings can enhance the chemical, electrical, optical and mechanical functionality of the CNTs. Owing to the filamentary and porous structure of VA-CNT, the coating parameters and CNT microstructure geometries need to be optimized to obtain uniform deposition thickness across the microstructures.

Methods of enhancing density

Capillary forces from liquid processing distort CNT forests by randomly aggregating tem into a cellular like structure.[97] On the other hand, recent studies showed that capillary forces can transform cylindrical patterns (50 μm diameter; aspect ratio <2) into robust microstrcutures of densely packed SWCNTs.[88] This simple method, which inspired the work of this dissertation, transforms fragile as-grown CNT microstructures of 3 % density into robust 50% dense CNTs. Alternatively, cm scale CNT forests can be delaminated from the substrate and mechanically compacted then capillary densified to form stiff CNT solids.

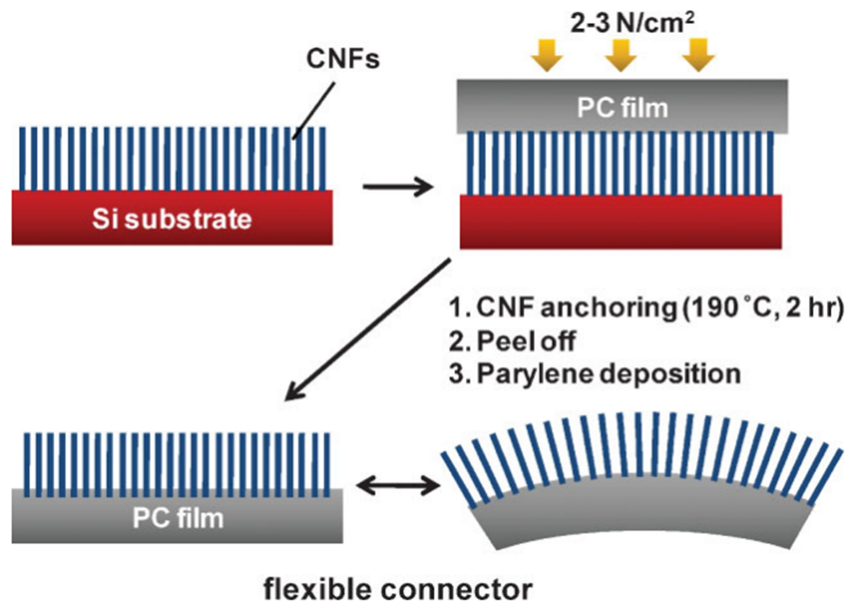

Figure 2.15 Transfer of VA-CNT to flexible substrates. Schematic showing the transfer of carbon nanofibers (CNF) to polycarbonate films.[100]

Methods of making high aspect ratio elements for Micro- Electro- Mechanical Systems

Owing to their high aspect ratio, high electrical conductivity and good temperature stability, VA-CNT microstructures are potential building block elements in MEMS.[96] To overcome their low density and stiffness, VA-CNTs are infiltrated with conformal layers of polycrystalline silicon or silicon nitride. Due to the conformal nature of CVD, high aspect ratio CNT microstructures can be filled at very high rate. For example, 100 µm tall patterns can be filled with poly-Si in about 3 hours. To ensure uniform deposition along the entire height and area, small holes (<3 µm diameter) are designed in the catalyst layer to allow for the deposition gases to diffuse into large microstructures (gas access holes). The resulting CNT-silicon microstructures can be processed using standard microfabrication techniques such as lithography and DRIE. Using this approach, high aspect ratio (100:1) MEMS actuators are fabricated. Robust VA-CNT microstructures can be fabricated using a similar approach using parylene or other polymer deposition.[102]

2.2.3. Examples of properties and applications of VA-CNTs

Interconnect via

As discussed in **Section 2.2.1**, it is predicted that the resistance of 70 nm diameter CMOS interconnect vertical via filled with close packed MWCNT of 4 nm diameter having 6 walls, can be as low as that of a Cu via. Fujitsu,[103-105] Infineon[106] and IMEC[107] reported progress in process technology towards achieving this high performance, including direct growth of the CNTs within vias at CMOS-compatible temperatures followed by deposition of a top electrical contact. **Table 2.4** shows the most recently reported results from these groups.

Despite this encouraging progress, several challenges have to be met before CNTs can actually replace Cu interconnect vias. According to the 2009 International Technology Roadmap of Semiconductors (ITRS, 2009) the main challenges to overcome for vertical vias are:[76]

Table 2.4 Recent advances and benchmarks in CNT interconnect via

Via dia.	CNT dia.	Stackup	Catalyst	Recipe	Density [CNTs/cm^2]	Resistance	Ref.
2 µm	10 nm	Cu/Ta/Ti /Co/CNT / Ti/Cu	2.5 nm Co layer	thermal CVD 450°C	10^{10}	5 Ω	103
140-300 nm	15 nm	Cu/Al/ Ni/CNT/ AuPd	3 nm Ni layer	thermal CVD 520°C	5 x 10^{10}	20 Ω	108
2 µm	10 nm	Cu/Ta/ TiN/Co/ CNT/Ti/ Cu	4 nm Co nano-particles	thermal CVD 510°C	9x10^{11} and 10^{11}	0.59 Ω	91
150-300 nm	8-12 nm	TiN/SiC/ PSG/SiC	1.3 nm Ni Layer	CVD 400-470°C	2x10^{11} – 7x10^{10}	7.9 kΩ	107
120 nm	7 nm	Cu/TaN/ Tin/Co/ CNT	1.7 nm Co film	thermal CVD 450°C	10^{12}	not yet reported	105

1. Improved control over CNT diameter, number of walls and quality
2. Achieving high CNT areal density, e.g., at least 5 x 10^{12} CNTs/cm^2 for MWNTs
3. Achieving ohmic contact to the ends of the CNTs

Recent advances towards the realization of high density growth at low temperatures focus on the decomposition of feedstock gases using a multi-mode (RF plasma, DC plasma, hot-filament, and thermal) CVD chamber to scale up the process to obtain uniform growth on full 300 mm wafers.[105] Uniform diameter catalyst nanoparticles are prepared either by dewetting a thin catalyst layer (Co or Ni) through thermal annealing or by direct injection of catalyst nanoparticles from gas phase. Both of these variations aim at achieving the highest density of active nanoparticles selectively at the bottom of the via holes. More recently, Fujitsu reports a plasma-enhanced formation of small-diameter, closely packed nanoparticles from a deposited layer of Co.[91] The key to their method is to control the nanoparticle size and density and to stop the aggregation of particles before the growth starts. This is achieved using a low temperature (<260 °C) and low-power plasma (<0.5 W/cm^2) for annealing. The CNT density reaches 10^{12} CNTs/cm^2 representing a bulk volumetric density of 30-40%.

Capacitors and battery electrodes

The use of capillary densified CNTs in two-electrode Electric Double Layer Capacitor (EDLC) shows an increase in energy density and ion diffusivity compared to activated porous carbon[28] possibly due to the pore alignment.[88, 109] Alternatively, VA-CNT can be synthesized in aligned porous Anodic Aluminum Oxide (AAO) membranes. Using these templates, coaxial CNT/MnO_2 can be fabricated and use as Li ion battery cathodes.[88, 110] The CNTs in this configuration enhance the performance of the batteries due to high surface area, improved electrical conductivity and improved ion storage and cycling kinetics.

2.2.4. Integration considerations of HA-CNTs

HA-CNT configuration provides directional in-plane properties for the engineering of anisotropic devices and surfaces. Moreover, owing to their planar structure and robust architecture, HA-CNT can be more readily integrated with standard microfabrication processes. Two routes are currently taken for the fabrication of HA-CNT films: (i) direct synthesis in the horizontal configuration;[61] and (ii) mechanical and/or capillary transformation of VA-CNT to HA-CNTs.[69, 84, 98] Most important considerations for the synthesis and integration of HA-CNT using the two routes are summarized in this section. Routes (i) result in a single layer of low density aligned CNT, where the CNTs are straight and isolated; routes (ii) result in high packing density films having controlled geometry as discussed in the following sections.

Direct synthesis of HA-CNT:

HA-CNT can be directly synthesized high temperature(>900°C) on special cut single crystal substrates such as c-cut quartz and sapphire.[61] Crystal topography offers a template for the unidirectional aligned growth of SWCNTs as described in **Section 2.1.6**. However, the extreme growth conditions hinder the applicability of direct synthesis to for example CMOS compatible processes. This process is also limited to creating a single layer of largely spaced CNTs (<100 CNTs/μm). Controlling the number of layers or achieving packed assemblies using direct horizontal synthesis hasn't to date been achieved.

HA-CNT by rolling:

Mechanical rolling enables the transformation of as-grown, low-density, VA-CNT line patterns into high density HA-CNT films.[69, 98, 111] Considerations for applying this process are the same as those for VA-CNT processing (**Section 2.2.1**). Additional considerations include minimizing rolling induced defects and contamination, and controlling the adhesion of the CNTs to the receiving substrate. This process is discussed in details in **Chapter 4**.

HA-CNT by capillary forming:

The capillary forces resulting from dipping VA-CNT walls in and out of a liquid surface such as acetone can be used to fabricate thin films of HA-CNT on large areas.[84] The final thickness of the HA-CNT film is controlled by the width of the catalyst line pattern used to grow the VA-CNTs. The considerations for applying this process are the same as those for VA-CNT processing.

Orientation of HA-CNT:

Current methods to fabricate HA-CNT are limited to creating unidirectional films on substrates. Locally multi-directional and multi-layered architectures, which are needed for design of next-generation circuits and interconnects, have only been achieved by multi-step alignment and transfer printing methods[64, 112] or by self-directed capillary folding described in **Chapter 5** of the thesis.[70]

Transfer of HA-CNT films:

Dry transfer printing of HA-CNT films can be easily achieved using PDMS stamps onto arbitrary substrates as shown in **Figure 2.16**.[113] Owing to their viscoelastic properties, dry PDMS stamps can be used to pick HA-CNT films from growth substrates by quick peeling and transfer to target substrate by slow peeling.[114] Thin films of HA-SWCNTs synthesized on quartz substrates can only be transferred if coated with carrier films such as thin Au to facilitate their separation from the growth substrate and later from the stamp.

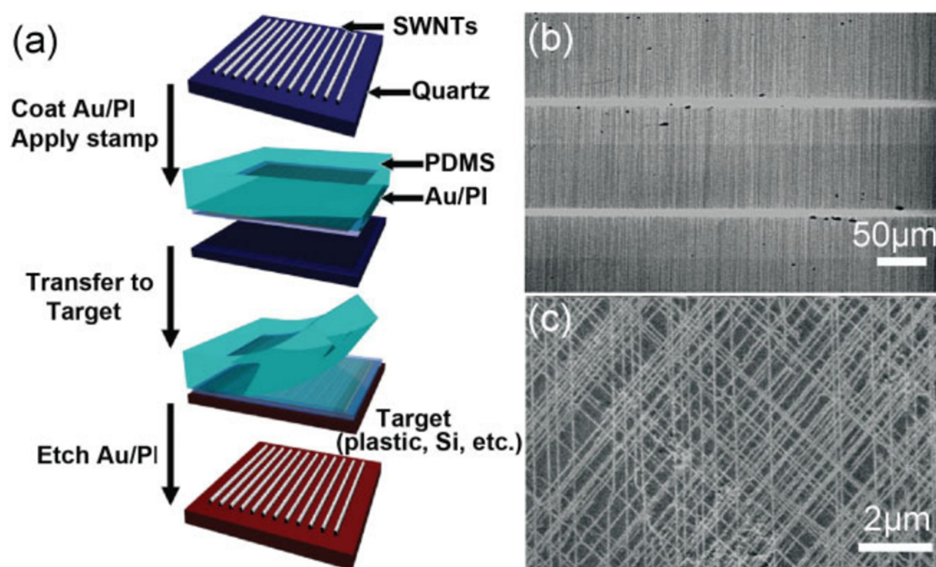

Figure 2.16 Transfer printing of HA-CNTs using PDMS stamps. (a) Schematic of transfer printing process using Au carrier films. (b) and (c) printed films of HA-SWCNT having uni- and multi-directional configurations.[114]

2.2.5. Examples of properties and applications of HA-CNTs

HA-CNT for flexible electronics

Transferring ultra-thin films of HA-CNTs to PDMS enables the formation of flexible transistors on flexible conformal and stretchable electronic systems.[86] Devices formed by simple transfer printing of HA-CNT films can withstand up to 20% strain. An alternative design can be adopted with SWNTs arranged in the ‘‘wavy’’ layout, which is formed through film buckling process. These devices can take large stains reaching up to 50%.

MEMS Switches and resonators

Forming dense arrays of HA-CNT using the capillary dipping method enables the fabrication of micro- electro- mechanical switches from thin CNT films by standard lithography, etching and lift-off as shown in **Figure 2.17**. Electrical nanorelays of ~ 100 nm dimensions were fabricated and cycled > 20 times to pass currents beyond 100 μW for up to 2 s.[84] The performance of these devices is limited by the cantilever drain-sticking force. Notably, the elastic modulus of the CNT films can be estimated form the performance of these devices to be 9.7 GPa. HA-CNT resonators can be fabricated using the same approach for making CNT relays. The resonators having the CNT parallel to

the longitudinal direction behave as cohesive elastic beams with sound velocity of 10100 m/s.[115]

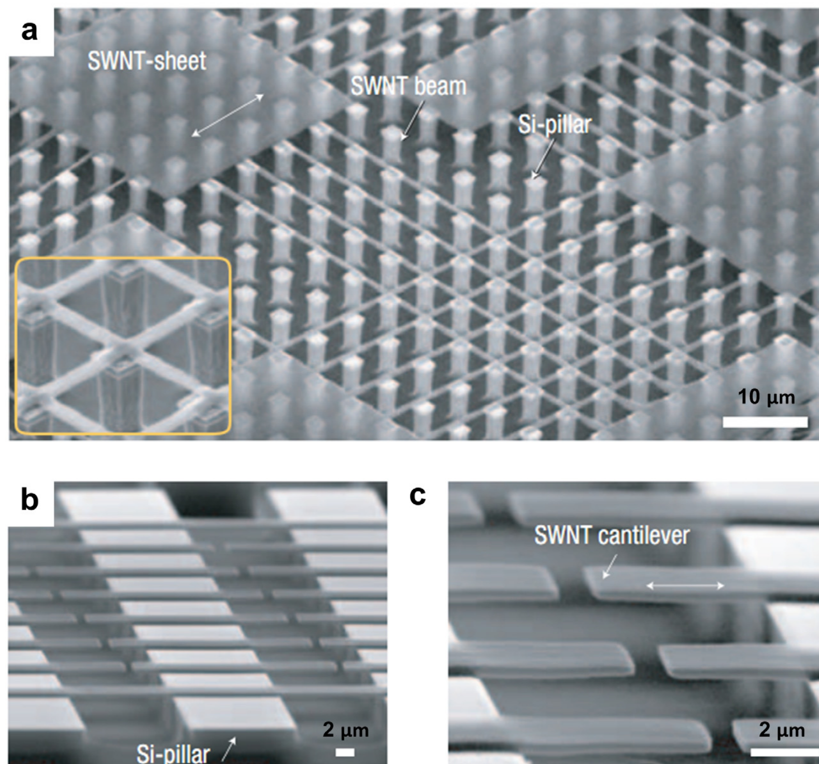

Figure 2.17 Integrated HA-CNT MEMS resonators and switches. (a) Low resolution SEM showing a large area of HA-CNT suspended on Si pillars. (b,c) High resolution SEM images showing the HA-CNT cantilevers. [116]

2. 3 Bibliography

1. Chu, K.-H.; Xiao, R.; Wang, E. N., Uni-directional liquid spreading on asymmetric nanostructured surfaces. *Nat Mater* **2010,** *9* (5), 413-417.

2. Fang, H.; et al., Fabrication of slantingly-aligned silicon nanowire arrays for solar cell applications. *Nanotechnology* **2008,** *19* (25), 255703.

3. Hawkeye, M. M.; Brett, M. J., Glancing angle deposition: Fabrication, properties, and applications of micro- and nanostructured thin films. *Journal of Vacuum Science & Technology A: Vacuum, Surfaces, and Films* **2007,** *25* (5), 1317-1335.

4. Gansel, J. K.; Thiel, M.; Rill, M. S.; Decker, M.; Bade, K.; Saile, V.; von Freymann, G.; Linden, S.; Wegener, M., Gold Helix Photonic Metamaterial as Broadband Circular Polarizer. *Science* **2009,** *325* (5947), 1513-1515.

5. Pokroy, B.; Kang, S. H.; Mahadevan, L.; Aizenberg, J., Self-Organization of a Mesoscale Bristle into Ordered, Hierarchical Helical Assemblies. *Science* **2009,** *323* (5911), 237-240.

6. Bates, F. S.; Fredrickson, G. H., Block Copolymer Thermodynamics: Theory and Experiment. *Annual Review of Physical Chemistry* **1990,** *41* (1), 525-557.

7. Bates, F. S.; Fredrickson, G. H., Block Copolymers—Designer Soft Materials. *Physics Today* **1999,** *52*, 32.

8. Bowden, N.; Brittain, S.; Evans, A. G.; Hutchinson, J. W.; Whitesides, G. M., Spontaneous formation of ordered structures in thin films of metals supported on an elastomeric polymer. *Nature* **1998,** *393* (6681), 146-149.

9. Campo, A. d.; Greiner, C., SU-8: a photoresist for high-aspect-ratio and 3D submicron lithography. *Journal of Micromechanics and Microengineering* **2007,** *17* (6), R81.

10. Beuret, C.; Racine, G. A.; Gobet, J.; Luthier, R.; de Rooij, N. F. In *Microfabrication of 3D multidirectional inclined structures by UV lithography and electroplating*, Proceedings of the IEEE Workshop on Micro Electro Mechanical Systems, 1994; 1994; pp 81-85.

11. Tabata, O.; Terasoma, K.; Agawa, N.; Yamamoto, K. In *Moving mask LIGA (M²LIGA) process for control of side wall inclination*, Micro Electro Mechanical Systems, 1999. MEMS '99. Twelfth IEEE International Conference on, 17-21 Jan 1999; 1999; pp 252-256.

12. Sato, H.; Yagyu, D.; Ito, S.; Shoji, S., Improved inclined multi-lithography using water as exposure medium and its 3D mixing microchannel application. *Sensors and Actuators A: Physical* **2006,** *128* (1), 183-190.

13. Hung, K.-Y.; et al., Application of 3D glycerol-compensated inclined-exposure technology to an integrated optical pick-up head. *Journal of Micromechanics and Microengineering* **2004,** *14* (7), 975.

14. Mekaru, H.; Utsumi, Y.; Hattori, T., Quasi-3D microstructure fabrication technique utilizing hard X-ray lithography of synchrotron radiation. *Microsystem Technologies* **2002,** *9* (1), 36-40.

15. Han, M.; Lee, W.; Lee, S.-K.; Lee, S. S., 3D microfabrication with inclined/rotated UV lithography. *Sensors and Actuators A: Physical* **2004,** *111* (1), 14-20.

16. Yoon, Y.-K.; et al., A thermal microjet system with tapered micronozzles fabricated by inclined UV lithography for transdermal drug delivery. *Journal of Micromechanics and Microengineering* **2011,** *21* (2), 025014.

17. Sato, H.; Kakinuma, T.; Go, J. S.; Shoji, S., In-channel 3-D micromesh structures using maskless multi-angle exposures and their microfilter application. *Sensors and Actuators A: Physical* **2004,** *111* (1), 87-92.

18. Sato, H.; et al., An all SU-8 microfluidic chip with built-in 3D fine microstructures. *Journal of Micromechanics and Microengineering* **2006,** *16* (11), 2318.

19. Yang, R.; Feeback, D. L.; Wang, W., Microfabrication and test of a three-dimensional polymer hydro-focusing unit for flow cytometry applications. *Sensors and Actuators A: Physical* **2005,** *118* (2), 259-267.

20. Peng, K. Q.; Yan, Y. J.; Gao, S. P.; Zhu, J., Dendrite-assisted growth of silicon nanowires in electroless metal deposition. *Advanced Functional Materials* **2003,** *13* (2), 127-132.

21. Huang, Z.; Geyer, N.; Werner, P.; de Boor, J.; Gösele, U., Metal-Assisted Chemical Etching of Silicon: A Review. *Advanced Materials* **2010,** *23* (2), 285-308.

22. Peng, K. Q.; Zhang, M. L.; Lu, A. J.; Wong, N. B.; Zhang, R. Q.; Lee, S. T., Ordered silicon nanowire arrays via nanosphere lithography and metal-induced etching. *Applied Physics Letters* **2007,** *90* (16).

23. Chang, S.-W.; Chuang, V. P.; Boles, S. T.; Ross, C. A.; Thompson, C. V., Densely Packed Arrays of Ultra-High-Aspect-Ratio Silicon Nanowires Fabricated using Block-Copolymer Lithography and Metal-Assisted Etching. *Advanced Functional Materials* **2009,** *19* (15), 2495-2500.

24. Huang, Z.; Zhang, X.; Reiche, M.; Liu, L.; Lee, W.; Shimizu, T.; Senz, S.; Goۦˆsele, U., Extended Arrays of Vertically Aligned Sub-10 nm Diameter [100] Si Nanowires by Metal-Assisted Chemical Etching. *Nano Letters* **2008,** *8* (9), 3046-3051.

25. Hildreth, O. J.; Lin, W.; Wong, C. P., Effect of Catalyst Shape and Etchant Composition on Etching Direction in Metal-Assisted Chemical Etching of Silicon to Fabricate 3D Nanostructures. *Acs Nano* **2009,** *3* (12), 4033-4042.

26. Kim, J.; Han, H.; Kim, Y. H.; Choi, S.-H.; Kim, J.-C.; Lee, W., Au/Ag Bilayered Metal Mesh as a Si Etching Catalyst for Controlled Fabrication of Si Nanowires. *Acs Nano* **2011,** *5* (4), 3222-3229.

27. Huang, Z. P.; Shimizu, T.; Senz, S.; Zhang, Z.; Zhang, X. X.; Lee, W.; Geyer, N.; Gosele, U., Ordered Arrays of Vertically Aligned [110] Silicon Nanowires by Suppressing the Crystallographically Preferred Etching Directions. *Nano Letters* **2009,** *9* (7), 2519-2525.

28. An, K. H.; Kim, W. S.; Park, Y. S.; Moon, J. M.; Bae, D. J.; Lim, S. C.; Lee, Y. S.; Lee, Y. H., Electrochemical Properties of High-Power Supercapacitors Using Single-Walled Carbon Nanotube Electrodes. *Advanced Functional Materials* **2001,** *11* (5), 387-392.

29. Rykaczewski, K.; Hildreth, O. J.; Wong, C. P.; Fedorov, A. G.; Scott, J. H. J., Guided Three-Dimensional Catalyst Folding during Metal-Assisted Chemical Etching of Silicon. *Nano Letters* **2011,** *11* (6), 2369-2374.

30. Hildreth, O. J.; Brown, D.; Wong, C. P., 3D Out-of-Plane Rotational Etching with Pinned Catalysts in Metal-Assisted Chemical Etching of Silicon. *Advanced Functional Materials* **2011,** *21* (16), 3119-3128.

31. Robbie, K.; Brett, M. J.; Lakhtakia, A., Chiral sculptured thin films. *Nature* **1996,** *384* (6610), 616-616.

32. Reichelt, K., Nucleation and growth of thin films. *Vacuum* **1988,** *38* (12), 1083-1099.

33. Tait, R. N.; Smy, T.; Brett, M. J., Modelling and characterization of columnar growth in evaporated films. *Thin Solid Films* **1993,** *226* (2), 196-201.

34. Ye, D.-X.; et al., Uniform Si nanostructures grown by oblique angle deposition with substrate swing rotation. *Nanotechnology* **2005,** *16* (9), 1717.

35. He, Y.; Zhao, Y., Advanced multi-component nanostructures designed by dynamic shadowing growth. *Nanoscale* **2011,** *3* (6), 2361-2375.

36. Pursel, S.; Horn, M. W.; Demirel, M. C.; Lakhtakia, A., Growth of sculptured polymer submicronwire assemblies by vapor deposition. *Polymer* **2005,** *46* (23), 9544-9548.

37. Malvadkar, N. A.; Hancock, M. J.; Sekeroglu, K.; Dressick, W. J.; Demirel, M. C., An engineered anisotropic nanofilm with unidirectional wetting properties. *Nat Mater* **2010,** *9* (12), 1023-1028.

38. Boduroglu, S.; Cetinkaya, M.; Dressick, W. J.; Singh, A.; Demirel, M. C., Controlling the Wettability and adhesion of nanostructured poly-(p-xylylene) films. *Langmuir* **2007,** *23* (23), 11391-11395.

39. Demirel, M. C.; Kao, P.; Malvadkar, N.; Wang, H.; Gong, X.; Poss, M.; Allara, D. L., Bio-organism sensing via surface enhanced Raman spectroscopy on controlled metal/polymer nanostructured substrates. *Biointerphases* **2009,** *4* (2), 35-41.

40. Cetinkaya, M.; Demirel, M. C., Bridging Experiments and Simulations in Oblique Angle Polymerization. *Chemical Vapor Deposition* **2009,** *15* (4-6), 101-105.

41. Demirel, M. C.; Boduroglu, S.; Cetinkaya, M.; Lakhtakia, A., Spatially Organized Free-Standing Poly(p-xylylene) Nanowires Fabricated by Vapor Deposition. *Langmuir* **2007,** *23* (11), 5861-5863.

42. Cetinkaya, M.; Boduroglu, S.; Demirel, M. C., Growth of nanostructured thin films of poly(p-xylylene) derivatives by vapor deposition. *Polymer* **2007,** *48* (14), 4130-4134.

43. Kim, T.-I.; Suh, K. Y., Unidirectional wetting and spreading on stooped polymer nanohairs. *Soft Matter* **2009,** *5* (21), 4131-4135.

44. Kim, T. I.; Jeong, H. E.; Suh, K. Y.; Lee, H. H., Stooped Nanohairs: Geometry-Controllable, Unidirectional, Reversible, and Robust Gecko-like Dry Adhesive. *Advanced Materials* **2009,** *21* (22), 2276-+.

45. Kim, P.; Epstein, A. K.; Khan, M.; Zarzar, L. D.; Lipomi, D. J.; Whitesides, G. M.; Aizenberg, J., Structural Transformation by Electrodeposition on Patterned Substrates (STEPS): A New Versatile Nanofabrication Method. *Nano Letters* **2011,** *in press, doi: 10.1021/nl200426g*.

46. Kwak, M. K.; Jeong, H.-E.; Kim, T.-i.; Yoon, H.; Suh, K. Y., Bio-inspired slanted polymer nanohairs for anisotropic wetting and directional dry adhesion. *Soft Matter* **2010,** *6* (9), 1849-1857.

47. Kim, T.-i.; Pang, C.; Suh, K. Y., Shape-Tunable Polymer Nanofibrillar Structures by Oblique Electron Beam Irradiation. *Langmuir* **2009,** *25* (16), 8879-8882.

48. Seminara, A.; Pokroy, B.; Kang, S. H.; Brenner, M. P.; Aizenberg, J., Mechanism of nanostructure movement under an electron beam and its application in patterning. *Physical Review B* **2011,** *83* (23).

49. Yoon, H.; Jeong, H. E.; Kim, T.-i.; Kang, T. J.; Tahk, D.; Char, K.; Suh, K. Y., Adhesion hysteresis of Janus nanopillars fabricated by nanomolding and oblique metal deposition. *Nano Today* **2009,** *4* (5), 385-392.

50. Sidorenko, A.; Krupenkin, T.; Taylor, A.; Fratzl, P.; Aizenberg, J., Reversible Switching of Hydrogel-Actuated Nanostructures into Complex Micropatterns. *Science* **2007,** *315* (5811), 487-490.

51. Kim, P.; Zarzar, L. D.; He, X.; Grinthal, A.; Aizenberg, J., Hydrogel-actuated integrated responsive systems (HAIRS): Moving towards adaptive materials. *Current Opinion in Solid State and Materials Science* **2011,** *In Press, Corrected Proof*.

52. Burgess, I. B.; Mishchenko, L.; Hatton, B. D.; Kolle, M.; LoncجŒar, M.; Aizenberg, J., Encoding Complex Wettability Patterns in Chemically Functionalized 3D Photonic Crystals. *Journal of the American Chemical Society* **2011,** *133* (32), 12430-12432.

53. Tian, B.; Xie, P.; Kempa, T. J.; Bell, D. C.; Lieber, C. M., Single-crystalline kinked semiconductor nanowire superstructures. *Nat Nano* **2009,** *4* (12), 824-829.

54. Bierman, M. J.; Lau, Y. K. A.; Kvit, A. V.; Schmitt, A. L.; Jin, S., Dislocation-Driven Nanowire Growth and Eshelby Twist. *Science* **2008,** *320* (5879), 1060-1063.

55. Zhu, J.; Peng, H.; Marshall, A. F.; Barnett, D. M.; Nix, W. D.; Cui, Y., Formation of chiral branched nanowires by the Eshelby Twist. *Nat Nano* **2008,** *3* (8), 477-481.

56. Eshelby, J. D., *Screw Dislocations in Thin Rods*. AIP: 1953; Vol. 24.

57. Zhang, H.-F.; Wang, C.-M.; Buck, E. C.; Wang, L.-S., Synthesis, Characterization, and Manipulation of Helical SiO2 Nanosprings. *Nano Letters* **2003,** *3* (5), 577-580.

58. McIlroy, D. N.; Zhang, D.; Kranov, Y.; Norton, M. G., Nanosprings. *Applied Physics Letters* **2001,** *79* (10), 1540-1542.

59. Wang, L.; et al., High yield synthesis and lithography of silica-based nanospring mats. *Nanotechnology* **2006,** *17* (11), S298.

60. Zhang, D.; Alkhateeb, A.; Han, H.; Mahmood, H.; McIlroy, D. N.; Norton, M. G., Silicon Carbide Nanosprings. *Nano Letters* **2003,** *3* (7), 983-987.

61. Xiao, J.; Dunham, S.; Liu, P.; Zhang, Y.; Kocabas, C.; Moh, L.; Huang, Y.; Hwang, K.-C.; Lu, C.; Huang, W.; Rogers, J. A., Alignment Controlled Growth of Single-Walled Carbon Nanotubes on Quartz Substrates. *Nano Letters* **2009,** *9* (12), 4311-4319.

62. Ding, L.; Yuan, D.; Liu, J., Growth of High-Density Parallel Arrays of Long Single-Walled Carbon Nanotubes on Quartz Substrates. *Journal of the American Chemical Society* **2008,** *130* (16), 5428-5429.

63. Zhou, W.; Ding, L.; Yang, S.; Liu, J., Synthesis of High-Density, Large-Diameter, and Aligned Single-Walled Carbon Nanotubes by Multiple-Cycle Growth Methods. *Acs Nano* **2011,** *5* (5), 3849-3857.

64. Kang, S. J.; Kocabas, C.; Kim, H.-S.; Cao, Q.; Meitl, M. A.; Khang, D.-Y.; Rogers, J. A., Printed Multilayer Superstructures of Aligned Single-Walled Carbon Nanotubes for Electronic Applications. *Nano Letters* **2007,** *7* (11), 3343-3348.

65. Cubukcu, E.; Degirmenci, F.; Kocabas, C.; Zimmler, M. A.; Rogers, J. A.; Capasso, F., Aligned carbon nanotubes as polarization-sensitive, molecular near-field detectors. *Proceedings of the National Academy of Sciences* **2009,** *106* (8), 2495-2499.

66. Kang, S. J.; Kocabas, C.; Ozel, T.; Shim, M.; Pimparkar, N.; Alam, M. A.; Rotkin, S. V.; Rogers, J. A., High-performance electronics using dense, perfectly aligned arrays of single-walled carbon nanotubes. *Nature Nanotechnology* **2007,** *2* (4), 230-236.

67. Bajpai, V.; Dai, L.; Ohashi, T., Large-Scale Synthesis of Perpendicularly Aligned Helical Carbon Nanotubes. *Journal of the American Chemical Society* **2004,** *126* (16), 5070-5071.

68. Hart, A. J.; Slocum, A. H., Rapid growth and flow-mediated nucleation of millimeter-scale aligned carbon nanotube structures from a thin-film catalyst. *Journal of Physical Chemistry B* **2006,** *110* (16), 8250-8257.

69. Tawfick, S.; O'Brien, K.; Hart, A. J., Flexible High-Conductivity Carbon-Nanotube Interconnects Made by Rolling and Printing. *Small* **2009,** *5* (21), 2467-2473.

70. Tawfick, S.; De Volder, M.; Hart, A. J., Structurally Programmed Capillary Folding of Carbon Nanotube Assemblies. *Langmuir* **2011,** *27* (10), 6389-6394.

71. AuBuchon, J. F.; Chen, L.-H.; Gapin, A. I.; Kim, D.-W.; Daraio, C.; Jin, S., Multiple Sharp Bendings of Carbon Nanotubes during Growth to Produce Zigzag Morphology. *Nano Letters* **2004,** *4* (9), 1781-1784.

72. Wang, W.; Yang, K. Q.; Gaillard, J.; Bandaru, P. R.; Rao, A. M., Rational synthesis of helically coiled carbon nanowires and nanotubes through the use of tin and indium catalysts. *Advanced Materials* **2008,** *20* (1), 179-+.

73. Amelinckx, S.; Zhang, X. B.; Bernaerts, D.; Zhang, X. F.; Ivanov, V.; Nagy, J. B., A Formation Mechanism for Catalytically Grown Helix-Shaped Graphite Nanotubes. *Science* **1994,** *265* (5172), 635-639.

74. Tang, N.; Wen, J.; Zhang, Y.; Liu, F.; Lin, K.; Du, Y., Helical Carbon Nanotubes: Catalytic Particle Size-Dependent Growth and Magnetic Properties. *Acs Nano* **2010,** *4* (1), 241-250.

75. Fan, S.; Chapline, M. G.; Franklin, N. R.; Tombler, T. W.; Cassell, A. M.; Dai, H., Self-Oriented Regular Arrays of Carbon Nanotubes and Their Field Emission Properties. *Science* **1999,** *283* (5401), 512-514.

76. International Technology Roadmap for Semiconductors. http://www.itrs.net/Links/2009ITRS/Home2009.htm **2009**, accessed in September 2011.

77. Wei, B. Q.; Vajtai, R.; Ajayan, P. M., *Reliability and current carrying capacity of carbon nanotubes*. AIP: 2001; Vol. 79, p 1172-1174.

78. Fischer, J. E.; Zhou, W.; Vavro, J.; Llaguno, M. C.; Guthy, C.; Haggenmueller, R.; Casavant, M. J.; Walters, D. E.; Smalley, R. E., Magnetically aligned single wall carbon nanotube films: Preferred orientation and anisotropic transport properties. *Journal of Applied Physics* **2003,** *93* (4), 2157-2163.

79. Li, H. J.; Lu, W. G.; Li, J. J.; Bai, X. D.; Gu, C. Z., Multichannel Ballistic Transport in Multiwall Carbon Nanotubes. *Physical Review Letters* **2005,** *95* (8), 086601.

80. Atkinson, K. R.; Hawkins, S. C.; Huynh, C.; Skourtis, C.; Dai, J.; Zhang, M.; Fang, S.; Zakhidov, A. A.; Lee, S. B.; Aliev, A. E.; Williams, C. D.; Baughman, R. H., Multifunctional carbon nanotube yarns and transparent sheets: Fabrication, properties, and applications. *Physica B: Condensed Matter* **2007,** *394* (2), 339-343.

81. Yokoyama, D.; Iwasaki, T.; Ishimaru, K.; Sato, S.; Hyakushima, T.; Nihei, M.; Awano, Y.; Kawarada, H., Electrical properties of carbon nanotubes grown at a low temperature for use as interconnects. *JAPANESE JOURNAL OF APPLIED PHYSICS* **2008,** *47* (4), 1985-1990.

82. Close, G. F.; Wong, H. S. P.; Ieee, *Fabrication and characterization of carbon nanotube interconnects*. 2007; p 203-206.

83. Wang, D.; Song, P. C.; Liu, C. H.; Wu, W.; Fan, S. S., Highly oriented carbon nanotube papers made of aligned carbon nanotubes. *Nanotechnology* **2008,** *19* (7), 6.

84. Hayamizu, Y.; Yamada, T.; Mizuno, K.; Davis, R. C.; Futaba, D. N.; Yumura, M.; Hata, K., Integrated three-dimensional microelectromechanical devices from processable carbon nanotube wafers. *Nature nanotechnology* **2008,** *3*, 289-94.

85. Katagiri, M.; Yamazaki, Y.; Sakuma, N.; Suzuki, M.; Sakai, T.; Wada, M.; Nakamura, N.; Matsunaga, N.; Sato, S.; Nihei, M.; Awano, Y., Fabrication of 70-nm-diameter Carbon Nanotube Via Interconnects by Remote Plasma-Enhanced Chemical Vapor Deposition and Their Electrical Properties. *Proceedings of the 2009 Ieee International Interconnect Technology Conference* **2009**, 44-46.

86. Cao, Q.; Rogers, J. A., Ultrathin Films of Single-Walled Carbon Nanotubes for Electronics and Sensors: A Review of Fundamental and Applied Aspects. *Advanced Materials* **2009,** *21* (1), 29-53.

87. Meshot, E. R.; Bedewy, M.; Lyons, K. M.; Woll, A. R.; Juggernauth, K. A.; Tawfick, S.; Hart, A. J., Measuring the lengthening kinetics of aligned nanostructures by spatiotemporal correlation of height and orientation. *Nanoscale* **2010**.

88. Futaba, D. N.; Hata, K.; Yamada, T.; Hiraoka, T.; Hayamizu, Y.; Kakudate, Y.; Tanaike, O.; Hatori, H.; Yumura, M.; Iijima, S., Shape-engineerable and highly densely packed single-walled carbon nanotubes and their application as super-capacitor electrodes. *Nat Mater* **2006,** *5* (12), 987-994.

89. Zhang, Y.; Gregoire, J. M.; van Dover, R. B.; Hart, A. J., Ethanol-Promoted High-Yield Growth of Few-Walled Carbon Nanotubes. *The Journal of Physical Chemistry C* **2010,** *114* (14), 6389-6395.

90. Jakubinek, M. B.; White, M. A.; Li, G.; Jayasinghe, C.; Cho, W.; Schulz, M. J.; Shanov, V., Thermal and electrical conductivity of tall, vertically aligned carbon nanotube arrays. *Carbon* **2010,** *48* (13), 3947-3952.

91. Sato, S.; Nihei, M.; Mimura, A.; Kawabata, A.; Kondo, D.; Shioya, H.; Taisuke, W.; Mishima, M.; Ohfuti, M.; Awano, Y., Novel approach to fabricating carbon nanotube via interconnects using size-controlled catalyst nanoparticles. *Proceedings of the IEEE 2006 International Interconnect Technology Conference* **2006**, 230-232.

92. Zhang, G.; Mann, D.; Zhang, L.; Javey, A.; Li, Y.; Yenilmez, E.; Wang, Q.; McVittie, J. P.; Nishi, Y.; Gibbons, J.; Dai, H., Ultra-high-yield growth of vertical single-walled carbon nanotubes: Hidden roles of hydrogen and oxygen. *Proceedings of the National Academy of Sciences of the United States of America* **2005,** *102* (45), 16141-16145.

93. Yamada, T.; Namai, T.; Hata, K.; Futaba, D. N.; Mizuno, K.; Fan, J.; Yudasaka, M.; Yumura, M.; Iijima, S., Size-selective growth of double-walled carbon nanotube forests from engineered iron catalysts. *Nat Nano* **2006,** *1* (2), 131-136.

94. Harutyunyan, A. R.; Chen, G.; Paronyan, T. M.; Pigos, E. M.; Kuznetsov, O. A.; Hewaparakrama, K.; Kim, S. M.; Zakharov, D.; Stach, E. A.; Sumanasekera, G. U., Preferential Growth of Single-Walled Carbon Nanotubes with Metallic Conductivity. *Science* **2009,** *326* (5949), 116-120.

95. Chiang, W.-H.; Mohan Sankaran, R., Linking catalyst composition to chirality distributions of as-grown single-walled carbon nanotubes by tuning NixFe1-x nanoparticles. *Nat Mater* **2009,** *8* (11), 882-886.

96. Hutchison, D. N.; Morrill, N. B.; Aten, Q.; Turner, B. W.; Jensen, B. D.; Howell, L. L.; Vanfleet, R. R.; Davis, R. C., Carbon Nanotubes as a Framework for High-Aspect-Ratio MEMS Fabrication. *Microelectromechanical Systems, Journal of* **2010,** *19* (1), 75-82.

97. Chakrapani, N.; Wei, B. Q.; Carrillo, A.; Ajayan, P. M.; Kane, R. S., Capillarity-driven assembly of two-dimensional cellular carbon nanotube foams. *Proceedings of the*

National Academy of Sciences of the United States of America **2004,** *101* (12), 4009-4012.

98. Pint, C. L.; Xu, Y.-Q.; Pasquali, M.; Hauge, R. H., Formation of Highly Dense Aligned Ribbons and Transparent Films of Single-Walled Carbon Nanotubes Directly from Carpets. *Acs Nano* **2008,** *2* (9), 1871-1878.

99. Sunden, E.; Moon, J. K.; Wong, C. P.; King, W. P.; Graham, S., Microwave assisted patterning of vertically aligned carbon nanotubes onto polymer substrates. *Journal of Vacuum Science & Technology B: Microelectronics and Nanometer Structures* **2006,** *24* (4), 1947-1950.

100. Ko, H.; Zhang, Z.; Ho, J. C.; Takei, K.; Kapadia, R.; Chueh, Y.-L.; Cao, W.; Cruden, B. A.; Javey, A., Flexible Carbon-Nanofiber Connectors with Anisotropic Adhesion Properties. *Small* **2010,** *6* (1), 22-26.

101. Tsai, T. Y.; Lee, C. Y.; Tai, N. H.; Tuan, W. H., Transfer of patterned vertically aligned carbon nanotubes onto plastic substrates for flexible electronics and field emission devices. *Applied Physics Letters* **2009,** *95* (1), 013107.

102. Fang, W.; Chu, H. Y.; Hsu, W. K.; Cheng, T. W.; Tai, N. H., Polymer-Reinforced, Aligned Multiwalled Carbon Nanotube Composites for Microelectromechanical Systems Applications. *Advanced Materials* **2005,** *17* (24), 2987-2992.

103. Nihei, M.; Kawabata, A.; Kondo, D.; Horibe, M.; Sato, S.; Awano, Y., Electrical Properties of Carbon Nanotube Bundles for Future Via Interconnects. *JAPANESE JOURNAL OF APPLIED PHYSICS* **2005,** *44* (4A), 1626-1628.

104. Awano, Y.; Sato, S.; Kondo, D.; Ohfuti, M.; Kawabata, A.; Nihei, M.; Yokoyama, N., Carbon nanotube via interconnect technologies: size-classified catalyst nanoparticles and low-resistance ohmic contact formation. *Physica Status Solidi a-Applications and Materials Science* **2006,** *203* (14), 3611-3616.

105. Yamazaki, Y.; Katagiri, M.; Sakuma, N.; Suzuki, M.; Sato, S.; Nihei, M.; Wada, M.; Matsunaga, N.; Sakai, T.; Awano, Y., Synthesis of a Closely Packed Carbon Nanotube Forest by a Multi-Step Growth Method Using Plasma-Based Chemical Vapor Deposition. *Applied Physics Express* **2010,** *3* (5).

106. Kreupl, F.; Graham, A. P.; Duesberg, G. S.; Steinhogl, W.; Liebau, M.; Unger, E.; Honlein, W., Carbon nanotubes in interconnect applications. *Microelectron. Eng.* **2002,** *64* (1-4), 399-408.

107. Chiodarelli, N.; Li, Y.; Cott, D. J.; Mertens, S.; Perys, N.; Heyns, M.; De Gendt, S.; Groeseneken, G.; Vereecken, P. M., Integration and Electrical Characterization of Carbon Nanotube Via Interconnects. *Microelectronic Engineering* **2010,** *(accepted)*.

108. Coiffic, J. C.; Fayolle, M.; Le Poche, H.; Maitrejean, S.; Olivier, S., Realization of via interconnects based on Carbon Nanotubes. *Proceedings of the Ieee 2008 International Interconnect Technology Conference* **2008**, 153-155.

109. Kimizuka, O.; Tanaike, O.; Yamashita, J.; Hiraoka, T.; Futaba, D. N.; Hata, K.; Machida, K.; Suematsu, S.; Tamamitsu, K.; Saeki, S.; Yamada, Y.; Hatori, H., Electrochemical doping of pure single-walled carbon nanotubes used as supercapacitor electrodes. *Carbon* **2008,** *46* (14), 1999-2001.

110. Reddy, A. L. M.; Shaijumon, M. M.; Gowda, S. R.; Ajayan, P. M., Coaxial MnO2/Carbon Nanotube Array Electrodes for High-Performance Lithium Batteries. *Nano Letters* **2009,** *9* (3), 1002-1006.

111. Wang, D.; et al., Highly oriented carbon nanotube papers made of aligned carbon nanotubes. *Nanotechnology* **2008,** *19* (7), 075609.

112. Pint, C. L.; Xu, Y.-Q.; Moghazy, S.; Cherukuri, T.; Alvarez, N. T.; Haroz, E. H.; Mahzooni, S.; Doorn, S. K.; Kono, J.; Pasquali, M.; Hauge, R. H., Dry Contact Transfer Printing of Aligned Carbon Nanotube Patterns and Characterization of Their Optical Properties for Diameter Distribution and Alignment. *Acs Nano* **2010,** *4* (2), 1131-1145.

113. Cao, Q.; Hur, S. H.; Zhu, Z. T.; Sun, Y. G.; Wang, C. J.; Meitl, M. A.; Shim, M.; Rogers, J. A., Highly Bendable, Transparent Thin-Film Transistors That Use Carbon-Nanotube-Based Conductors and Semiconductors with Elastomeric Dielectrics. *Advanced Materials* **2006,** *18* (3), 304-309.

114. Meitl, M. A.; Zhu, Z.-T.; Kumar, V.; Lee, K. J.; Feng, X.; Huang, Y. Y.; Adesida, I.; Nuzzo, R. G.; Rogers, J. A., Transfer printing by kinetic control of adhesion to an elastomeric stamp. *Nat Mater* **2006,** *5* (1), 33-38.

115. Hayamizu, Y.; Davis, R. C.; Yamada, T.; Futaba, D. N.; Yasuda, S.; Yumura, M.; Hata, K., Mechanical Properties of Beams from Self-Assembled Closely Packed and Aligned Single-Walled Carbon Nanotubes. *Physical Review Letters* **2009,** *102* (17), 175505.

116. Hayamizu, Y.; Yamada, T.; Mizuno, K.; Davis, R. C.; Futaba, D. N.; Yumura, M.; Hata, K., Integrated three-dimensional microelectromechanical devices from processable carbon nanotube wafers. *Nat Nano* **2008,** *3* (5), 289-294.

Chapter 3
Synthesis and coating of VA-CNT microstructures

This chapter describes the methods and tools developed to grow VA-CNT microstructures by chemical vapor deposition from lithographically patterned catalyst, and to coat the CNTs after synthesis. These methods result in VA-CNT microstructures with cross-sections as small as 2x2 μm, over cm-scale areas. The height is controlled by the growth time, and can be up to ~1 mm. The effects of feature size, pattern density, and water vapor content on the growth results are identified and discussed. The growth rate is higher for high pattern density but doesn't correlate with the individual feature size within the investigated range (10-100 μm). Observations indicate that the water vapor content of the growth atmosphere has a strong effect on the growth rate. This effect can be suppressed by achieving dry baseline (low water vapor content) in the CVD system before growth by adequate purging with dry gas, although active control of the vapor content was not yet implemented. Additionally, as-grown VA-CNTs can be modified by plasma etching and/or coating. These modification methods tune the chemical and mechanical properties of the CNT forest by changing the structural characteristics and the surface chemistry and enhancing their functionality.

3. 1 Catalyst patterning and deposition

The standard procedure to prepare patterned catalyst for VA-CNT microstructures growth is shown in **Figure 3.1**, and corresponds to the process sequence listed in **Table 3.1**. The process starts with (100) silicon wafers with resistivity of 10-20 Ω-cm. These wafers are acquired from the Michigan Lurie Nanofabrication Facility (LNF) store. The doping type and level does not affect the CNT growth process. The silicon wafers are thermally oxidized at 1100°C for a duration ranging from 1 to 4 hours.

Table 3.1 Process parameters for catalyst patterning by photolithography

	Step	Description	Parameter	Comment
1	Dehydration bake	Bake wafer on hot plate	@ 120°C for 5 min	Optional step
2	Dispense and spread HMDS	Spin coat	@ 500 rpm for 4s	Low speed to cover the wafer
3	Spin HMDS	Spin coat	@ 3000 rpm for 30s	Adhesion promoter for PR
4	Dispense and spread SPR 220 -3.0	Spin coat	@ 500 rpm for 4s	Dispense a volume covering 2/3 of wafer area
4'	Dispense and spread AZ 5214E	Spin coat	@ 500 rpm for 4s	Dispense a volume covering ½ of wafer area
5	Spin SPR 220-3.0	Spin coat	@ 3000 rpm for 30s	Target thickness 2.6 µm
5'	Spin AZ 5214E	Spin coat	@ 4000 rpm for 30s	Target thickness 1.4 µm
6	Pre-exposure bake of SPR 220-3.0	Bake wafer on hot plate	@ 115°C for 90s	Evaporate solvent from PR
6'	Pre-exposure bake of AZ 5214E	Bake wafer on hot plate	@ 100°C for 1 min	Evaporate solvent from PR
7	Expose SPR 220-3.0	Expose in MA/BA-6	6s	Power density 30 mW/cm^2
7'	Expose AZ 5214E	Expose in MA/BA-6	6s	Power density 30 mW/cm^2
8	Post exposure bake of SPR 220-3.0	Bake wafer on hot plate	@ 115°C for 90s	
8'	Post exposure bake of AZ 5214E	Bake wafer on hot plate	@ 110°C for 2 min	Reversal bake
8''	Expose AZ 5214E	Expose in MA/BA-6	50s	Flood exposure (no mask)
9	Develop SPR 220-3.0	Submerge in AZ 300	1 min	Inspect in optical microscope
9'	Develop AZ 5214E	Submerge in MF 319	2-3 min	Inspect in optical microscope
10	Clean wafer	Submerge in DI water	1-2 min	
11	Dry wafer	Dry with nitrogen gun	Hold vertical and dry top to bottom	Wafer ready

The target oxide thickness is usually 3000Å but we used wafers with thickness ranging from 400Å to 1 μm, without apparent effects on subsequent process outcomes.

Second, the wafers are coated with Hexamethyldisilazane (HMDS) solution, dissolved in a solvent such as propylene glycol methyl ether acetate (PGMEA). HMDS functions as a primer and promotes the adhesion between the photoresist and the oxidized silicon surfaces. The spin coating parameters consist of a spreading step at low speed followed by the coating step at a higher speed. SPR 220-3.0 from Rohm and Haas was used as a positive tone resist and AZ 5214E from Clariant GmbH as a negative tone resist. The PR coating recipe is also described in **Table 3.1**.

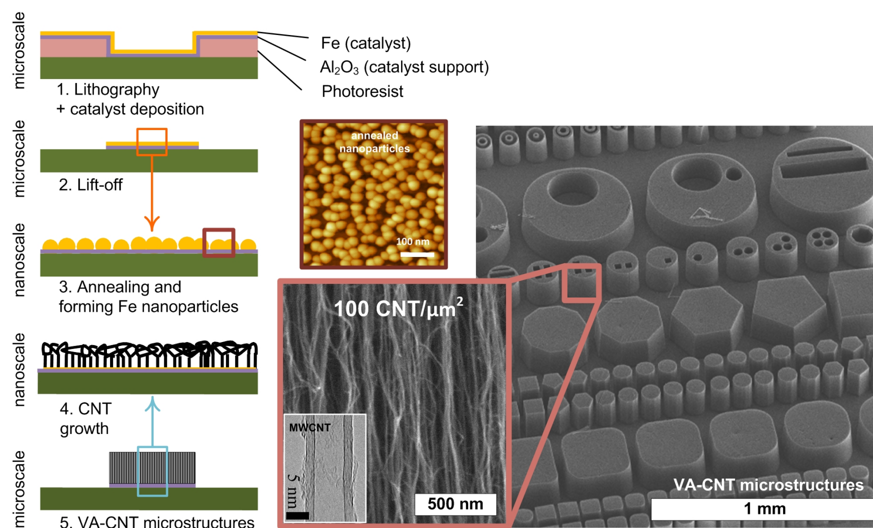

Figure 3.1 Fabrication of VA-CNT microstructures. (a) Process schematic. (b) SEM of a variety of VA-CNT microstructure geometries. Inset showing VA-CNT side wall structure

The exposure is carried out in a Karl Suss mask aligner system MA/BA-6 located in the LNF. The total power density of the UV lamp on this tool is 30 mW/cm^2 where approximately half of the intensity is i-line (365 nm) and half is from the h-line (405 nm). Masks with the required microstructure design can have features as small as 3 microns with this process. If smaller features are required, the stepper lithography system GCA AS200 equipped with 5x optics can be used for projection lithography. The smallest features achieved using this system were circles with 600 nm diameter. The exposure time with this i-line system for SPR-220 3.0 is 0.35 ms.

The PR was developed using a fresh container of developer each time. After development, a very thin layer of PR typically remains in the developed areas; however, we found that it was not necessary to remove this to achieve good catalyst deposition and CNT growth. If needed, a descum process (low power oxygen plasma) can be done in the Plasmatherm 790 system located in LNF.

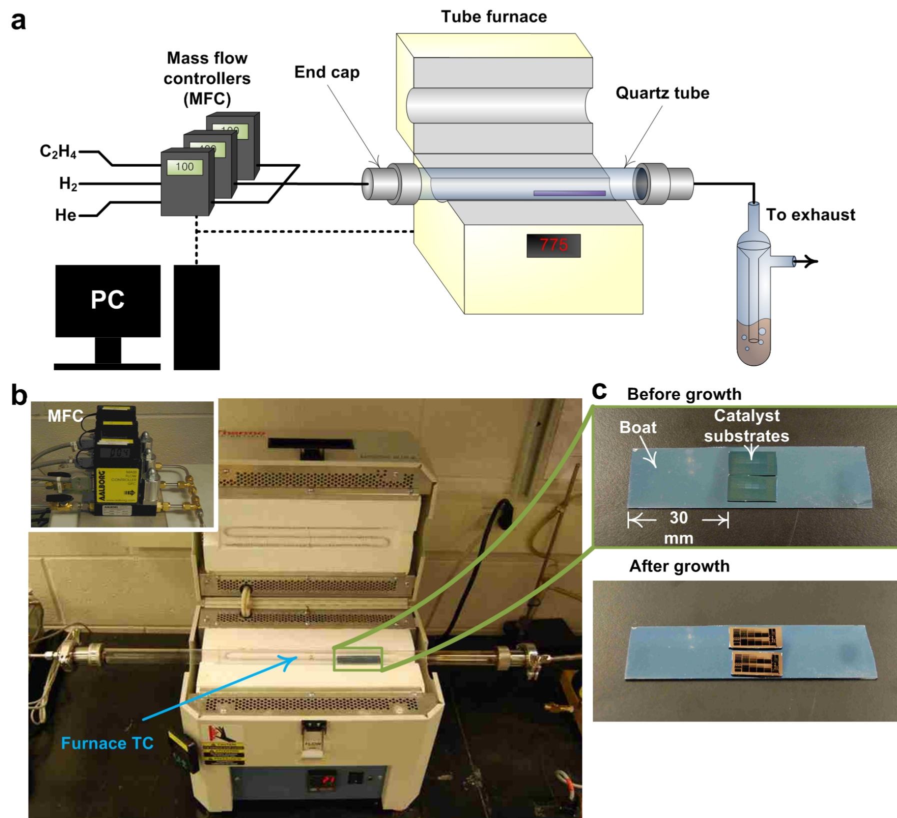

Figure 3.2 Chemical Vapor Deposition system used to grow VA-CNTs. (a) Schematic of the mass flow controllers (MFCs) controlled by a PC and connected to the tube furnace, then though the bubbler to the exhaust. (b) Optical image showing the tube furnace. Inset showing the MFCs. (c) Si substrates with catalust micropatterns before and after CNT growth. Figure prepared by Davor Copic.

The standard catalyst film consists of 10 nm Al_2O_3 and 1 nm Fe. E-beam evaporation and sputtering are used to deposit these films. The parameters for the deposition are listed in Table 3.2. The experiments in this thesis use this standard catalyst configuration unless otherwise stated. Changing the catalyst thickness may however change the growth results as discussed in **Section 3.3.3**.

The lift-off process is done in the Mechanosynthesis Group lab. It consists of 2 cleaning cycles with acetone in an ultrasonic bath (CREST Ultrasonics 1100D) at power setting 8 for 6 minutes. Acetone is replaced between the 2 cycles. After the second cycle, acetone is replaced with 2-propanol and the samples are blow dried with Nitrogen gun.

Table 3.2 CNT catalyst deposition process parameters

	Al_2O_3		**Fe**	
	E-beam	**Sputtering**	**E-beam**	**Sputtering**
Power	11.6%	175W (RF)	12%	200 W
Target thickness	100 Å	100 Å	10 Å	10 Å
Deposition rate	3 Å/s	0.046 Å/s	0.5 Å/s	1.04 Å/s
Deposition time	33 s	2150 s	20 s	9.6 s

3. 2 VA-CNT growth

The silicon wafer with the catalyst micropatterns is diced into rectangular pieces which are then loaded into the tube furnace as shown in **Figure 3.2**. The furnace used in all the experiments is a Thermo-Fisher Minimite with 1" diameter quartz tube. The sample's leading edge is placed at 60 mm downstream the center of the furnace (where the thermocouple is located). We call this location the "sweet spot". The reaction gases are supplied using digital Mass Flow Controllers (MFCs, Aalborg Inc.) connected to a PC with National Instruments™ data acquisition (DAQ) card and Labview™ software interface. As shown in **Figure 3.3**, the recipe consists of 3 stages: catalyst annealing, CNT growth and termination. This recipe is based on previous work by Hart and Slocum[1]. The process is at atmospheric pressure and the exhaust gas is regulated using a mineral oil bubbler. The total flow rate is selected to maintain a laminar flow in the tube.

The standard recipe illustrated in **Figure 3.3** uses He/H_2 flows of 400/100 standard cubic centimeter (sccm) during heating and annealing and $He/H_2/C_2H_4$ flows of 400/100/100 sccm during growth at 775°C. It results in a vertical CNT growth rate in the range of 60-100 μm/min. In separate studies our group has observed that the growth self-

terminates abruptly, i.e., the height stops increasing, after approximately 20 minutes, at a height of approx. 1 mm.[2]

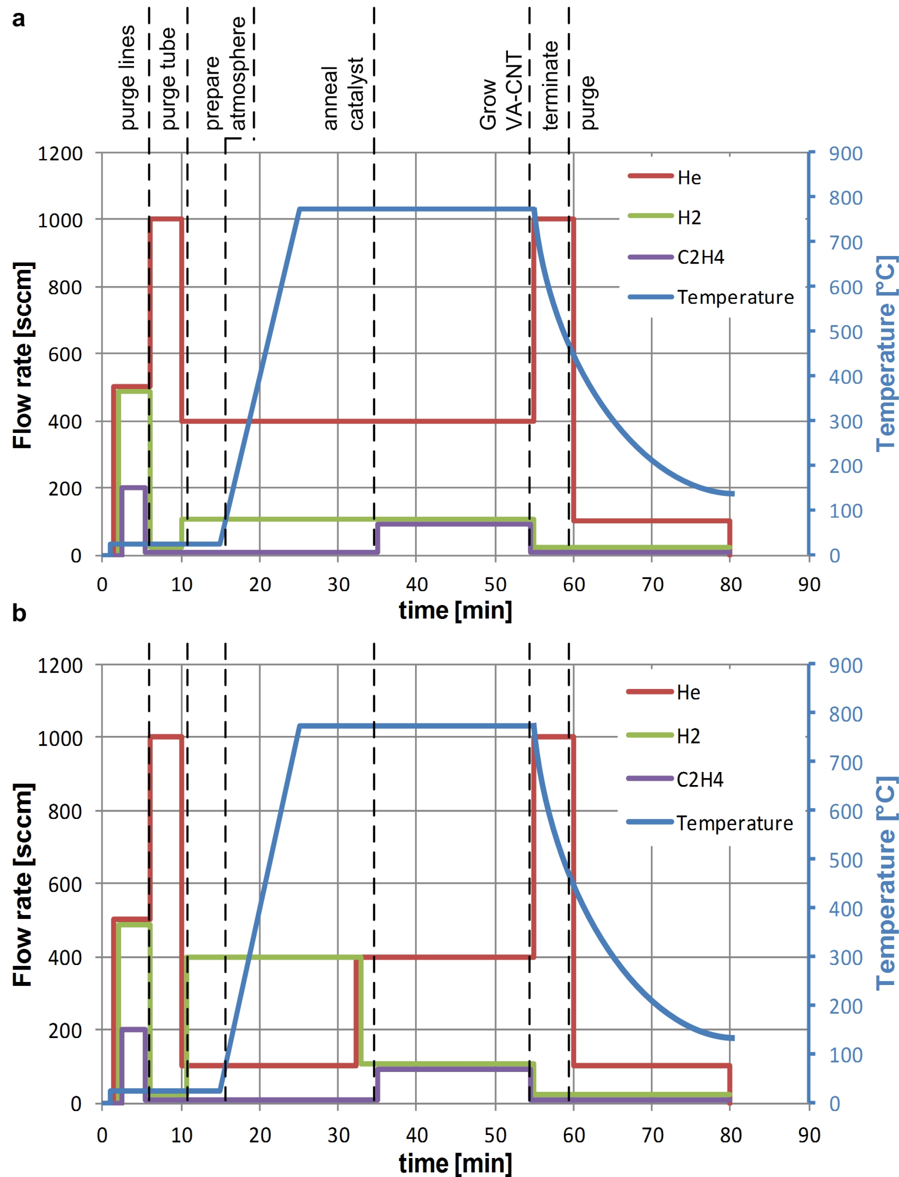

Figure 3.3 VA-CNT growth recipes. (a) Standard New" recipe. (b) "Hybrid" recipe.

The mass density of the CNT microstructures is in the range of 0.015 mg/mm^3 to 0.035 mg/mm^3. The density of graphite is 2.2 mg/mm^3.[3] The microstructures are thus 1% dense foams. The CNT grown by the standard process have mean outer and inner diameters of 10 nm and 6 nm as measured by the Transmission Electron Microscope (TEM) (**Figure 3.1**). Using these values, the areal density of the CNTs is estimated to be

≈$2.5x10^{10}$ CNTs/cm^2. In the following sections, the stages of catalyst annealing and CNT growth and termination are discussed.

3.2.1. Catalyst annealing stage

As-deposited Fe film is continuous with small surface roughness. As the substrate is heated, the film dewets to form nanoparticles. Atomic Force Microscope (AFM) images of the catalyst before and after annealing are shown in **Figure 3.4**. The mechanism of film dewetting (Fe-Al_2O_3 system) is not clearly understood. In general, film dewetting is driven by the contact angle of Fe to the Al_2O_3 substrate. In particular, the material system here consists of three surface energies: Al_2O_3-Fe, Al_2O_3-gas and Fe gas. If the equilibrium contact angle between the Fe and Al_2O_3 is not equal to zero (i.e. perfect wetting), the film is said to be metastable. Hence a continuous film can be driven to another stable configuration where it partially dewets the substrate and forms particles. An essential stage in film dewetting is the nucleation of voids The mechanism of groove nucleation can be mechanical due to strain mismatch[1] or thermodynamic due grooving at the grain boundaries or facets of the Fe film. The relative contribution of each of the factors is beyond the scope of this thesis.

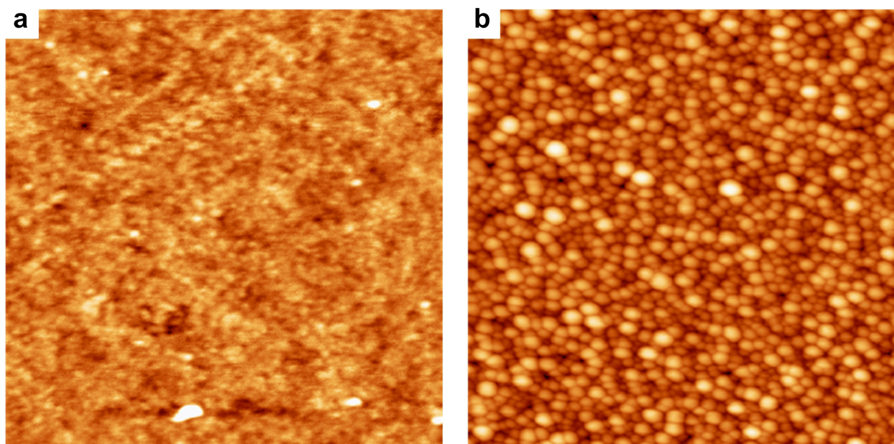

Figure 3.4 Atomic Force Microscope images of the catalyst. (a) Before annealing. (b) After annealing. AFM scans taken by Eric Meshot.

[1]. The substrate thermal expansion coefficient is dominated by the silicon property (≈$3 x10^{-6}$ strain/°C at 20°C). The thermal expansion coefficient value for the Fe film is $11.8 x 10^{-6}$ strain/°C.

The standard catalyst Al_2O_3 10 nm – Fe 1 nm is widely used for MWCNT forests and microstructures growth. Our results indicate that variation from the standard catalyst configuration results in trade-offs between growth rate and density. For example, Al_2O_3 15 nm- Fe 1nm results in 8% higher growth rate but 30% lower density as shown in **Figure 3.5**.

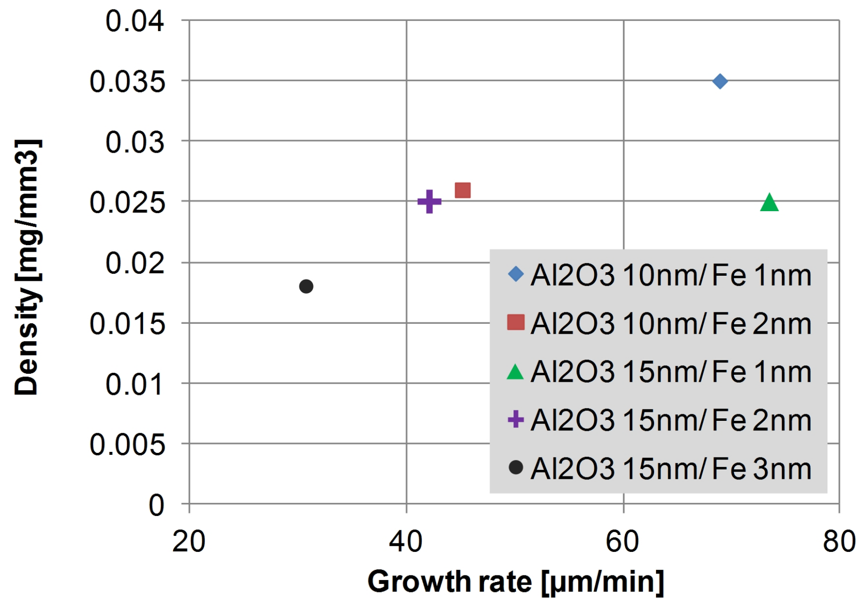

Figure 3.5 VA-CNT growth rate and density for various catalyst compositions.

Further, the gas composition (He/H_2 ratio) during the annealing step also affects the CNT structural characteristics by affecting the size and spacing of the particles. This effect has not been studied but will be briefly discussed here. In principle, the H_2 role in this process is to reduce the oxidized catalyst ($Fe_xO \rightarrow Fe$). Additionally, the H_2 reacts with the O_2 traces to form water vapor which is believed to inhibit Ostwald ripening of the particles after dewetting. Ostwald ripening, also known as coarsening is the migration of Fe atoms from the smaller catalyst nanoparticles into the larger ones.[4] The described dynamics affects the diameter distribution and density of the particles which change the structure of the CNTs. He is an inert carrier gas, and its effects on the particle-substrate interaction are not considered.

My observations indicate that He 400 sccm/H_2 100 sccm annealing recipe (**Figure 3.3a** also know as "Standard New" Recipe) leads to more consistent and typically higher growth rates during the summer, while He 100 sccm/H_2 400 sccm (**Figure 3.3b** also known as the Hybrid Recipe) is more suitable in the winter! Several studies from the Mechanosynthesis group indicate that the growth variations are related to the relative humidity (RH), because there is widespread work on how small water vapor levels affect CNT growth. The RH level in our lab is not controlled and ranges between 65% during the summer and 12% during the winter. Recent experiments performed in our group support my observations by showing that the Hybrid Recipe results in consistent growth results during the summer only when the tube is sufficiently dried by purging for >30 minutes using dry gas (e.g He) before growth starts. The water vapor content was measured using a capacitance based water vapor sensor connected in series with the tube inlet gas line and the time evolution of the water parts per million (ppm) is shown in **Figure 3.6**. The results indicate that the water vapor diffuses into the Teflon tubes used to transport the gases into the furnace. The figure shows that after the tube is dried by purging, the water ppm in the furnace increases abruptly when new gas (e.g. H_2 or C_2H_4) is introduced into the tube. Results from newly installed stainless steel lines indicate that the tube remains dry even when new gases are introduced. I also observed that increasing the annealing time from 10 minutes to 30 minutes leads to more consistent growth results during the summer. This observation is also consistent with the adverse effect of high water vapor concentration on the CNT growth during humid days. However, no difference in the surface morphology of the catalyst could be observed by AFM for annealing with the two different recipes. The conclusion of my efforts is the need for a standard longer He purging time (40 minutes) especially during summer time where humidity is higher than 30%; and possibly introducing controlled amounts of water vapor during the winter season. With a more consistent baseline, the effect of the He/H_2 ratio on the film structure can be more controllably studied.

3.2.2. CNT growth stage

The CNT growth stage starts immediately after the carbon source gas is introduced into the tube. In the standard recipe, we use 100 sccm of ethylene (C_2H_4). As the gas

mixture flows through the tube, it heats up by convection from the tube walls and by radiation. C_2H_4 thermally reacts into a multitude of hydrocarbon species which are active precursors to CNT growth.[5] Because of the decomposition mechanism of C_2H_4 in the tube, the growth must be performed downstream the tube as shown in **Figure 3.2** although the temperature distribution is symmetric with respect to the furnace centerline. The growth rate varies between 60-100 µm/min.

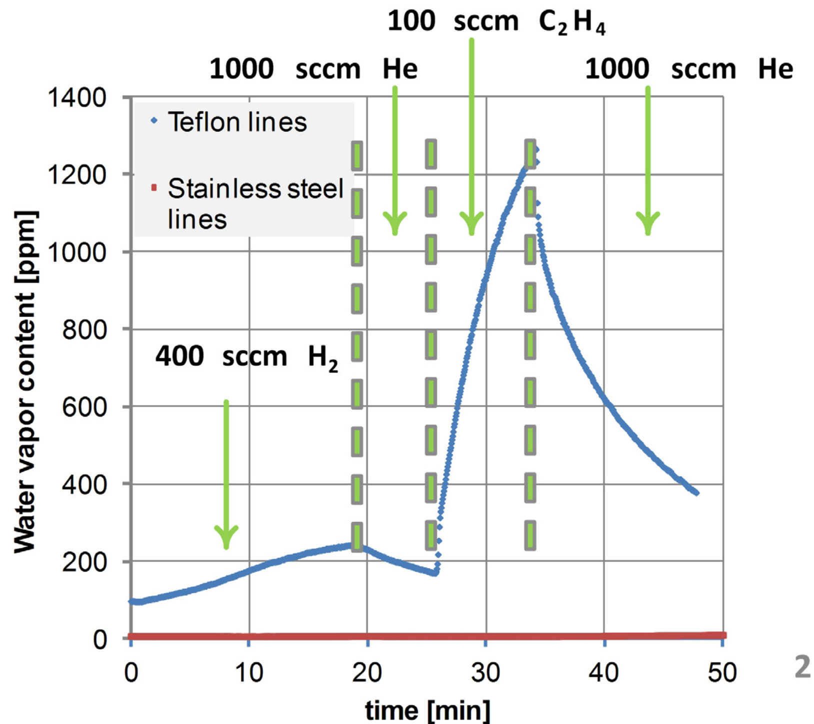

Figure 3.6 Water vapor content time evolution. Plot showing the time evolution of the measured water vapor content in the CVD system with the gases connected by Teflon and Stainless steel lines. Stainless steel line values remain below 10 ppm. Experiments by Erik Polsen and Ryan Oliver.

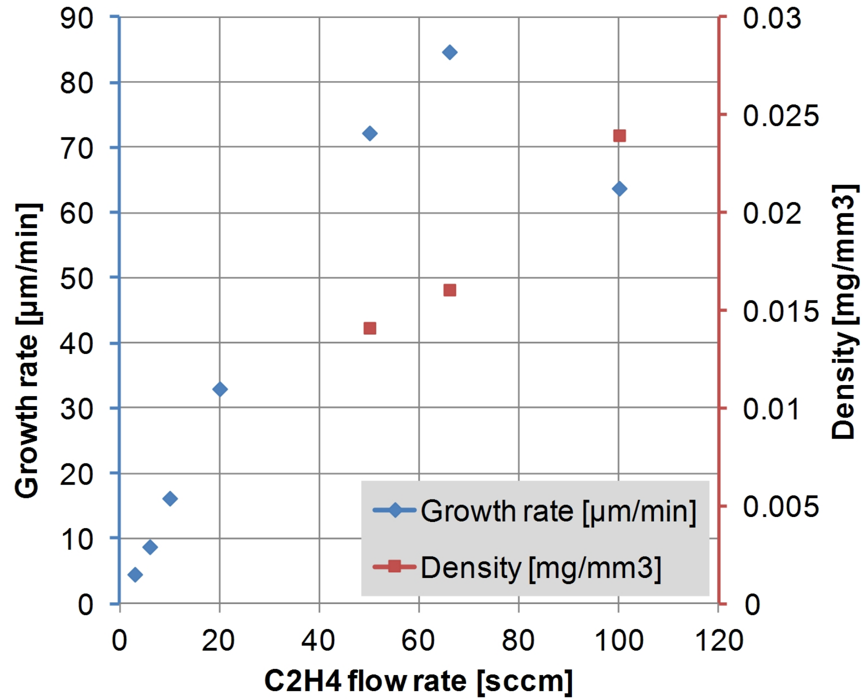

Figure 3.7 VA-CNT growth rate and density for various C_2H_4 flow rates.

The C_2H_4 flow rate affects the growth rate and density as shown in **Figure 3.7**, which also shows a trade-off between the two. These experiments were performed under controlled conditions on patterned and non-patterned catalyst. The density is estimated from mass and area measurements from non-patterned catalyst. Before the experiments, the tube was dried by annealing in air for 30 minutes at 875°C. The first growth was performed and the samples disregarded to eliminate the variation caused by environmental effects (i.e., water vapor) on the gas lines. After each growth the tube was baked in air for 30 minutes at 875°C to burn-off any hydrocarbons deposited on the inner tube wall during the growth. All the growth experiments were carried out in the same day after the system initialization steps described above. Te results demonstrate the trade-off between growth rate and density as a function of the C_2H_4 flow rate.

3.2.3. The termination stage

The termination recipe affects the adhesion of the CNT to the substrate. When the C_2H_4 and H_2 are abruptly turned off and replaced by He flow, the CNT microstructures have low adhesion to the substrate. On the other hand, if the growth is terminated by an

abrupt change in temperature without any change in the supply gases, the CNT microstructures have high adhesion to the substrate.[6] This is achieved by opening the lid of the furnace to allow for a higher cooling rate. The adhesion to the substrate affects the rolling and the capillary forming of VA-CNT microstructures. **Figure 3.8**. shows exemplary low adhesion and high adhesion microstructures made by capillary folding.

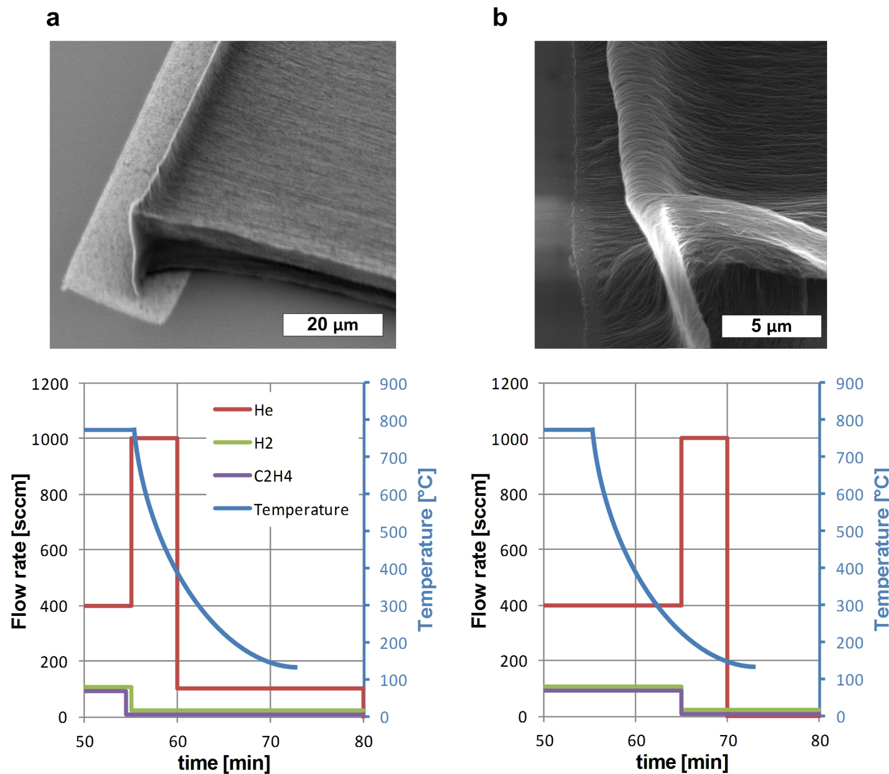

Figure 3.8 VA-CNT growth termination recipe. SEMs showing (a) low and (b) high adhesion CNT microstructures collapsed by capillary forces obtained by the recipes shown at the bottom.

The adhesion of the CNTs to the Fe nanoparticles (and hence to the substrate) after growth can be enhanced by forming a thin carbon layer around the nanoparticle and at the CNT-nanoparticle interface by rapid cooling in the growth atmosphere as shown in **Figure 3.8b**. As the furnace temperature drops, the CNT growth terminates when the temperature reaches ≈550°C. The continued C_2H_4 flow during this stage leads to the deposition of a carbon shell around the nanoparticles which promotes the adhesion by forming C-C bonds. On the other hand, when the carbon source is abruptly turned off (**Figure 3.8a**), the carbon atoms precipitate out from the Fe nanoparticles and react with traces of oxygen and H_2O. In this case, the furnace temperature is allowed to slowly drop

by switching-off the power to the heating elements without opening the furnace lid. Addition of H_2 during this stage is optional and leads to further etching of the carbon. This hypothesis is confirmed by Pint et al. using X-ray Photoelectron Spectroscopy (XPS).

3. 3 Effect of pattern size and density (with Yuki Matsuoka)

The size and density of the catalyst patterns affect the growth results. This is confirmed by the observation of increased CNT growth rate for densely packed catalyst patterns compared to highly spaced or isolated features on the same substrate. Yuki Matsuoka and I designed a mask for catalyst patterning to capture controlled variations in patterns size and density as summarized in **Figure 3.9**. Three arrays of circles with diameters of 10, 30 and 90 µm were designed. The spacing among the circles is calculated to achieve constant total fill fraction (fill fraction = catalyst area per substrate area) for each diameter.

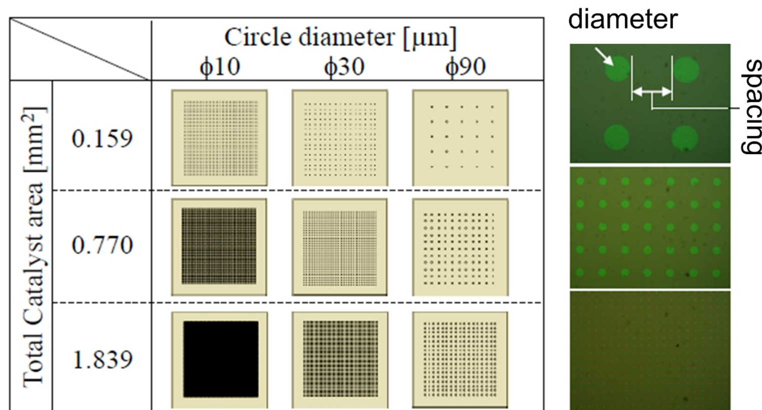

Figure 3.9 Mask for studying the effect of catalyst size and density on CNT growth. Figure prepared by Yuki Matsuoka.

These results, shown in **Figure 3.10**, indicate that at fill fraction (i.e. low density patterns), the growth rate is smaller. Varying the fill fraction by an order of magnitude changes the growth rate by 15%. Jeong et al. experimentally studied this effect and they contribute the growth rate dependency on the pattern density to the number of walls of the individual CNTs.[7] Hence, they show that dense patterns have a higher growth rate but a smaller number of CNT walls. While this variation seems small, it can lead to

bending the CNT microstructures as shown in **Figure 3.11**. Variations in the local pattern density surrounding an individual catalyst feature can lead to gradients in CNT growth rates across the same feature (**Figure 3.11**). This creates mechanical stresses on the CNT microstructure as it is growing and leads to microstructure bending. This effect is similar to the actuation mechanism of bimetallic strips.

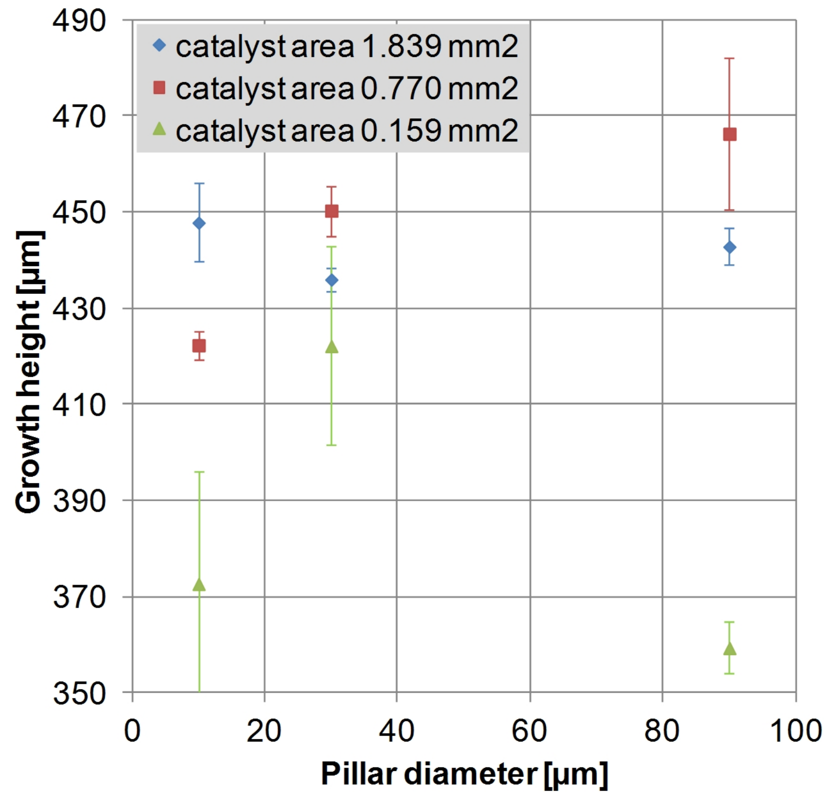

Figure 3.10 VA-CNT growth rate for various pattern diameters and density

3. 4 Plasma etching of VA-CNT

Plasma etching can be used to modify the top surface (the "crust") of the CNT forests and hence change the mechanical interactions among the CNTs. Etching is performed in Plasmatherm 790 located in the LNF facility. This tool consists of parallel-plate Reactive Ion Etching (RIE) chamber. The etching conditions are summarized in **Table 3.3**. **Figure 3.11** shows the crust before and after plasma etching.

Table 3.3 Process parameters for plasma etching of VA-CNTs.

Step	**Gas 1**	**Gas 2**	**Pressure**	**RF Power**	**Duration**
1	O_2 20 sccm	-	75 mTorr	80 mW	20 s
2	O_2 20 sccm	Ar 20 sccm	75 mTorr	80 mW	40s

Modifications in the structural characteristics of the crust can hence change mechanocapillary forming. Other changes due to plasma etching include changing the CNT density, inducing defects in the CNTs, and forming –OH groups on the CNT and substrate surface.

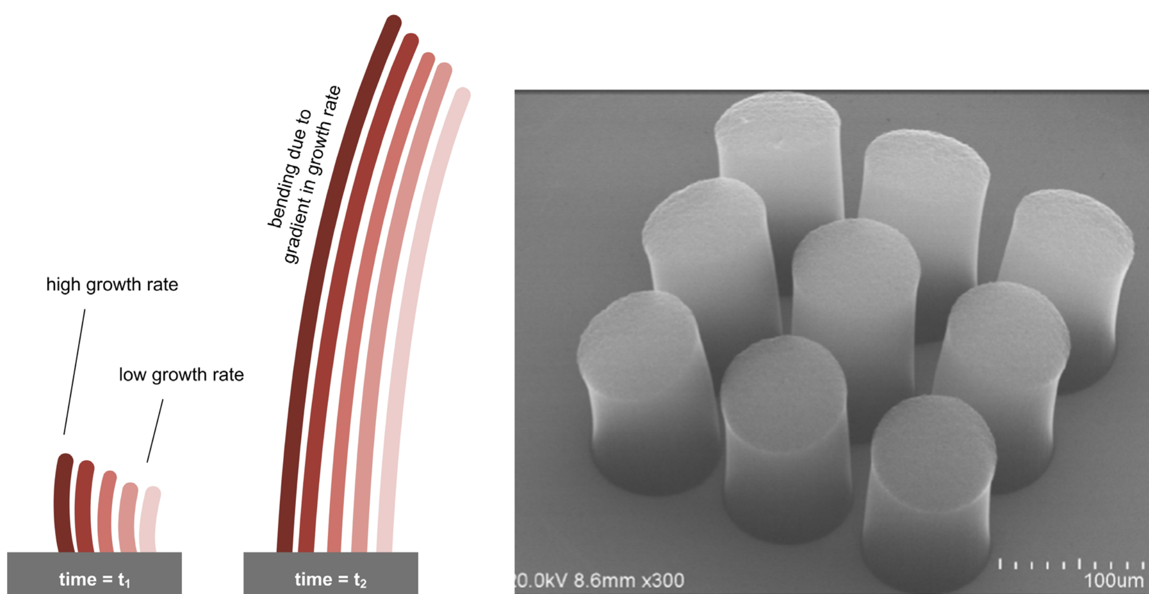

Figure 3.11 VA-CNT bending due to variation in growth rate across the same feature.

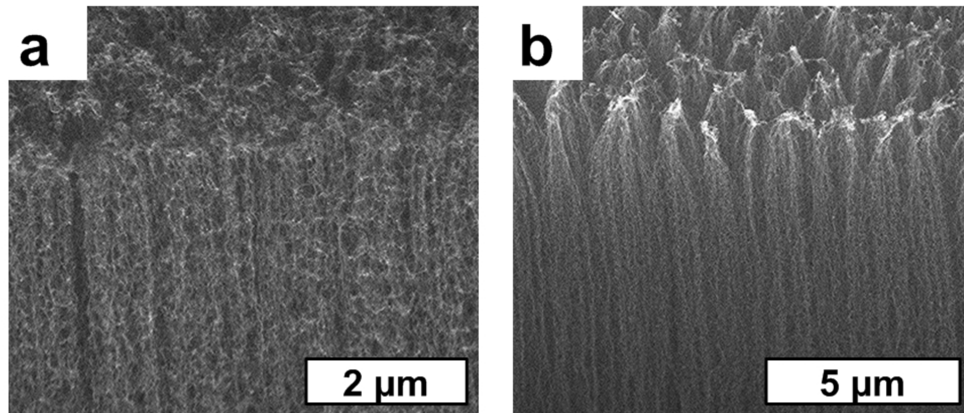

Figure 3.12 VA-CNT top surface morphology. (a) before and (b) after plasma etching.

3. 5 Coating of VA-CNT microstructures

The CNT microstructures can be modified and functionalized by several types of coatings. Developing processes for coating the CNT microstructures with ceramics or polymers (e.g. Reactive Coatings) is motivated by the several demonstrations of these coatings in enhancing the robustness and the mechanical properties of the CNTs making functional interfaces for batteries,[8] immobilization of a number of different entities including proteins,[9, 10] peptides,[11] DNA,[12] and quantum dots.[13]

3.5.1. Ceramics coatings by Atomic Layer Deposition

Atomic Layer Deposition (ALD) can be used to conformally deposit thin layers of ceramics such as Al_2O_3 around the surface of individual CNTs within the microstructures. ALD is a special type of CVD where the gas phase reaction constituents are not simultaneously introduced into the system. Instead, the deposition in ALD consists of an integer number of cycles. During each cycle, the gas precursors are sequentially introduced in two half-reaction stages. By purging and/or evacuating the chamber after each stage, only the gas species adsorbed on the surface remain. Hence the material deposition during each cycle is self-limiting and produces a constant film thickness.

The ALD of Al_2O_3 on CNT has been studied by Professor Roy Gordon and colleagues at Harvard University.[14] The challenge in coating CNTs with ALD is

achieving a conformal coating during the first half-reaction stage without creating defects on the CNT surface. They found that using nitrogen dioxide (NO_2) gas and trimethylaluminum (TMA, Al[CH3]$_3$) vapor leads to the formation of uniform conformal layers physically adsorbed on the CNT surface.

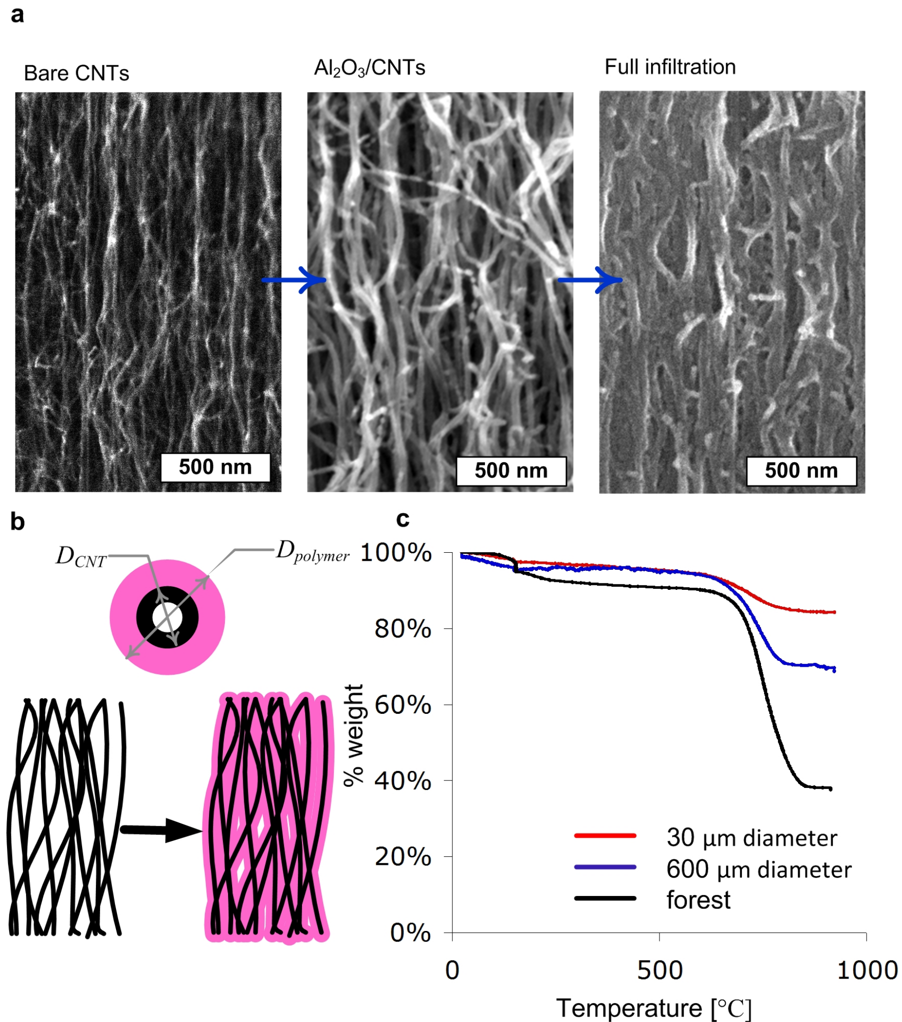

Figure 3.13 Al_2O_3 coating of VA-CNT by Atomic Layer Deposition. (a) SEM of the VA-CNT side walls (from left to right) with no coating, 10o cycles of Al_2O_3 and 1000 cycles Al_2O_3. (b) Schematic showing conformal coating of the CNTs. (c) Thermogravimetric Analysis of VA-CNT cylindrical microstructures with30 and 60 µm diameter coated with 1000 cycles of Al_2O_3.

I used TMA, Al[CH3]$_3$/DI-H_2O 20 ms half-cycle pulses at temperatures ranging from 80°C to 300°C in the Oxford OpAL system located in the LNF. The cycle growth rate is 1.1 Å/cycle as measured by ellipsometry on a flat Si substrate.

The coating is conformal to the CNT surfaces as shown in SEM images of **Figure 3.13**. Coating the CNT microstructures with a large number of cycles (1000 cycles) leads to filling of the microstructures thus forming a Al_2O_3 matrix-CNT fiber composite. The uniformity of the coating varies across the CNT microstructure due to the gas diffusion. More specifically, the coating thickness is higher along the edges and on the top of the CNT microstructures. This effect is characterized by conducting Thermo-Gravimetric Analysis (TGA) of ALD coated samples (100 cycles) consisting of cylindrical CNT microstructures with 30 μm and 600 μm diameters. The TGA final temperature is 1000°C and the remaining mass consists of Al_2O_3 considering that the CNTs burn at ≈ 700°C.

To assess the penetration depth, Alex Hryn (NNIN-REU summer student 2009) and I formulated an idealized model of CNTs conformally coated with ALD as shown in **Figure 3.13b**. An ideally coated sample of CNTs would have ~83% mass remaining after the CNTs burn away. From the TGA graph of Figure 3.13c, the 30μm CNT microstructures are fully coated. The results from the 600μm sample however indicated that the CNTs were not fully coated. Assuming that CNTs are either fully coated or not coated at all, a rough estimate of the penetration depth is estimated to be ≈20 μm into the pillars.

3.5.2. Polymer coating by Chemical Vapor Deposition (with Xiaopei Deng)

Professor J. Lahann's group in the Chemical Engineering department developed CVD polymerization technology for the deposition of a wide range of different Reactive Coatings.[15] These reactive coatings share the same polymer main chain, poly-*p*-xylylene, but differ in the nature of their substituents, which can be presented on aromatic or aliphatic parts of the polymer.

Xiaopei Deng and I developed a method to conformally coat VA-CNT with various functional polymer films using CVD.[16] As-grown VA-CNT are plasma etched following the process parameters described in **Table 3.3**. The CVD coating was done and characterized by Xiaopei Deng. The silicon substrates with the VA-CNTs are placed in the polymerization CVD chamber. The starting material 4-trifluoroacetyl [2.2]

paracyclophane was synthesized via Friedel–Crafts acylation of [2.2] paracyclophane.[17] A pressure of 0.3 mbar and temperatures of 90–100 °C are employed for the sublimation of the starting material. Then the starting material is transferred in a stream of argon carrier gas (20 sccm) to the pyrolysis zone (670 °C). Following pyrolysis, the diradicals are transferred into the deposition chamber, where polymerization occurrs. The wall temperature is adjusted to 120 °C, and the substrates are cooled to 15 °C to optimize the deposition onto the substrate and the deposition rate is controlled at a constant rate 0.5 Å/s. Rotation of the sample holder ensures uniform film deposition.

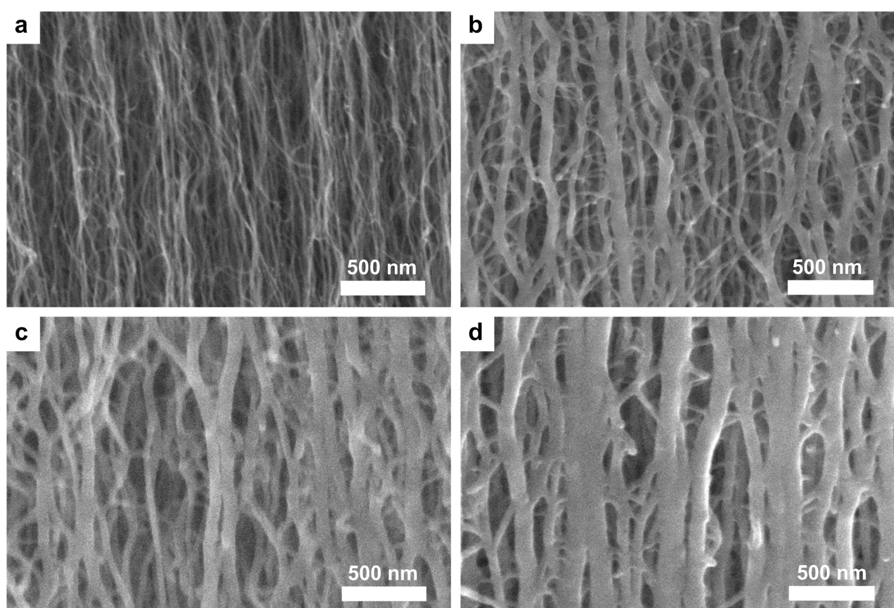

Figure 3.14 Parylene coating of VA-CNT by Chemical Vapor Deposition. (a-d) SEM images of side showing (a) no coating, (b) coating for 10 min, (c) for 20 min, and (d) for 30 min.

We selected poly[4-trifluoroacetyl-p-xylylene-co-pxylylene] as the reactive coating because of its documented reactivity towards hydrazides and hydrazines. The process could be similarly applied to coatings with other functional groups, such as active esters, anhydrides, amines, acetylene, or tertiary bromides.32 Polymer deposition followed a modified Gorham process, where 4-trifluoroacetyl [2.2] paracyclophane was sublimated at a temperature of 90-100 °C and a pressure of 0.3 mbar. Subsequent cleavage of the C-C bonds of the bridge at 670 °C resulted in the corresponding quinodimethanes (monomers). Next, the reactive species were allowed to enter the deposition chamber, where they spontaneously deposited on the CNT structures.

This technique can be used to coat the CNTs with various thicknesses as shown in **Figure 3.14**. The SEM images indicate that the conformal coating forms a shell around individual CNTs and/or CNT bundles. By changing the deposition time we achieved control on the coating thickness which allows the tuning of chemical and mechanical properties as discussed in Chapter 6.

3. 6 Bibliography

1. Hart, A. J.; Slocum, A. H., Rapid growth and flow-mediated nucleation of millimeter-scale aligned carbon nanotube structures from a thin-film catalyst. *Journal of Physical Chemistry B* **2006,** *110* (16), 8250-8257.

2. Meshot, E. R.; Hart, A. J., Abrupt self-termination of vertically aligned carbon nanotube growth. *Applied Physics Letters* **2008,** *92* (11), 113107.

3. Bedewy, M.; Meshot, E. R.; Guo, H. C.; Verploegen, E. A.; Lu, W.; Hart, A. J., Collective Mechanism for the Evolution and Self-Termination of Vertically Aligned Carbon Nanotube Growth. *Journal of Physical Chemistry C* **2009,** *113* (48), 20576-20582.

4. Amama, P. B.; Pint, C. L.; McJilton, L.; Kim, S. M.; Stach, E. A.; Murray, P. T.; Hauge, R. H.; Maruyama, B., Role of Water in Super Growth of Single-Walled Carbon Nanotube Carpets. *Nano Letters* **2008,** *9* (1), 44-49.

5. Plata, D. L.; Meshot, E. R.; Reddy, C. M.; Hart, A. J.; Gschwend, P. M., Multiple Alkynes React with Ethylene To Enhance Carbon Nanotube Synthesis, Suggesting a Polymerization-like Formation Mechanism. *Acs Nano* **2010,** *4* (12), 7185-7192.

6. Pint, C. L.; Xu, Y.-Q.; Pasquali, M.; Hauge, R. H., Formation of Highly Dense Aligned Ribbons and Transparent Films of Single-Walled Carbon Nanotubes Directly from Carpets. *Acs Nano* **2008,** *2* (9), 1871-1878.

7. Jeong, G.-H.; Olofsson, N.; Falk, L. K. L.; Campbell, E. E. B., Effect of catalyst pattern geometry on the growth of vertically aligned carbon nanotube arrays. *Carbon* **2009,** *47* (3), 696-704.

8. Reddy, A. L. M.; Shaijumon, M. M.; Gowda, S. R.; Ajayan, P. M., Coaxial MnO2/Carbon Nanotube Array Electrodes for High-Performance Lithium Batteries. *Nano Letters* **2009,** *9* (3), 1002-1006.

9. Lahann, J.; Balcells, M.; Lu, H.; Rodon, T.; Jensen, K. F.; Langer, R., Reactive polymer coatings: A first step toward surface engineering of microfluidic devices. *Analytical Chemistry* **2003,** *75* (9), 2117-2122.

10. Elkasabi, Y.; Nandivada, H.; Chen, H. Y.; Bhaskar, S.; D'Arcy, J.; Bondarenko, L.; Lahann, J., Partially Fluorinated Poly-p-xylylenes Synthesized by CVD Polymerization. *Chemical Vapor Deposition* **2009,** *15* (4-6), 142-149.

11. Lee, K. B.; Kim, D. J.; Lee, Z. W.; Woo, S. I.; Choi, I. S., Pattern generation of biological ligands on a biodegradable poly(glycolic acid) film. *Langmuir* **2004,** *20* (7), 2531-2535.

12. Thevenet, S.; Chen, H. Y.; Lahann, J.; Stellacci, F., A generic approach towards nanostructured surfaces based on supramolecular nanostamping on reactive polymer coatings. *Advanced Materials* **2007,** *19* (24), 4333-+.

13. Chen, H. Y.; Lahann, J., Vapor-assisted micropatterning in replica structures: A solventless approach towards topologically and chemically designable surfaces. *Advanced Materials* **2007,** *19* (22), 3801-+.

14. Farmer, D. B.; Gordon, R. G., Atomic Layer Deposition on Suspended Single-Walled Carbon Nanotubes via Gas-Phase Noncovalent Functionalization. *Nano Letters* **2006,** *6* (4), 699-703.

15. Lahann, J. r.; Balcells, M.; Lu, H.; Rodon, T.; Jensen, K. F.; Langer, R., Reactive Polymer Coatings:â€‰ A First Step toward Surface Engineering of Microfluidic Devices. *Analytical Chemistry* **2003,** *75* (9), 2117-2122.

16. Tawfick, S.; Deng, X. P.; Hart, A. J.; Lahann, J., Nanocomposite microstructures with tunable mechanical and chemical properties. *Physical Chemistry Chemical Physics* **2010,** *12* (17), 4446-4451.

17. Lahann, J.; Klee, D.; Hocker, H., Chemical vapour deposition polymerization of substituted [2.2]paracyclophanes. *Macromolecular Rapid Communications* **1998,** *19* (9), 441-444.

Chapter 4
Mechanical rolling of VA-CNT

High density assemblies of horizontally aligned CNTs (HA-CNTs) with controlled geometry, packing, and placement could potentially replace metals as interconnects in existing and emerging electronic systems. This chapter describes the methods and tools developed to fabricate HA-CNT ribbons and sheets with controlled characteristics and to transfer them from the growth silicon substrates to flexible polymer substrates. In this process, a small roller is used to "topple" tall VA-CNT microstructures and to simultaneously compress them, thus increasing the packing fraction of CNTs from approximately 2% to as high as 60%. The resulting ribbon width ranges from <100 μm to 5 cm and the thickness range from 300 nm to 20 μm. CNT sheets are fabricated by rolling overlapping ribbons from a line pattern cm-scale. We formulate design guidelines for selection of pattern geometry, roller diameter and material, and the forces in the rolling process. The HA-CNT structures are transferred to other substrates using kinetically controlled peeling and printing, enabling integration with CMOS and MEMS fabrication, and with alternative substrates such as flexible plastics.

4. 1 Process and machine design

VA-CNT microstructures are grown by thermal CVD on a silicon substrate then the VA-CNTs are transformed into densely packed HA-CNTs by direct mechanical rolling using a small diameter stainless steel pin, as shown in **Figure 4.1** and **4.2**.[1] The catalyst patterning and growth processes are described in Chapter 3. VA-CNT microstructures resembling thin "blades" are grown to 1-2 mm height. The termination stage in the growth recipe is used to control the adhesion of the blades to the substrate.[2] Rolling is achievable with both low and strong adhesion of the VA-CNT to the substrate. However, if dry transfer printing to other substrates is required, low adhesion recipe is used and the HA-CNTs are easily delaminated from the substrate without the need of a carrier film.

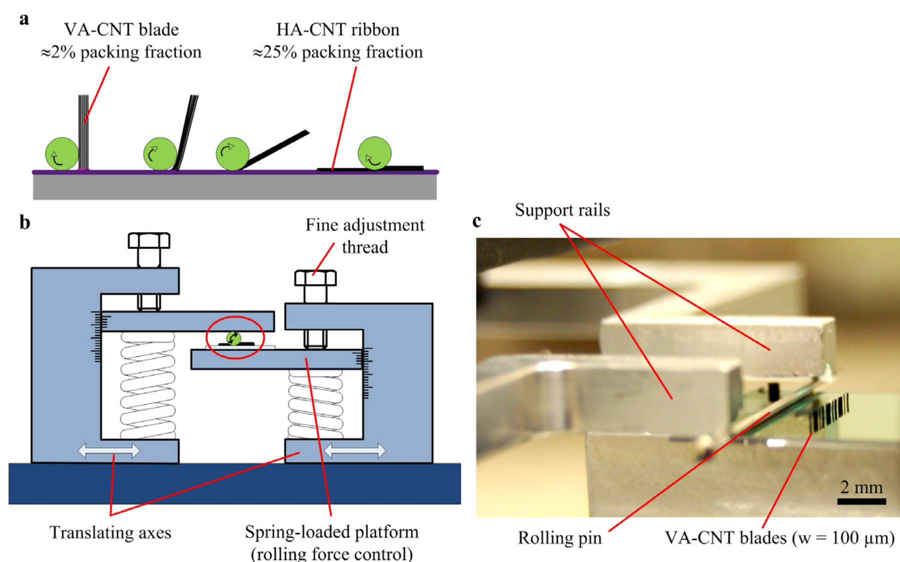

Figure 4.1 Rolling of VA-CNT blades into densely packed HA-CNTs. (a) Kinematics of the rolling process. (b) Schematic of the force-controlled rolling machine. (c) Optical image showing VA-CNT blades mounted in the machine before rolling.

After growth, the substrate with VA-CNT blades is placed in a custom-built benchtop apparatus (**Figure 4.1** and **4.4**), wherein a stainless steel roller is held between the substrate and a pair of rails. The substrate and rails are moved in opposite directions, causing the roller to rotate about a fixed virtual pivot. Contact between the roller and the CNTs first topples the VA-CNT blades to the horizontal orientation, and then the contact pressure between the roller and CNTs compacts the CNTs as the roller moves across the

substrate. The applied force determines the thickness of the HA-CNT ribbons after rolling. The force is adjusted using springs in the machine frame.

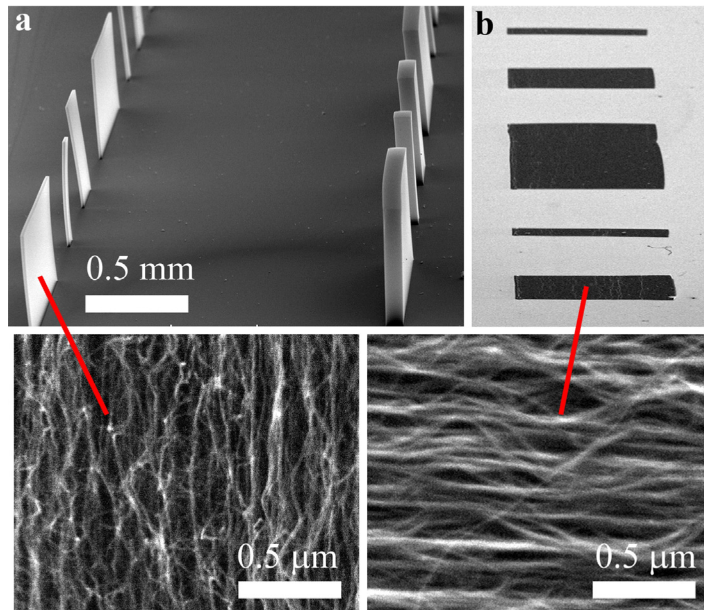

Figure 4.2 SEM images of CNTs before and after rolling. (a) as-grown VA-CNTs having 20 and 100 mm width and(b) HA-CNTs fabricated by rolling followed by capillary densification. Higher-magnification images show CNT alignment in each configuration.

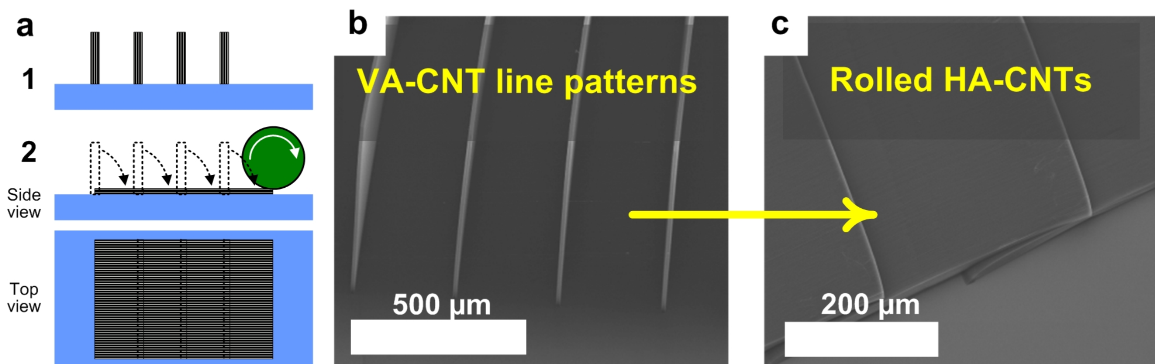

Figure 4.3 Rolling of CNT sheets. (a) Schematic of rolling of line patterns to form overlapping CNT sheets. SEM image of (a) as-grown CNT line patterns and (b) HA-CNT sheets after rolling.

Initial contact between a VA-CNT blade and the roller topples the blade by kinking the structure at its base, causing little shear in the upper portion of the blade. Minimizing shear and buckling of the VA-CNTs during the rolling process is essential for creating HA-CNT films with uniform texture, and this is achieved using a roller diameter less than the VA-CNT blade height, and designing the VA-CNT blade width to be substantially

less than the height. In the experiments reported here, we use a 0.3 mm to 0.6 mm diameter stainless steel pin to roll VA-CNTs with 200 μm to 2 mm initial height and 20-100 μm initial width. Our method contrasts recent approaches that shear a uniform VA-CNT forest into a thin film, using a much larger diameter roller that is separated from the CNTs by a flexible mesh.[3] In our experience with this alternative approach, entanglement and van der Waals forces among the VA-CNTs induce significant shear, and therefore the resulting CNT films are not well aligned through their thickness. By rolling series of line patterns, overlapping HA-CNT can form cm-scale CNT sheets as shown in **Figure 4.3**.

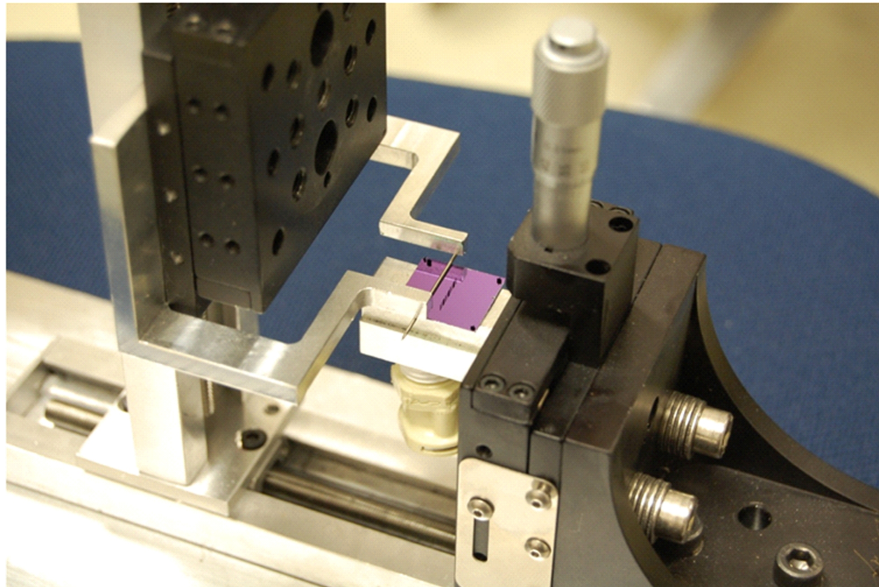

Figure 4.4 Optical image of the rolling machine showing mounted CNT substrate and pin before rolling.

Further, for effective transformation, the HA-CNTs must not adhere to the roller. Since the resultant force from the van der Waals attraction between the CNTs and roller is directly proportional to the contact area, it is desirable to minimize the local contact area between the CNTs and the roller. From Hertzian contact mechanics,[4] the width of the contact area between a cylinder (diameter d, length l, modulus E_1, poisson's ratio ν_1) and a plane (E_2, ν_2), is

$$b = \left[\frac{2Fd}{\pi l}\left(\frac{1-\nu_1^2}{E_1}+\frac{1-\nu_2^2}{E_2}\right)\right]^{1/2} \tag{1}$$

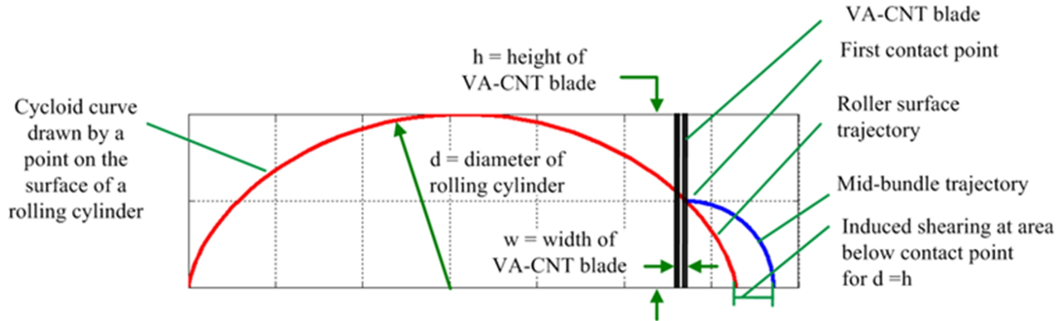

Figure 4.5 Kinematics of rolling. Based on optical microscopy during the rolling process, we observed that the CNTs show only little slip with respect to the roller. Thus the contact point of the CNTs and the roller follow the cycloid curve and cause shear and buckling in this area.

Therefore, a small diameter roller made of a material having high elastic modulus gives relatively weak adhesion to the CNTs. This simple formula agrees with our observation that the CNTs tend to stick to rollers having a substantially larger diameter than used in the present study, and/or to rollers made of a soft material (e.g., PDMS or Nylon). Further, large rollers cause undesirable shearing and buckling of the VA-CNTs. (**Figure 4.5**)

4. 2 Alignment characteristics of HA-CNT

Our force-controlled rolling process creates HA-CNT ribbons with uniform thickness and significantly higher packing density than the original VA-CNT blades, as shown in **Figure 4.2**. The rolling process preserves and possibly increases the CNT alignment, as quantified by calculating Herman's orientation parameter (H) from synchrotron small-angle X-ray scattering (SAXS) data.[5] Example SAXS images are shown in **Figure 4.6**. For VA-CNT blades characterized by transmission SAXS, H = 0.2; for HA-CNT ribbons characterized by grazing incidence (GI-) SAXS, H = 0.4. Precise comparison of H values between the transmission and grazing incidence configurations is not possible as Herman's parameter is highly sensitive to background scattering; however, from the FWHM of the azimuthal intensity distribution, we can judge that the alignment of the HA-CNTs is at least as good as the initial VA-CNTs, and logically should increase as the

CNTs are densified during processing. Further, as we expect that the X-ray beam penetrates fully through the HA-CNT ribbon thickness, SAXS verifies that the ribbons exhibit strong alignment through their thickness.

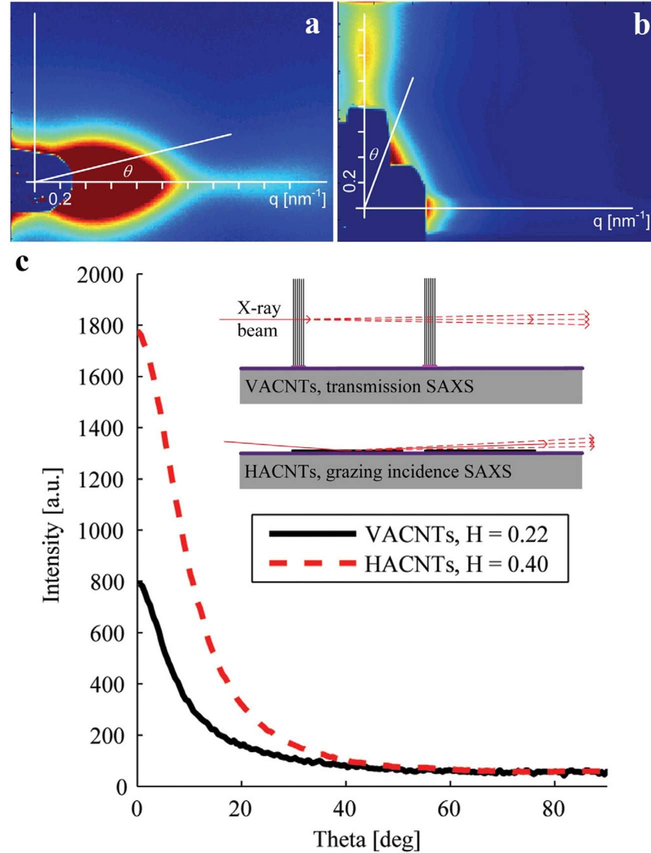

Figure 4.6 Characterization of alignment of CNT microstructures by synchrotron X-ray scattering. (a) Transmission SAXS image of VA-CNTs before rolling; (b) grazing incidence SAXS image of HA-CNTs after rolling; and (c) comparison of azimuthal intensity distributions

4. 3 Thickness and density of HA-CNT

The final thickness (t) and packing density of the HA-CNT ribbons is controlled by the initial width (w) of the VA-CNT blades prior to transformation, and by the force applied to the roller. **Figure 4.7** plots the densification ratio (w/t) and packing fraction of HA-CNT ribbons created from VA-CNT blades having w = 20 µm and 100 µm. The densification factor increases linearly with the normal force applied during the rolling process. This linear plastic behavior is due to the initially low density of VA-CNTs; the CNTs are easily compacted in the direction perpendicular to their alignment. The HA-

CNT density is calculated using the known VA-CNT density and the measured densification ratio. The VA-CNT density is calculated from measurements of the mass (using a microbalance) and the CNT microstructure volume (using SEM) of a VA-CNT forest grown fully over a silicon substrate. The CNTs used in this study have average outer diameter 10 nm and inner diameter 6 nm, as also determined by SAXS. [21] The VA-CNT density is 0.02 g/cm^3, corresponding to a packing fraction of 0.016. The density at the maximum packing fraction of 0.9 is 1.26 g/cm^3, and for comparison the density of graphite is 2.2 g/cm^3.

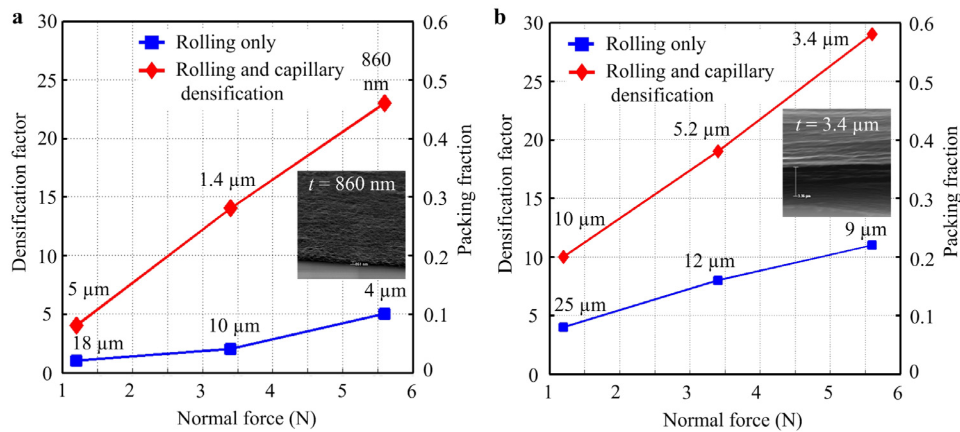

Figure 4.7 Control of HA-CNT geometry by control of rolling force: densification factor and packing fraction for (a) 20-mm and (b) 100-mm VACNT blade widths. Insets show side views of typical HA-CNT ribbons after rolling and capillary densification at 5.6 N applied force. Thickness values are written next to each data point and are averages for three samples processed under identical conditions.

After the rolling process, significant further densification is achieved by infiltrating the HA-CNTs with an organic solvent such as acetone, and subsequently evaporating the solvent. Evaporation of the solvent draws the CNTs into a more tightly packed arrangement. In agreement with previous studies of elastocapillary aggregation of fibers and hair,[15] the final packing fraction depends on the initial spacing (packing fraction) of the HA-CNTs after the rolling process. Therefore, maximal packing of HA-CNTs is achieved by combining mechanical and capillary densification methods. The maximum densification factor achieved in this study is 30, giving a final packing fraction of approximately 0.6. Raman spectroscopy (**Figure 4.8**) shows that the G/D peak intensity

ratio is invariant before and after rolling and densification, therefore suggesting that the CNTs are not damaged during the rolling and densification steps.

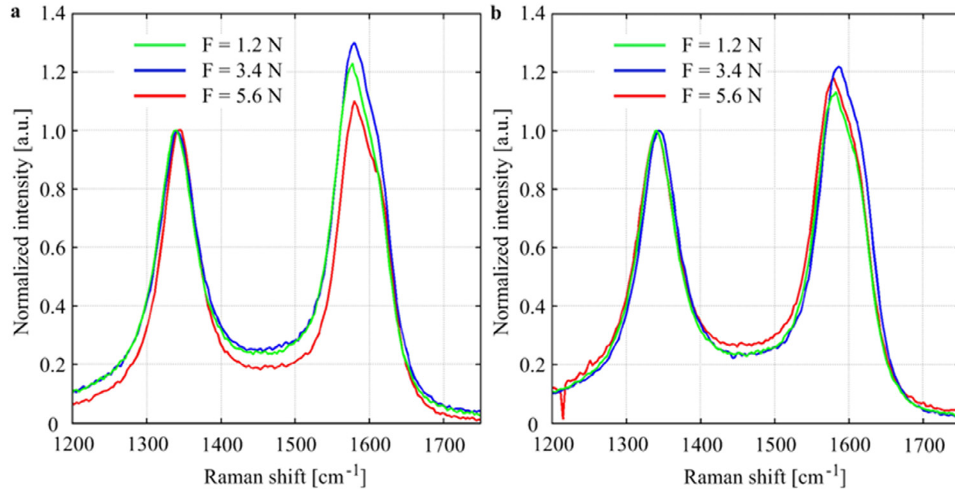

Figure 4.8 Normalized Raman spectra acquired for HA-CNT ribbons after rolling VACNTs having w = 20 µm, and (b) w = 100 µm, at various rolling forces. These spectra show that the change in CNT structural quality manifested by IG/ID ratio is negligible. For reference, IG/ID = 1.2 for a VA-CNT forest grown under the same CVD conditions.

4. 4 Transfer printing of HA-CNT

The HA-CNT ribbons can be robustly transfer printed to other substrates, including flexible films of PDMS and polyimide (Kapton) as shown in **Figure 4.9**. A smooth PDMS carrier substrate, made by curing and then delaminating the PDMS from a template silicon substrate, is laminated onto the original HA-CNT substrate after rolling and capillary densification. Taking advantage of kinematically controlled adhesion of PDMS to SiO2, the CNTs stick to the PDMS when the carrier substrate is peeled quickly from the growth substrate.[6] By laminating the PDMS carrying the HA-CNTs onto a polyimide film and then peeling it off slowly the HACNT bundles are uniformly transferred to polyimide as shown in **Figure 6d** and **e**. In contrast to previous PDMS transfer of crystallographically aligned HA-CNTs, the high packing density and uniform texture of our HA-CNT ribbons facilitates their direct printing without need to infiltrate the CNTs with a polymer as a carrier medium. Raman spectroscopy measurements again show no considerable change in the IG/ID ratio, suggesting the printing process does not damage the CNTs. Finally, the HA-CNT ribbons can be processed by standard

photolithography and plasma etching methods, enabling straightforward device fabrication and electrical characterization as described in Chapter 7.

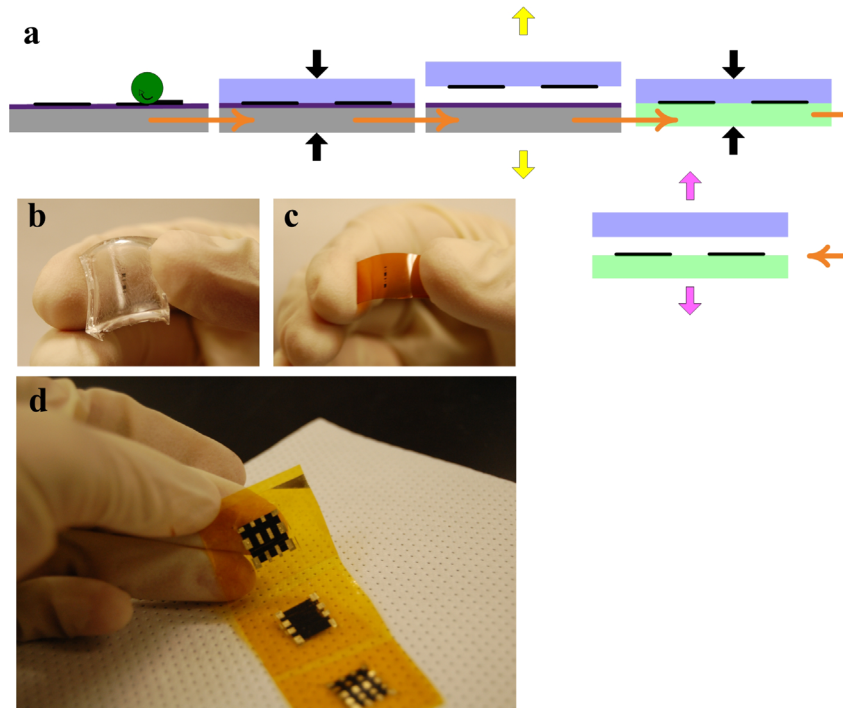

Figure 4.9 Transfer printing of HA-CNTs. (a) Schematic of the transfer printing process. (b) Transfer of CNT ribbons to flexible PDMS substrate; (c) Transfer to kapton substrate; and (d) transfer of several CNT sheet to kapton; Au electrodes shown in (d) were deposited by sputtering through a laser cut shadow mask.

4. 5 Bibliography

1. Tawfick, S.; O'Brien, K.; Hart, A. J., Flexible High-Conductivity Carbon-Nanotube Interconnects Made by Rolling and Printing. *Small* **2009,** *5* (21), 2467-2473.

2. Pint, C. L.; Xu, Y.-Q.; Pasquali, M.; Hauge, R. H., Formation of Highly Dense Aligned Ribbons and Transparent Films of Single-Walled Carbon Nanotubes Directly from Carpets. *Acs Nano* **2008,** *2* (9), 1871-1878.

3. Wang, D.; et al., Highly oriented carbon nanotube papers made of aligned carbon nanotubes. *Nanotechnology* **2008,** *19* (7), 075609.

4. Shigley, J. E.; Mischke, C. R.; Brown, T. H., Jr., Standard Handbook of Machine Design (3rd Edition). McGraw-Hill: 2004.

5. Wang, B. N.; Bennett, R. D.; Verploegen, E.; Hart, A. J.; Cohen, R. E., Characterizing the Morphologies of Mechanically Manipulated Multiwall Carbon Nanotube Films by Small-Angle X-ray Scattering *The Journal of Physical Chemistry C* **2007,** *111* (48), 17933-17940.

6. Meitl, M. A.; Zhu, Z.-T.; Kumar, V.; Lee, K. J.; Feng, X.; Huang, Y. Y.; Adesida, I.; Nuzzo, R. G.; Rogers, J. A., Transfer printing by kinetic control of adhesion to an elastomeric stamp. *Nat Mater* **2006,** *5* (1), 33-38.